MECHANISM OF LARGE-SCALE FLOWSLIDES DUE TO THE 2018 SULAWESI EARTHQUAKE, INDONESIA

ロヒート, デイブエシュ, モハンバイ

https://hdl.handle.net/2324/4496043

出版情報：Kyushu University, 2021, 博士（工学）, 課程博士
バージョン：
権利関係：

MECHANISM OF LARGE-SCALE FLOWSLIDES DUE TO THE 2018 SULAWESI EARTHQUAKE, INDONESIA

ROHIT DIVYESH MOHANBHAI

August, 2021

Dedicated to My Parents

MECHANISM OF LARGE-SCALE FLOWSLIDES DUE TO THE 2018 SULAWESI EARTHQUAKE, INDONESIA

A Thesis Submitted
In Partial Fulfilment of the Requirements
For the Degree of
DOCTOR OF ENGINEERING

By
Rohit Divyesh Mohanbhai

九州大学
KYUSHU UNIVERSITY

to the
DEPARTMENT OF CIVIL AND STRUCTURAL ENGINEERING
GRADUATE SCHOOL OF ENGINEERING
KYUSHU UNIVERSITY
August, 2021

DEPARTMENT OF CIVIL AND STRUCTURAL ENGINEERING
GRADUATE SCHOOL OF ENGINEERING
KYUSHU UNIVERSITY
Fukuoka, Japan

CERTIFICATE

The undersigned hereby certify that they have read and recommended to the Graduate School of Engineering for the acceptance of this thesis entitled, "***Mechanism of Large-scale Flowslides due to the 2018 Sulawesi Earthquake, Indonesia***" by **Rohit Divyesh Mohanbhai** in partial fulfilment of the requirements for the degree of **Doctor of Engineering**.

Dated: August, 2021

Thesis Supervisor:

Prof. Hemanta Hazarika, Dr. Eng.

Examining Committee:

陳 光斉

Prof. Guangqi Chen, Dr. Sci.

安福規之

Prof. Noriyuki Yasufuku, Dr. Eng.

國生剛治

Prof. Takaji Kokusho, Dr. Eng.

Prof. Ikuo Towhata, Dr. Eng.

ABSTRACT

The 2018 Central Sulawesi Earthquake caused massive flowslides at multiple locations on the gently sloping ground (gradient 1-3%) in the Palu Valley, killing more than 2000 people and causing catastrophic damage to infrastructure facilities. The flowslides caused extensive ground displacement ranging from several hundred meters to more than 1 km simultaneously at four key locations in Balaroa, Petobo, Jono Oge, and Sibalaya areas. From the field survey, it is observed that the relatively shallow part of the collapsed ground has a stratified structure consisting of a low-permeability fine-grained soil layer (cap layer) and a sand layer directly below it along the ground surface. It is assumed that the sand layer liquefied due to the strong Mw7.5 earthquake, leading to a flow failure. However, it is difficult to propose the exact mechanism which might have led to the triggering of liquefaction and flowslide over long distances in an extremely low-gradient ground.

The large-scale flowslide caused by this earthquake on gentle slopes is a special case with few precedents in the past. The main objective of this research is the academic question, "What kind of mechanism might have triggered such large-scale flowslide?". One such possibility might be, the squeezing out of the pore water from the sandy layer below the cap layer due to liquefaction. This might have formed a water film below the cap layer leading to the loss of shear resistance of soil layers including the cap layer. It is assumed that this led to the liquefaction of the upper layer.

Considering the above hypothesis, the mechanism of flowslide is investigated by a detailed field survey, laboratory model experiments, and numerical analysis of those. Furthermore, it is necessary to qualitatively evaluate the mechanism of the flowslide

that cannot be explained only by the mere lateral flow of the ground due to the liquefaction during an earthquake.

In this study, the soil lithology is confirmed through trench surveys and one-dimensional model experiments and numerical analysis are performed to evaluate the effect of the low permeability layer on the initiation of the flowslides and the water film formation phenomenon by the model experiments through 1g shaking table tests. From these results, the effects of the cap layer thickness, configuration, and permeability coefficient of the cap layer on the decrease in the shear strength of the ground were confirmed, and the collapse mechanism of the gently sloping ground are clarified.

This thesis is organized into 6 chapters. The contents of each chapter are summarized as follows:

Chapter 1 focuses on the large-scale fluidized flow failure of gentle slope ground at four locations in Palu Valley due to the 2018 Sulawesi Central Earthquake. The geological characteristics and seismic activity of the area, and the degree of damage caused due to the flowslides are discussed. This lays emphasis on the background and motivation of the current research. The necessity of elucidating the mechanism of large-scale flowslide, which is the purpose of this research is discussed and the originality of the research is also stated.

Chapter 2 clarifies the geological characteristics of the liquefied ground through a field survey. Here, the results of trench surveys, drone photography, and simple dynamic penetration tests conducted in the field are analyzed. Through the observations, it is confirmed that the ground lithology is stratified with the presence of a low permeability cap layer containing clay and silt, a loose sand layer under it. A very soft, liquefiable soil strata is also confirmed through the low converted N values of the shallow strata, which is 5 or less and a shallow groundwater table (within 2 m from the ground surface).

Chapter 3 discusses the results from 1g model experiments using a shaking table experimental device are conducted to examine the deformation characteristics of sandy ground with a cap layer during an earthquake. Here, the PIV (Particle Image Velocimetry) method is used to clarify the vector distribution of soil particle movement in the ground during an earthquake, with and without a cap layer. The results show that the presence of the cap layer delays the onset of slip rupture due to liquefaction during an earthquake.

Chapter 4 discusses one-dimensional liquefaction experiments on a loose saturated sand layer simulating a stratified structure which clarifies that a water film forms directly under the cap layer sandwiched in the sand layer. The effects of cap layer configuration and permeability on water film formation are also evaluated. Here, it is elucidated that, due to the presence of the cap layer, a delay occurs in the dissipation of excess pore water pressure after impact, and a water film is formed. Therefore, it can be concluded that the stratified structure of the ground confirmed in the field survey caused the formation of a water film after the earthquake, leading to flowslide.

Chapter 5 presents numerical analysis of one-dimensional liquefaction experiment models with a stratified structure are conducted to investigate the stress and strain generated at the boundary of the cap layer and elucidated the mechanism of flow failure by the water film. From the analysis results, it can be concluded that the rapid decrease in effective confining pressure and the increase in shear strain near the boundary of the cap layer are the causes of triggering the flow failure. Additionally, the stratified structure of the ground based on the trench survey conducted in the field is simulated and one-dimensional seismic response analysis is performed. From the analysis results using the actual seismic waveforms observed in Palu city, it can be concluded that the excess pore water pressure ratio between the sand directly under the relatively thick cap layer and the silt layer exceeded 1.0 and liquefied. It is also confirmed that the shear strain in the upper part of the relatively thick cap layer is almost zero, while the strain in the sand layer in the lower part of the cap layer exceeds 20%. From these results, it can be ascertained that flowslide occurred due to the formation of a water film accompanying the liquefaction of the sand layer.

Chapter 6 concludes the results and achievements of the research and sheds light on future research.

ACKNOWLEDGEMENT

As we say in India, a Guru comes before God as he is the one who shows you the right way through the darkness to the brightness of knowledge. Therefore, first and foremost, I would like to express my deepest gratitude to my supervisor, Prof. Hemanta Hazarika, for allowing me to work on this interesting research topic and for his valuable advice and assistance throughout my Ph.D. research. Prof. Hazarika has provided me many great opportunities to enhance my knowledge and experience, not only in research but overall personality development, which will always be there with me throughout my life. Prof. Hazarika always thinks about the future of his students and develops them to be self-reliant in terms of knowledge and experience.

It was a great pleasure for me to have the opportunity to pursue my graduate study at Kyushu University for which, I would like to express my deepest gratitude to the Ministry of Education, Culture, Sports, Science and Technology, Japan, for providing me with the MEXT scholarship.

I would like to express my sincerely gratitude to members of my dissertation committee, Prof. Hemanta Hazarika, Prof. Guangqi Chen, Prof. Noriyuki Yasufuku, Prof. Takaji Kokusho and Prof. Ikuo Towhata for their comments and feedbacks on the research. I am deeply indebted to Prof. Takaji Kokusho for his continuous and prompt responses to my request and queries and always providing insightful suggestions during my research. My heartfelt thanks go to our lab secretary Ms. Mika Murayama, who goes out of her way to provide all kinds of support and emotional support to me. I would like to specially thank Mr. Yuichi Yahiro for supporting me with my experiments and providing knowledgeable inputs during my tests. Special thanks go to Ms. Wa Ode Sumartini and Dr. Siavash Manafi Khajeh Pasha for support in data collection during the field survey in Palu, Indonesia. I would like to thank all my friends Mr. Chengjiong Qin, Mr. Hao Chunrui, Mr. Hu Yutao, Mr. Liu Yan and Mr. Tsubasa Maeda for consistently being with me and supporting me in all aspects of my life. I can’t thank enough to my friend and roommate Mr. Nag Sarthak (Kyushu University, Japan) for being with me during this period. Last but not the least, I am grateful to Dr. Sukiman Nurdin (Tadulako University, Indonesia), and Dr. Ardy Arsyad (Hasanuddin University, Indonesia) for their support during the field investigation in Palu, Indonesia.

Finally, no words are enough to express my gratitude to my parents for the sacrifices that they have made to make me capable enough to reach this far. I want to thank them for showering me with their unconditional love.

TABLE OF CONTENTS

LIST OF FIGURES

Figure 3.3 Actual side view of the soil model: (a) without kaolin layer and (b) with kaolin layer........75

Figure 3.4 Model setup with recording instrumentation........76

Figure 3.5 1g shaking table model characteristics: (a) soil properties and (b) input acceleration motion........77

Figure 3.6 The deformation of soil surface and layers relative to elapsed time and the formation of sand boils........79

LIST OF TABLES

NOMENCLATURE

D_r	Relative density of soil (%)
G_s	Specific Gravity of soil
LL	Liquid limit
PL	Plastic limit
CL	Cap layer
k	Permeability of soil
g	Acceleration due to gravity
e_{max}	Maximum void ratio
e_{min}	Minimum void ratio
Δu	Excess pore water pressure
Δu_{max}	Maximum excess pore water pressure
r_u	Excess pore water pressure ration
τ	Shear stress
γ	Shear strain
θ	Inclination angle
WT	Water table

CHAPTER 1

INTRODUCTION

1.1 BACKGROUND OF THE STUDY

The Central Sulawesi province of Sulawesi Island, Indonesia was rattled by an earthquake of magnitude M_w 7.5 earthquake on September 28, 2018 at UTC 10:02:44. The epicentre of the earthquake was at located at 0.256° S and 119.846°E in the neck of the mountainous Donggala Regency of Central Sulawesi province. The event was a shallow earthquake with a hypocentral depth of 20 km (USGS, 2018). While a peak intensity of 8.5 on MMI scale was observed in Palu region, the shock waves of the earthquake were felt across the Sulawesi Island along with some parts of the neighbouring Borneo Island and that of Malaysia. The earthquake was the main event, with a major foreshock of magnitude M_w 6.1 just 3 hours before and multiple aftershocks of significant magnitude $M_w > 5.5$ which followed for weeks (Figure 1.1).

Furthermore, the seismic parameters of the earthquake sourced from USGS (2018) as well as Global Centroid Moment Tensor (Ekström et al., 2012) are provided in Table 1.1. The ground failure and liquefaction resulted from the earthquake caused extensive damage to critical infrastructure facilities like, residential buildings, bridges, roads and irrigation canals. The succeeding tsunami inundation hit the coastal areas, sweeping away the shoreline structures and destroying the beachfront parks. The tsunami also brought down the iconic Yellow Ponulele bridge (Palu bridge) which connected the East and West Palu (Figure 1.2 a and b). The Tsunami inundation occurred mainly along the Palu Bay, with a wave run-up height of 6 m and above, also as there was no trace of tsunami damage outside the bay, the cause of tsunami was proposed to be a submarine landslide within the bay (Liu et al., 2020; Mikami et al., 2019; Sassa & Takagawa, 2019). Both the earthquake and tsunami created havoc in the areas of Donggala and Sigi Regency with a loss of thousands of lives and lakhs displaced.

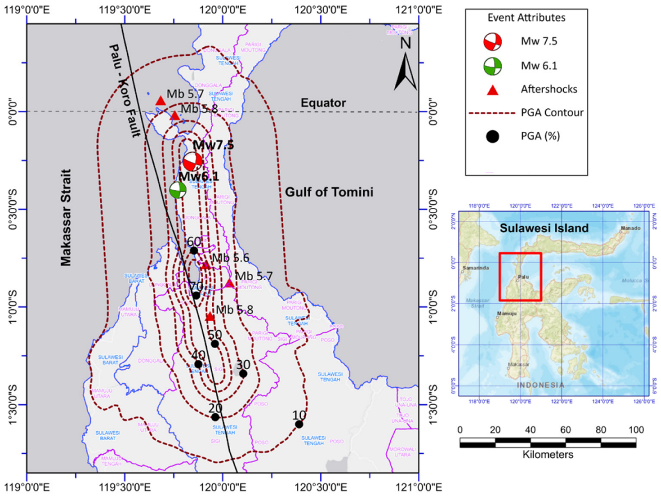

Figure 1.1 Location of the foreshock, mainshock and aftershocks of the 2018 Sulawesi earthquake along with the PGA contours (modified from Rohit et. al., 2021).

Table 1.1 The seismic parameters of the 2018 Sulawesi earthquake as reported by USGS and GCMT (Rohit et. al., 2021).

Parameter	**Global CMT**			**USGS**		
Centroid time	10: 2: 59.4 GMT			10:02:45 UTC		
Hypocentral depth (km)	12			20		
Half duration (s)	14.2			20.48		
M_w	7.6			7.53		
M_s	7.5			-		
Scalar moment (nm)	2.82E+27			2.497E+20		
	Strike	**Dip**	**Slip**	**Strike**	**Dip**	**Slip**
Fault plane 1	87°	77°	-146°	87°	74°	-156°
Fault plane 2	348°	57°	-15°	350°	67°	-17°

(a)

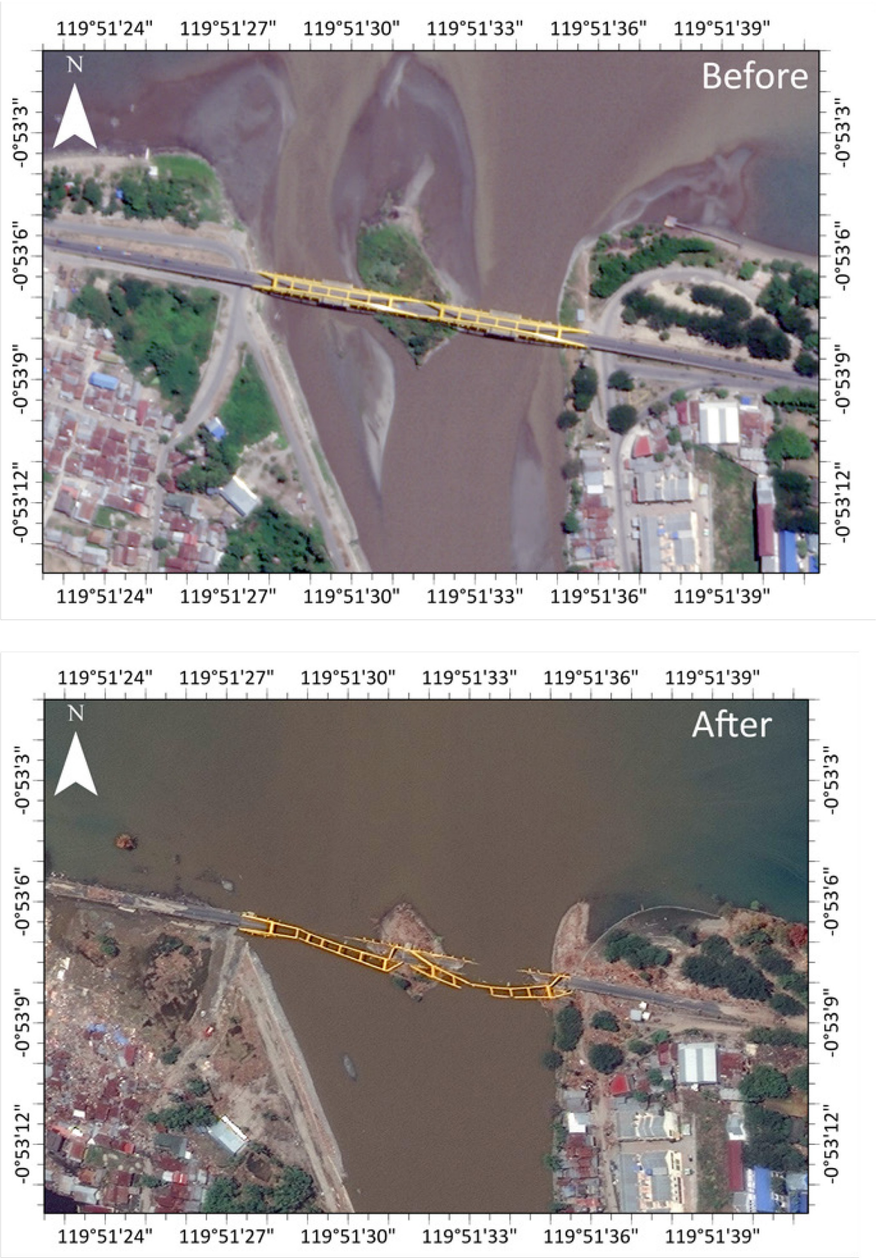
119°51'24"
119°51'27"
119°51'30"
119°51'33"
119°51'36"
119°51'39"
N
Before
-0°53'3"
-0°53'6"
-0°53'9"
-0°53'12"
After

(b)

Figure 1.2 The Yellow Ponulele bridge, Palu: (a) Before (September 28, 2018) and after (October 1, 2018) satellite image (modified from BNPB ArcGIS Map service) and (b) Actual picture of the damaged bridge from the site.

Table 1.2 here provides the information regarding the impact of the earthquake on human lives and housing infrastructure. Out of 2,101 deaths across Central Sulawesi province, the provincial capital, Palu alone had over 1700 deaths (HCT, 2018). This was due to the extensive landslides and geotechnical failure caused due to the earthquake. The Palu valley, which is around 70km south of the epicenter, suffered the maximum damage due to the earthquake. Four key locations in the Palu valley namely, Balaroa, Petobo, Jono Oge and Sibalaya experienced extensive landslides and liquefaction, which completely destroyed the localities living in these areas. At all these locations, the landslides occurred rapidly, with soil movement in massive blocks along with debris flow, hence these landslides could be classified as flowslides according to the Varnes classification (Hungr et al., 2014). These flowslides occurred in a very gentle sloping ground with the gradient less than 5-7% on an average and engulfed a large amount of area under it (Hazarika et al., 2021). It was also unique that, the flowslides initiated after the seismic ground motion ceased. Figure 1.3a, here shows the images acquired on before (September 23, 2018) and after (October 2, 2018) the earthquake by Operational Land Imager (OLI) on Landsat 8 satellite (USGS, 2018) in false color bands (6-5-2) to make it easy to differentiate between the urban areas (purple-gray), vegetation (green), and over-turned soil (brown and tan). From the after-earthquake image, the mud flow and debris can be clearly identified which occurred due to liquefaction induced flow failure. All the flowslides sites except Balaroa were surrounded by water bodies from at least two sides (Figure 1.3b). Petobo, Lolu and Jono Oge had the Gumbasa irrigation canal running along the crest of the sites, while the Palu river which runs along the centerline of the Palu valley, was present on the downstream side. It has been reported that, the irrigation canal was running full of water at the time of the earthquake (Gallant et al., 2020). The breach of the canal caused the mudslide and debris flow along with the flowslide, which increased the potential of damage and also acted as a key contributor to the flowslides.

Table 1.2 Damage estimates in Central Sulawesi Province due to the 2018 Sulawesi earthquake and tsunami (HCT, 2018).

Group	Numbers
Missing people	1373
Deaths	2101
Grievous injuries	4438
Internally displaced	173552
Houses damaged	68451

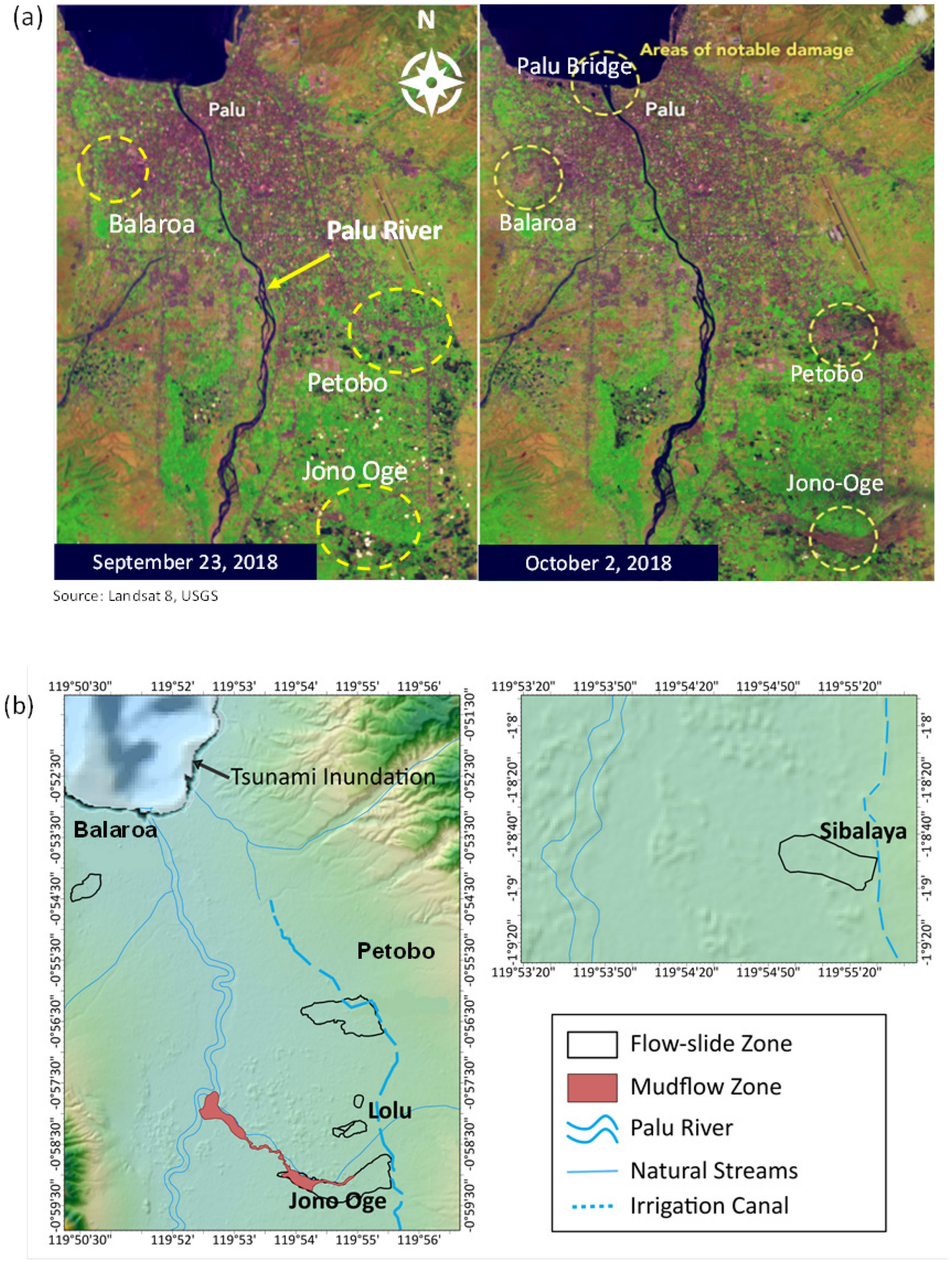

Source: Landsat 8, USGS

Figure 1.3 Damage due to the 2018 Sulawesi earthquake in Palu: (a) Landsat 8 images from before and after the earthquake (not to scale) and (b) key hydrological features surrounding the flowslide locations.

1.2 CHARACTERISTICS OF THE 2018 SULAWESI EARTHQUAKE

1.2.1 The foreshock, mainshock and aftershocks patterns

Earthquakes occur across a fault when the stresses in the sliding rocks reach the strength of crustal rocks. During an earthquake enormous amount of energy is released across the fault while readjusting crustal stresses around the plate boundaries. This stress readjustment, also known as Coulomb stress change generates aftershocks and according to Omori's law (Omori, 1894), after each earthquake, aftershocks follow and the frequency of these aftershocks decay with time depending on crustal strength across the fault and surrounding areas and the amount of stress accumulated. Also, each shock or aftershock can be a foreshock to another big earthquake. The same phenomenon was observed during the September 28, Sulawesi earthquake of magnitude M_w 7.5. As seen in Figure 1.4, just hours before the main shock, a foreshock of M_w 6.1 occurred which was of a large magnitude in itself. Further in the figure, the seismic history of Sulawesi region across the PKF is presented for the period of September 19, 2018 – October 31, 2018 depicting the foreshocks, mainshock and the aftershocks.

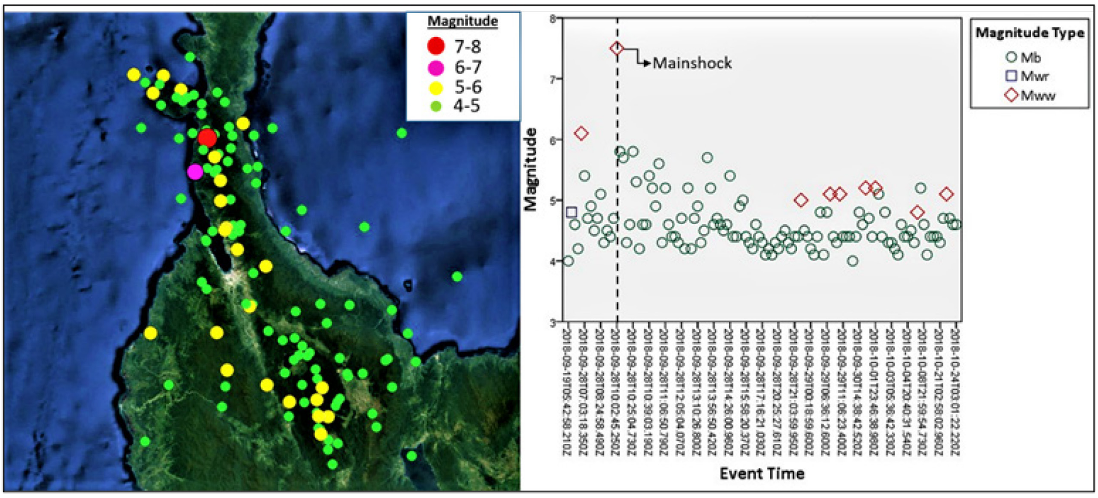

Figure 1.4 Distribution (left) and magnitude versus event time plot (right) for the earthquake events (M>4) in Central Sulawesi during the period of September 19, 2018 – October 31, 2018 (inset figure, USGS, 2018) (Map not to scale).

The foreshocks and aftershocks divided by a dotted line on the mainshock event. It can be inferred from the figure that almost all of the foreshocks and aftershocks are greater than a magnitude of 4 while multiple aftershocks of magnitude greater than 5 are observed. This relates to the amount of stresses released during the event and high slip rate of PKF.

1.2.2 Moment tensors, finite faults and surface fault rupture

Moment tensors are usually represented as beach balls which help in determination of the pattern of energy radiated as well as orientation of fault slip during a seismic event on a fault plane, through the analysis of first arrivals of P - waves as already shown in Figure 1.1. In case of the 2018 Sulawesi earthquake, the moment tensor of the main shock depicts a high probability of left-lateral strike slip along with a component of normal force in east – dipping fault approximately 60° (Socquet et. al., 2019). The fault solution of the main shock tensor as well as the foreshock tensor (Mw 6.1) describing the possible rupture is in conjunction with the actual geological and fault characteristics of Palu city which is straddled by a sinistral E – W striking PKF. The fault rupture which caused the earthquake was spread in an area of approximately 200 x 20 km, with a major part of rupture mainly in the south of the hypocenter (GEMPA, 2018). The rupture caused during the event was not a pure strike-slip, but with transpressive component generating mixed focal mechanism (Hui et al., 2018). The event created a rupture of length about 200 km in 30s at a speed of 4 – 4.1 kms^{-1} which lies in between the P and S wave propagation velocities also termed as supershear rupture (Bao et al., 2018). It was also considered as one of the reasons for large intensity of ground motion (Socquet et al., 2019). Furthermore, as seen in Figure 1.5 that the focal depths or hypocentral depths for most of the shocks (foreshocks, main event and aftershocks) occurred at depths of less than 15 m which indicates the crustal rupture at shallow depths confirming the interlocking of crustal plates at depth of 12 km in previous studies (Socquet et al., 2006a).

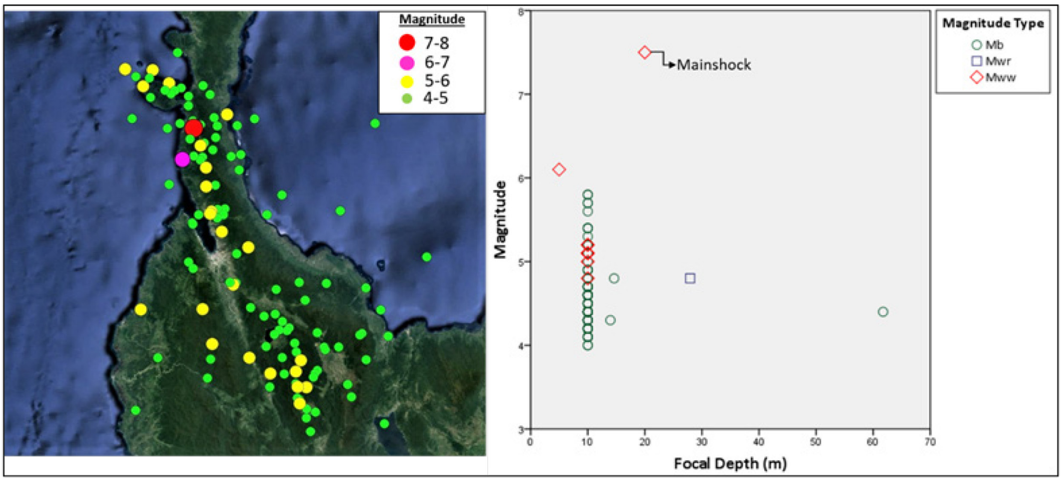

Figure 1.5 Distribution (left) and magnitude versus focal depth plot (right) for the earthquake events (M>4) in Central Sulawesi during the period of September 19, 2018 – October 31, 2018 (inset figure USGS, 2018) (Map not to scale).

1.2.3 Characteristics of the ground motion

Ground motion data of earthquake was recorded at the JICA-BMGK station in Palu, which is approximately 80 km from the epicentre and on the west side of earthquake induced landslide area at Balaroa (Fig. 1.6). The time history of acceleration for two horizonal components E-W and N-S and vertical component U-D of ground motion Fig. 1.7a~c, using the data provided in JICA Report (2019). The peak ground acceleration (PGA) values of the E-W, N-S and U-Components were 198.97 Gal, 200.2 Gal, and 335.1 Gal respectively. The response spectra shown in Fig. 1.7d display near-fault motion features likely to have been caused by forward directivity of rupture propagation. Furthermore, the wide range frequency content of ground motion increased the risk of geotechnical failure at various places. However, the response spectral values at the Palu station were reported to be less than those proposed by the Indonesian seismic design code, except for the period range of 2.5–3.5 s.

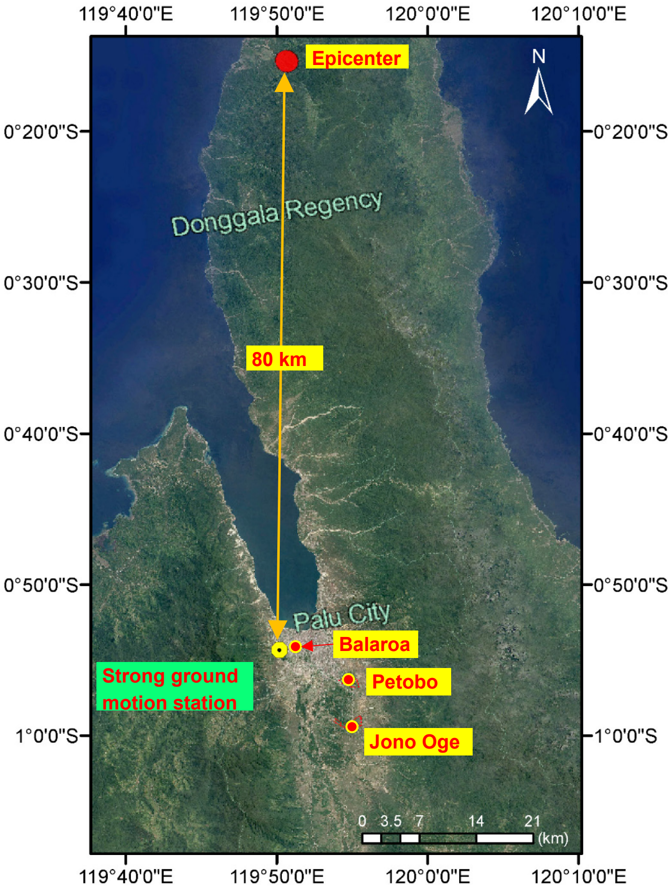

Figure 1.6 JICA-BMGK strong motion station (JICA Report, 2019).

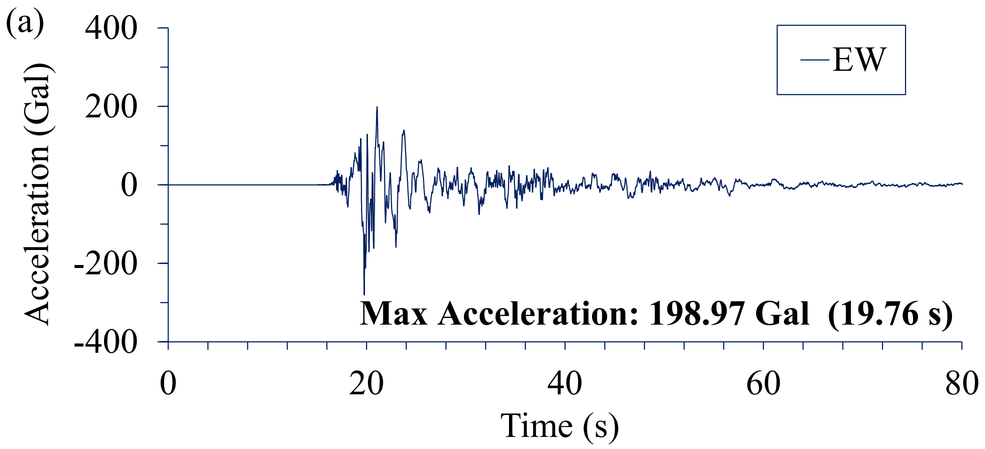

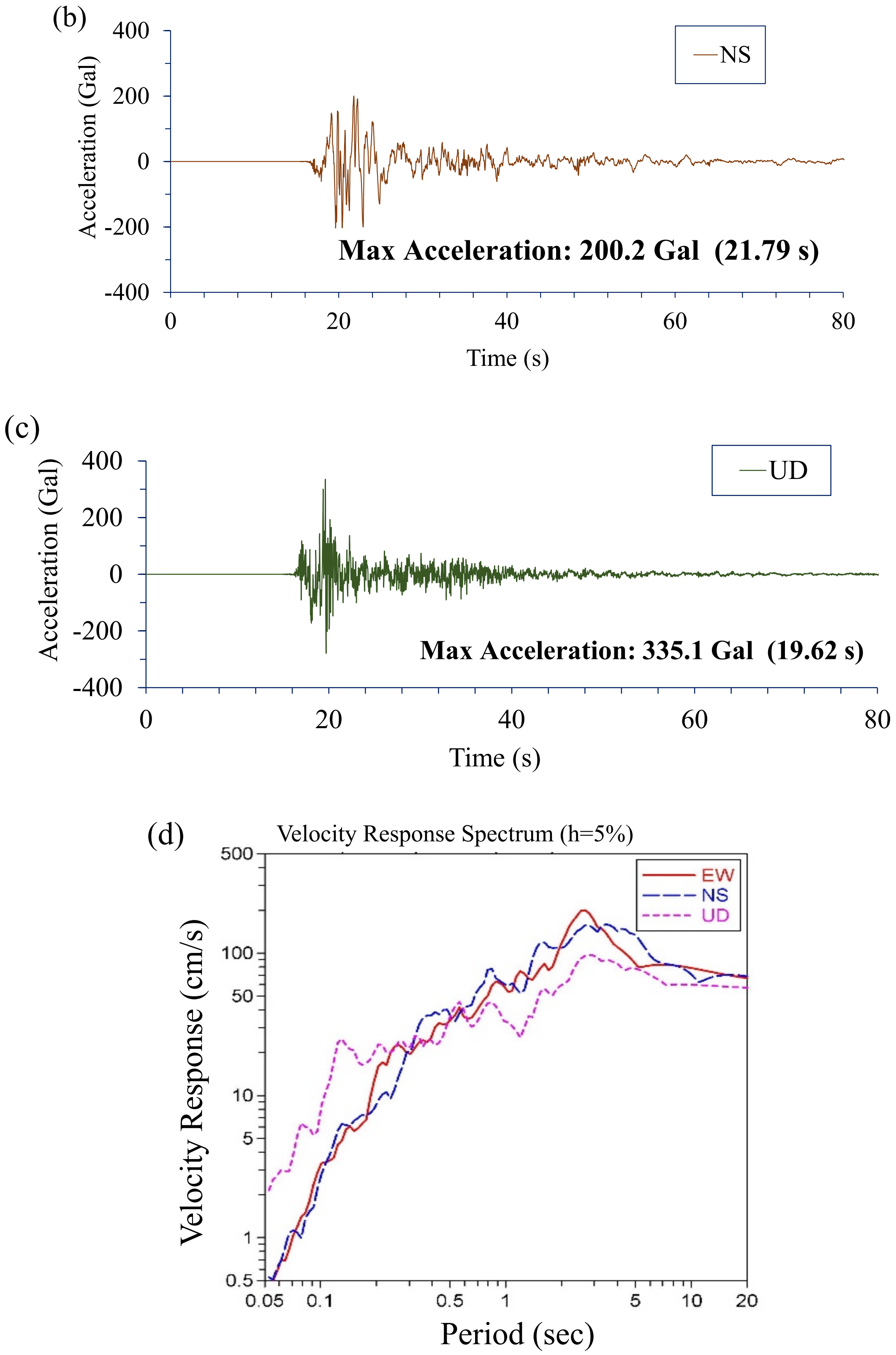

Figure 1.7 Time history of motions at strong ground motion station near Balaroa (a) E-W (b) N-S (c) U-D components and (d) Velocity responses (Adopted and modified from the data in JICA Report, 2019).

1.3 SITE CHARACTERISTICS

1.3.1 The geological history of Sulawesi area and Palu valley

Being the world's eleventh largest island with an area of 1,59,000 sq.km, Sulawesi or Celebes as it's called is among the one of the four Greater Sunda Islands in the Malay Archipelago. The island lies at the junction of three convergent plates namely the Asian, the Australian and the Pacific plates (Villeneuve & Gunawan, 2002). Sulawesi seems to be constituted of two discrete types of geological outcrops which were combined in late Cenozoic Era by extensive plate movements (Audley-Charles, 1981). Due to this crustal movement it consists of two distinct geological provinces namely the East Sulawesi and West Sulawesi between Palu and Gulf of Bone (Gursky, 2015). It has also been inferred that the eastern part of central Sulawesi, east arm, the southeast arm and the central arm represents the outer arc of Sulawesi, consisting a high-pressure metamorphic belt formed under a trench zone (Miyashiro, 1961). Further, the northern arm, the southern arm and the west – central Sulawesi which comprise the inner arc, consists a low-pressure metamorphic belt formed under a volcanic chain in the adjoining island arc or continental margin. The Celebes Island is divided into six provinces, Central Sulawesi being one of them and the area of interest in current research where the provincial capital Palu lies. Central Sulawesi consists of the region from Makassar Trough till the Gulf of Tolo (Bemmelen, 1949) which seems to be a geologic accretion formed during the Cretaceous and Paleogene period (Hamilton, 1979) as a junction between the east and west Sulawesi. It has a widely distributed granitic rocks which have intruded into the late Tertiary to Pleistozoic and Metamorphic rocks. These geologic units are overlain by Neogene Tertiary formations and Quaternary alluvium deposits (Metallic Minerals Exploration Agency, 1973). Furthermore, the geologic structure of Central Sulawesi is influenced by two tectonic faults namely Tawaëla graben in the eastern region with a N-S orientation and Fossa Sarasina graben (Palu - Koro Fault) in the central region with a NNW-SSE orientation (Metallic Minerals Exploration Agency, 1973).

The Palu valley was shaped by the trans-tensional tectonics involving the Palu-Koro Fault (PKF) system. The geological map of Palu region with the flowslide locations is shown in Figure 1.8a. The bed rock in Palu region predominantly consists of the Palu Metamorphic Complex (PMC) which is capped by Cenozoic sedimentary-volcanic Upper Cretaceous progressions. This complex forms the rugged mountain chain on the eastern flank of the valley (T. van Leeuwen et al., 2016). Neogene sedimentary rocks, informally called Celebes Molasse are also prevalent in Sulawesi which predominantly consist of conglomerates, sandstones, and mudstones with limestone interlayers (Surono & Sukarna, 1996). In south, the PMC is surrounded and covered by the Upper Cretaceous Latimojong Formation, which mainly comprises weakly metamorphosized pelitic and fine-grained psammitic rocks with subordinately intercalated volcanic rocks. The Malihan rocks or the Malino Metamorphic Complex is mainly constituted of mica schists, gneisses, greenschist, amphibolite, marble and quartzite. The Gumbassa Complex contains metamorphic rocks analogous to the PMC (van Leeuwen & Muhardjo, 2005).

Furthermore, the Palu valley is flanked by the mountains on both sides, which run North – South with peaks reaching to 2.3km (Bellier et al., 2001). While, the heights are dominated by metamorphic complexes and granitic rocks, the mid and lower ranges consist of the old (~ 120 Kya) and young (~11 Kya) alluvium fan deposits on the western and eastern flank of Palu valley along with debris flow deposits (Patria & Putra, 2020). The central part of the Palu valley, which is the flood basin of Palu river, mainly consists of alluvial deposits, flood deposits and old river channel deposit

(Kusumawardani et al., 2021). The alluvial deposits are mostly distributed as fans of the rivers streaming to west and downstream of the Palu river (Figure 1.8b). These fans are primarily deposited as seams of sand, gravel and silt (Metallic Minerals Exploration Agency, 1973). A past study on the sedimentary deposits of Ariana region confirmed that the young sedimentary deposits are susceptible to liquefaction, with a shallow ground water table and under 0.2 g ground motion acceleration (May et al., 2009).

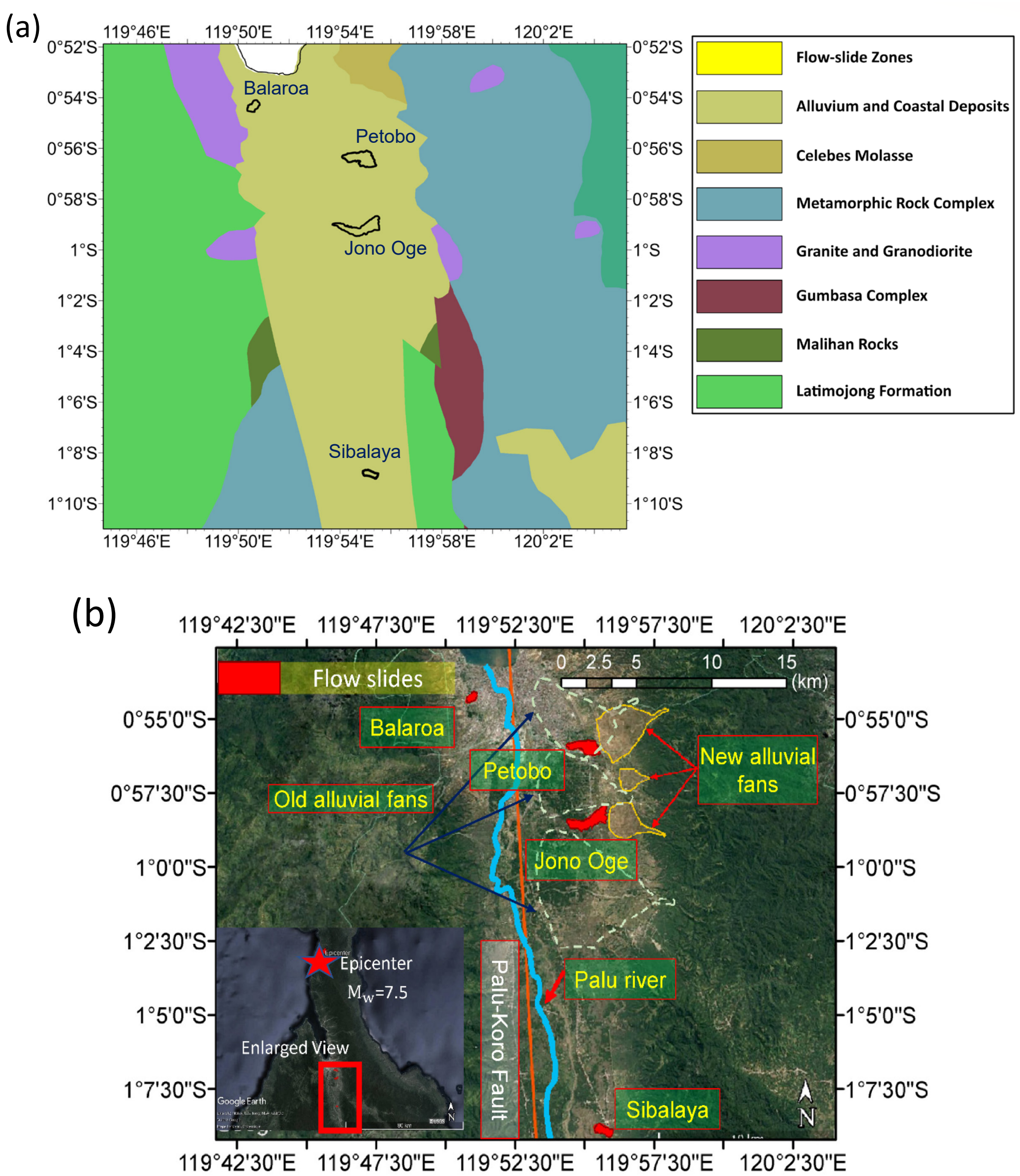

Figure 1.8 Geology of Palu Valley: (a) Spatial variation of underlying deposits and (b) the distribution of old and new alluvial fans around the flowslide sites (Hazarika et. al., 2021)

1.3.2 Geodynamics of Sulawesi Island and seismicity of Palu Koro Fault

The location of Sulawesi Island is one of the key reasons for consistent seismic events experienced by it as it lies at the tri-junction of the Australian, Eurasian and Philippine Sea plates (Hamilton, 1979) with a complex memoir of subduction, extension, ophiolite obduction and collision of continental fragments (Hamilton, 1979; Hall, 2014). There are multiple active major and minor faults in Sulawesi, which are responsible for historic earthquakes of magnitude ≥6. The Central Sulawesi region which is the most seismically active part of Sulawesi, was formed due to the multistage subduction and collision of the tectonic plates (Bellier et al., 2006). Figure 1.9 here depicts the active faults in Central Sulawesi and the fault mechanisms of some major historic earthquakes (M≥6) which occurred in the region (fault locations after BNPB (2018); focal mechanism beach balls created using Data Assistant, by Exprodat).

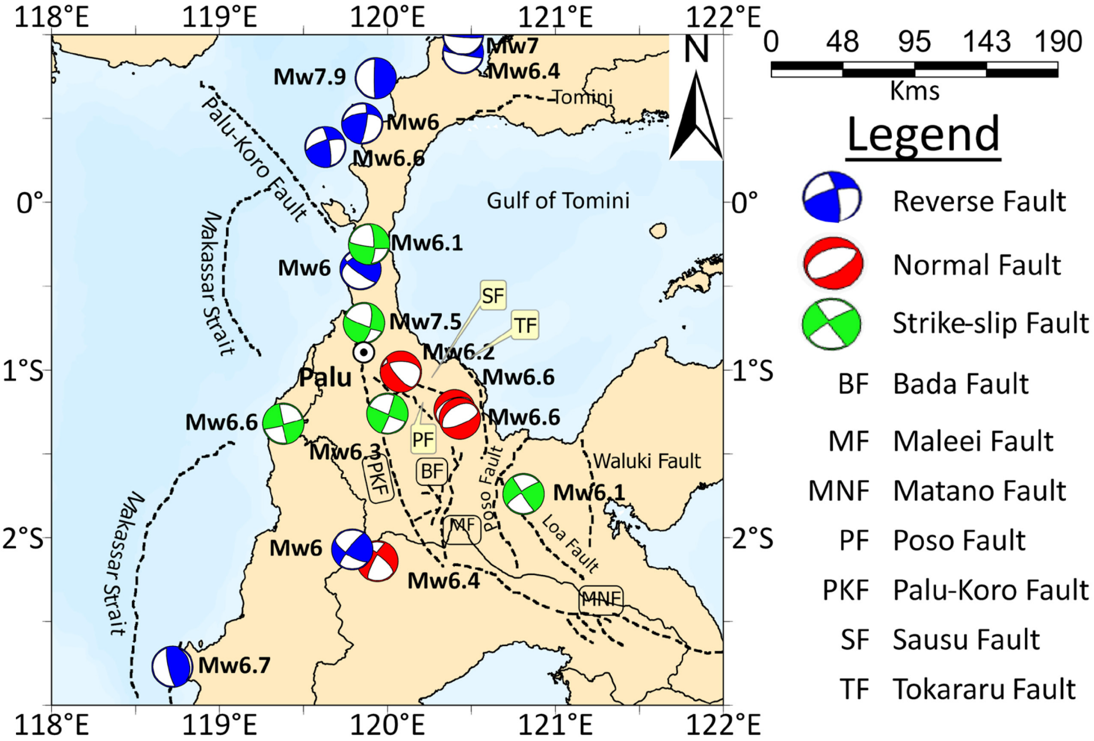

Figure 1.9 Focal mechanism of past earthquakes (M>6) and the locations of some of the active faults in Sulawesi.

Sulawesi hosts one of the world's most active strike-slip fault, the Palu-Koro Fault (PKF), which bifurcates the Central Sulawesi Province into two parts, the western central Sulawesi which is the northern part of Makassar block and the seismically active Eastern Central Sulawesi (ECS) (Fang et al., 2019). The PKF is considered to an active zone of significant strain with an estimated average annual sinistral slip rate of 39 mm and an extension rate of 11 mm (Socquet et al., 2006b). Also, past research has claimed the ability of PKF to generate supershear earthquakes as the 2018 Sulawesi earthquake, with its shallow seismicity (Watkinson & Hall, 2017). The supershear ruptures tend to generate an S-wave stem, which can travel to long distances and the seismic energy transmitted by them is of high amplitudes which amplify the damage as observed in Palu. The Sulawesi region also hosts multiple minor faults like Bada Valley fault, Matano fault, Sausu fault and Takararu fault, which are depicted in Figure 1.9, but they are out of bound of this study. Hosting an active strike – slip fault, the region has experienced multiple large devastating earthquakes in the past. From the historic seismicity of the PKF region, it can be inferred that the fault activity is concentrated at shallow depths with major earthquakes of magnitude $M_w \geq 6.5$ during years 1900–2018 with a hypocentral depth of less than 50 km (Hazarika et al., 2021). In past, various researchers have studied the seismic activity of Sulawesi using GPS and gravimetric methods by dividing the island in various microcontinents or blocks which suggest high seismic activity and presence of the high extension and compression zone across the PKF (Socquet et al., 2006; Sarsito et al., 2017). Cipta et al., 2017 conducted probabilistic seismic hazard analysis of Sulawesi along with the influence of site amplification using proxy methods. The study found that seismic hazard was highest in Central Sulawesi along the PKF and lowest in southern arm of Sulawesi. It was also evaluated that the cause of this high seismicity was due to fast movement of PKF which also caused high hazards in far field from the faults, which gives rise to a high intensity event of PGA>0.8g with a 500 year return period. Figure 1.10 presents the VS30 map for Sulawesi and Palu region in the inset. Therefore, it can be said that, a seismic hazard is imminent in Sulawesi Island within a stipulated time, also with low shear wave velocity (V_{s30}), the damage could be aggravated by site amplification leading to liquefaction.

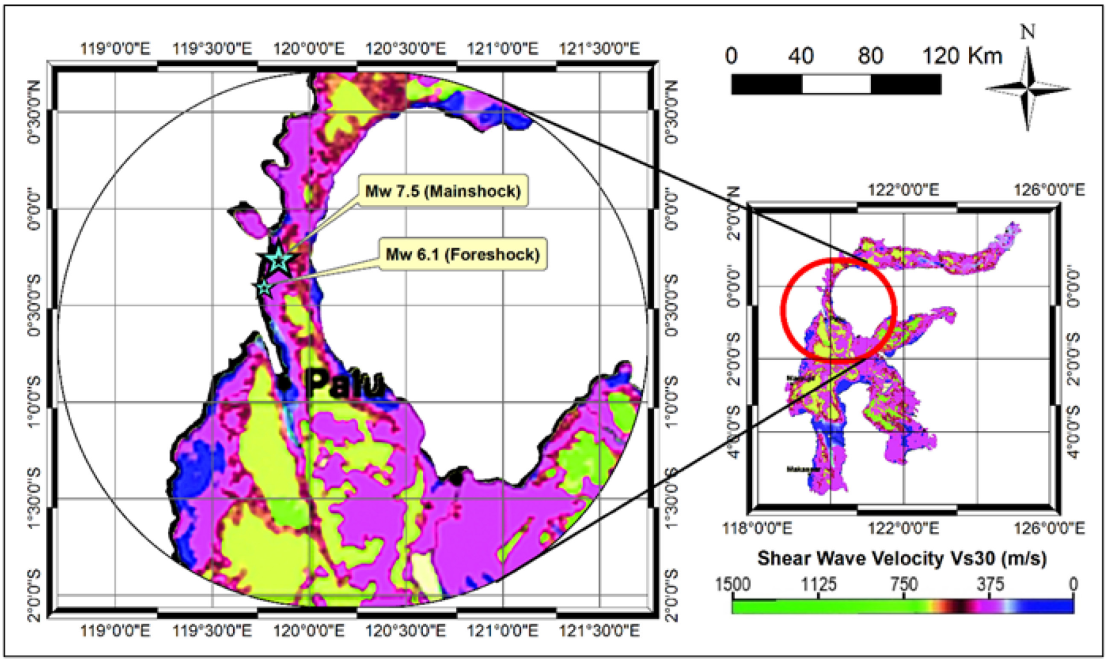

Figure 1.10 Shear wave velocity map, V_{s30} (m/s) of Sulawesi Province with inset figure showing V30 profile for Palu region and the main shock and foreshock for 28th September 2018 Donggala Earthquake (modified from Cipta et al., 2017).

1.4 LITERATURE REVIEW

1.4.1 Failure mechanisms proposed based on field investigations

Although the precise reason behind the triggering of this large-scale geotechnical disaster is yet unknown, many hypotheses have been proposed by researchers on the exact cause of such massive flowslides. They are discussed as follows:

1) **Water film formation**

Kokusho (JICA Report, 2018) proposed that during liquefaction, pore water from underlying liquefied layer tended to gush upward, but due the presence of an overlying low permeable cap layer, the water remained below this layer and formed a thin ‘water film’. This caused the reduction in friction at the cap layer interface and triggered the surface layer to flow downward under gravity.

2) **Rupture of a confined aquifer**

   It was postulated that, due to the probable liquefaction of surface layer liquified during the earthquake, the frictional force resisting the lateral movement reduced drastically, this initiated a major landslide along the slope under the influence of gravity. As the surface was ruptured due to the triggering of landslide, the water from the underlying confined aquifer might have rushed to the surface supplying additional water to the already liquified layer, thereby sustaining the flow for a long distance and time (JICA Report, 2018).

3) **Flowslides linked to the irrigation system**

   Watkinson et. al., (2019) and Bradley et. al., (2019) attributed the cause of the long run-out landslides to the irrigation system and shallow water table in the areas. The irrigation structure near the head scarp was unlined, which might have also led to increase in ground water table in the areas through seepage. The above two factors disturbed the naturally meta-stable alluvial fans which might have led to flowslides.

1.4.2 Previous research on influence of capping layer and liquefaction induced lateral deformation

In past, multiple studies have been conducted on the lateral flow failure in gentle slopes. Many of them have highlighted the formation of water film beneath a low permeable capping layer overlying a permeable sandy layer during liquefaction (Bolton, 1987); Butterfield & Bolton, 2003; Ishihara, 1985). Kokusho et. al., (2002; 1999) performed multiple 1D and 2D experimental tests using non-plastic fines as capping layer in between uniform sand layers. It was observed during the tests that, the capping layer inhibited the dissipation of excess pore water pressure from the liquefied underlying sand layer, this further delayed the soil to gain the initial effective stress thereby creating a dynamic instability at the interface of capping layer and sand layer. The studies also underscored, the delayed deformation of overlying soil layers . Numerical studies related to the formation of water film below a capped layer have been conducted in past with regards to liquefaction induced lateral spreading in gently sloped ground (El Shamy et al., 2010). It has also been studied how the trapped water below the capping layer could later result in the formation of sand boils (Yang & Elgamal, 2001). In addition to it, the water film formation and its influence on the lateral mass movement of ground in a sub-marine environment has been demonstrated through physical experiments by Kawakita et. al., (2020).

1.5 SCOPE AND OBJECTIVES

The earthquake induced widespread liquefaction and other geotechnical failures caused catastrophic damage to the population and infrastructure. The sheer scale of ground displacement, gentle terrain, and the time of initiation of flowslides attracted the attention of researchers from across the globe. Furthermore, it was first of a kind of event where multiple, synchronous, flowslides occurred on a ground with no prior recorded history of landslides. Therefore, it is necessary to clarify the mechanism of such long-distance flowslides in gently sloping ground based on the field data, laboratory tests, and numerical simulations of those. The purpose of this study are as follows:

1) To make clear the mechanism of such long-distance flowslides in a gently sloping ground based on the field data, laboratory tests, and numerical simulations of those.
2) To assess the soil particle movement during flowslide.
3) To elucidate the influence of multiple capping layers in the dissipation of excess pore water pressure in soil strata.

4) To evaluate the formation and stability of water film in a multi-cap layer soil environment with varying permeability.
5) To elucidate the forces generated in the soil strata at the cap layer interface which could contribute to the flowslide.

1.6 ORIGINAL CONTRIBUTION TO THE KNOWLEDGE

The flowslides in Palu were the first of their kind due to the scale of area covered, the very gentle gradient of the ground on which they occurred and the initiation time. A multi-pronged approach was adopted involving field investigation, experimental techniques, and numerical analysis to elucidate the mechanism behind the flowslides. Field investigations were carried out at the flowslide sites to assess the geological setting and bearing resistance of the soil. The soil stratifications with cap layers observed during the field investigations were then simulated through 1D and 2D experimental tests under impact and dynamic loading conditions. Furthermore, the 1D response analysis and 1D site response analysis were performed on scaled 1D experimental models and in-situ soil strata to determine the forces generated in the soil profile due to the cap layers and study the probable failure zone. Some key findings of this study which are an original contribution to the knowledge are as follows:

1. The presence of multiple alternating layers of fine sandy clay/silt sandwiched in between the coarse grain soils was confirmed across the flowslide sites through trenching. These fine soil layers tend to act as a cap layer inhibiting the dissipation of excess pore water pressure from underlying liquefied layers. Furthermore, at each trench, the cap layers had different plasticity characteristics, some were non-plastic, while some were plastic, which could severely affect the interlayer transmissivity of pore water during liquefaction (Chapter 2).

2. From 1D model tests, it could be concluded that the permeability and plasticity of the cap layers significantly influenced the stability of soil strata by controlling the dissipation time of excess pore water pressure. Non-plastic cap layers could not form a stable water film leading to quicker dissipation of excess pore water pressure from the underlying soil layers, leading to stabilization of the underlying layers (Chapter 4).
3. From 1D site response analysis of the in-situ soil strata, it could be ascertained that, the thickness of cap layer was one of the key parameters controlling the failure of underlying soil layers. Thin cap layers tend to disintegrate during the earthquake loading or breach due to the high upward pressure generated by the pore water, therefore preventing failure of underlying soil layers. (Chapter 5).

1.7 THESIS ORGANISATION

This thesis is organized into six chapters. The contents of the chapters are summarized as follows:

Chapter 1, here the research focuses on the large-scale fluidized flow failure of gentle slope ground at four locations in Palu Valley due to the 2018 Sulawesi Central Earthquake. The geological characteristics and seismic activity of the area, and the degree of damage caused due to the flowslides are discussed. This describes the background and motivation of the current research. The necessity of elucidating the mechanism of large-scale flowslide, which is the purpose of this research is discussed and the originality of the research is also stated.

Chapter 2 clarifies the geological characteristics of the liquefied ground through a field survey. Here, the results of trench surveys, drone photography, and simple dynamic penetration tests conducted in the field are analysed. Through the observations, it is confirmed that the ground lithology is stratified with the presence of a low permeability cap layer containing clay and silt, a loose sand layer under it. A very soft, liquefiable soil strata is also confirmed through the low converted N values of the shallow strata, which is 5 or less and a shallow groundwater table (within 2 m from the ground surface).

Chapter 3, here 1g model experiments using a shaking table experimental device are conducted to examine the deformation characteristics of sandy ground with a cap layer during an earthquake. Here, the PIV (Particle Image Velocimetry) method is used to clarify the vector distribution of soil particle movement in the ground during an earthquake, with and without a cap layer. The results show that the presence of the cap layer delays the onset of slip rupture due to liquefaction during an earthquake.

Chapter 4 discusses one-dimensional liquefaction experiments on a loose saturated sand layer simulating a stratified structure which clarifies that a water film forms directly under the cap layer sandwiched in the sand layer. The effects of cap layer configuration and permeability on water film formation are also evaluated. Here, it is elucidated that, due to the presence of the cap layer, a delay occurs in the dissipation of excess pore water pressure after impact, and a water film is formed. Therefore, it can be concluded that the stratified structure of the ground confirmed in the field survey caused the formation of a water film after the earthquake, leading to flow failure.

Chapter 5 presents numerical analysis of one-dimensional liquefaction experiment models with a stratified structure are conducted to investigate the stress and strain generated at the boundary of the cap layer and elucidated the mechanism of flow failure by the water film. From the analysis results, it can be concluded that the rapid decrease in effective confining pressure and the increase in shear strain near the boundary of the cap layer are the causes of triggering the flow failure. Additionally, the stratified structure of the ground based on the trench survey conducted in the field is simulated and one-dimensional seismic response analysis is performed. From the analysis results using the actual seismic waveforms observed in Palu city, it can be concluded that the excess pore water pressure ratio between the sand directly under the relatively thick cap layer and the silt layer exceeded 1.0 and liquefied. It was also confirmed that the shear strain in the upper part of the relatively thick cap layer was almost zero, while the strain in the sand layer in the lower part of the cap layer exceeded 20%. From these results, it can be ascertained that fluid fracture occurred due to the formation of a water film accompanying the liquefaction of the sand layer.

Chapter 6 concludes the results and achievements of the research and sheds light on future research.

REFERENCES

Audley-Charles, M. G. (1981). Geometrical problems and implications of large scale overthrusting in the Banda Arc–Australian margin collision zone. 407–416. *Geological Society, London, Special Publications*, *9*(1), 407–416.

Bao, H., Ampuero, J., Meng, L., Fielding, E. J., Liang, C., Feng, T., & Huang, H. (2018). Early and persistent supershear rupture of the 2018 Mw 7.5 Palu earthquake Han. *Nature Geoscience*, 1–21.

Bellier, O., Sébrier, M., Seward, D., Beaudouin, T., Villeneuve, M., & Putranto, E. (2006). Fission track and fault kinematics analyses for new insight into the Late Cenozoic tectonic regime changes in West-Central Sulawesi (Indonesia). *Tectonophysics*, *413*(3–4), 201–220.

Bellier, O., Siame, L., Beaudouin, T., Villeneuve, M., & Braucher, R. (2001). High slip rate for a low seismicity along the Palu-Koro active fault in Central Sulawesi (Indonesia). *Terra Nova*, *13*(6), 463–470.

Bemmelen, R. W. VAN. (1949). *The Geology of Indonesia.* Govt. Print. Office. http://catalog.hathitrust.org/api/volumes/oclc/1517019.html

Bolton, S. H. (1987). Design Problems in Soil Liquefaction. *Journal of Geotechnical Engineering*, *113*(8), 827–845.

Butterfield, K., & Bolton, M. (2003). Modelling pore fluid migration in layered, liquefied soils. *Pacific Conf. on Earthquake Engineering, Christchurch, New Zealand*, *131*. http://db.nzsee.org.nz/PCEE/2003/View/Paper131s.pdf

Cipta, A., Robiana, R., Griffin, J. D., Horspool, N., Hidayati, S., & Cummins, P. R. (2017). A probabilistic seismic hazard assessment for Sulawesi, Indonesia.

Geological Society, London, Special Publications, *441*(1), 133–152.

Ekström, G., Nettles, M., & Dziewoński, A. M. (2012). The global CMT project 2004-2010: Centroid-moment tensors for 13,017 earthquakes. *Physics of the Earth and Planetary Interiors*, *200–201*, 1–9.

El Shamy, U., Zeghal, M., Dobry, R., Thevanayagam, S., Elgamal, A., Abdoun, T., Medina, C., Bethapudi, R., & Bennett, V. (2010). Micromechanical aspects of liquefaction-induced lateral spreading. *International Journal of Geomechanics*, *10*(5), 190–201.

Fang, J., Xu, C., Wen, Y., Wang, S., Xu, G., Zhao, Y., & Yi, L. (2019). The 2018 Mw 7.5 Palu earthquake: A supershear rupture event constrained by InSAR and broadband regional seismograms. *Remote Sensing*, *11*(11), 1–15.

GEMPA. (2018). *Plate rupturing or landslide? What caused the tsunami after the M7.5 earthquake N of Palu, Indonesia?* https://gempa.de/news/2018/9/28/tsunami-m75-earthquake-palu-indonesia/

Hall, R. (2014). Indonesian tectonics: subduction, extension, provenance and more. *Ndonesian Petroleum Association, Proceedings of the 38th Annual Convention, IPA14-G-360*, *August*, 1–43.

Hamilton, W. B. (1979). *Tectonics of the Indonesian region* (Issue 1078). US Govt. Print. Off.

Hazarika, H., Rohit, D., Pasha, S. M. K., Maeda, T., Masyhur, I., Arsyad, A., & Nurdin, S. (2021). Large distance flow-slide at Jono-Oge due to the 2018 Sulawesi Earthquake, Indonesia. *Soils and Foundations*, *61*(1), 239–255.

Hui, G., Li, S., Wang, P., Suo, Y., Wang, Q., & Somerville, I. D. (2018). Linkage between reactivation of the sinistral strike-slip faults and 28 September 2018 Mw7.5 Palu earthquake, Indonesia. *Science Bulletin*, *63*(24), 1635–1640.

Hungr, O., Leroueil, S., & Picarelli, L. (2014). The Varnes classification of landslide types, an update. *Landslides*, *11*(2), 167–194.

Indonesia, H. C. T. (2018). *Central Sulawesi Earthquake & Tsunami* (Vol. 7, Issue November). https://reliefweb.int/report/indonesia/central-sulawesi-earthquake-tsunami-humanitarian-country-team-situation-report-8-16

Ishihara, K. (1985). Stability of natural deposits during earthquakes. *Proc. 11th International Conference on Soil Mechanics and Foundation Engineering, San Francisco, 1,* 321–376.

Japan International Cooperation Agency (2019). *Report of the technical committee on The 2018 Sulawesi earthquake, Indonesia*.

Kawakita, S., Asahina, D., Takemura, T., Hosono, H., & Kitajima, K. (2020). Effect of hydraulic and mechanical characteristics of sediment layers on water film formation in submarine landslides. *Progress in Earth and Planetary Science*, *7*(1).

Kokusho, Takeji, & Kojima, T. (2002). Mechanism for Postliquefaction Water Film Generation in Layered Sand. *Journal of Geotechnical and Geoenvironmental Engineering*, *128*(2), 129–137.

Kokusho, T. (1999). Water film in liquefied sand and its effect on lateral spread. *Journal of Geotechnical and Geoenvironmental Engineering*, *125*(10), 817–826.

Kusumawardani, R., Chang, M., Upomo, T. C., Huang, R., Fansuri, M. H., & Prayitno, G. A. (2021). Understanding of Petobo liquefaction flowslide based on site reconnaissance. *Landslides.* https://doi.org/10.1007/s10346-021-01700-x.

Liu, P. L. F., Higuera, P., Husrin, S., Prasetya, G. S., Prihantono, J., Diastomo, H., Pryambodo, D. G., & Susmoro, H. (2020). Coastal landslides in Palu Bay during 2018 Sulawesi earthquake and tsunami. *Landslides*, *17*(9), 2085–2098.

May, M. E. I., Kacem, J., & Dlala, M. (2009). Liquefaction susceptibility mapping using geotechnical laboratory tests. *International Journal of Environmental Science and Technology*, *6*(2), 299–308.

Metallic Minerals Exploration Agency. (1973). *Report on Geological Survey of Central Sulawesi, Indonesia.pdf.*

Mikami, T., Shibayama, T., Esteban, M., Takabatake, T., Nakamura, R., Nishida, Y., Achiari, H., Rusli, Marzuki, A. G., Marzuki, M. F. H., Stolle, J., Krautwald, C., Robertson, I., Aránguiz, R., & Ohira, K. (2019). Field Survey of the 2018 Sulawesi Tsunami: Inundation and Run-up Heights and Damage to Coastal Communities. *Pure and Applied Geophysics*, *176*, 3291–3304.

Miyashiro, A. (1961). Evolution of Metamorphic Belts. *Journal of Petrology*, *2*(3), 277–311.

National Agency of Disaster Management, Gempa Bumi Sulteng. (n.d.). Retrieved January 15, 2021, from https://bnpb.go.id/geoportal.html

Omori, F. (1894). On the aftershocks of earthquakes. *Journal of the College of Science, Imperial University of Tokyo*, *7*, 111–200.

Patria, A., & Putra, P. S. (2020). Development of the Palu–Koro Fault in NW Palu Valley, Indonesia. *Geoscience Letters*, *7*(1), 1–11.

Sarsito, D. A., Susilo, Simons, W. J. F., Abidin, H. Z., Sapiie, B., Triyoso, W., & Andreas, H. (2017). Rotation and strain rate of sulawesi from geometrical velocity field. *AIP Conference Proceedings*.

Sassa, S., & Takagawa, T. (2019). Liquefied gravity flow-induced tsunami: first evidence and comparison from the 2018 Indonesia Sulawesi earthquake and tsunami disasters. *Landslides*, *16*(1), 195–200.

Socquet, A., Hollingsworth, J., Pathier, E., & Bouchon, M. (2019). Evidence of supershear during the 2018 magnitude 7.5 Palu earthquake from space geodesy. *Nature Geoscience*, *12*, 192–199.

Socquet, A., Simons, W., Vigny, C., McCaffrey, R., Subarya, C., Sarsito, D., Ambrosius, B., & Spakman, W. (2006a). Microblock rotations and fault coupling in SE Asia triple junction (Sulawesi, Indonesia) from GPS and earthquake slip vector data. *Journal of Geophysical Research: Solid Earth*, *111*(8), 1–15.

Socquet, A., Simons, W., Vigny, C., McCaffrey, R., Subarya, C., Sarsito, D., Ambrosius, B., & Spakman, W. (2006b). Microblock rotations and fault coupling in SE Asia triple junction (Sulawesi, Indonesia) from GPS and earthquake slip vector data. *Journal of Geophysical Research: Solid Earth*, *111*(8), 1–15.

Surono, & Sukarna, D. (1996). Sedimentology of the Sulawesi molasse in relation to Neogene tectonics, Kendari area, eastern Indonesia. *Proceedings of the 6th International Congress of Pacific Neogene Stratigraphy and IGCP355,* 57–72.

USGS. (2018). *United States Geological Survey*. https://www.usgs.gov/

van Leeuwen, T., Allen, C. M., Elburg, M., Massonne, H. J., Palin, J. M., & Hennig, J. (2016). The Palu Metamorphic Complex, NW Sulawesi, Indonesia: Origin and evolution of a young metamorphic terrane with links to Gondwana and Sundaland. *Journal of Asian Earth Sciences*, *115*, 133–152.

van Leeuwen, T. M., & Muhardjo. (2005). Stratigraphy and tectonic setting of the Cretaceous and Paleogene volcanic-sedimentary successions in northwest Sulawesi, Indonesia: Implications for the Cenozoic evolution of Western and Northern Sulawesi. *Journal of Asian Earth Sciences*, *25*(3), 481–511.

Villeneuve, M., & Gunawan, W. (2002). Geology of the central Sulawesi belt (eastern Indonesia): constraints for geodynamic models. *International Journal of Earth Science*, *91*(3), 524–537.

Watkinson, I. M., & Hall, R. (2017). Fault systems of the eastern Indonesian triple junction: Evaluation of Quaternary activity and implications for seismic hazards. *Geological Society Special Publication*, *441*(1), 71–120.

Watkinson, I. M., & Hall, R. (2019). Impact of communal irrigation on the 2018 Palu earthquake-triggered landslides. *Nature Geoscience*, *12*(11), 940–945.

Yang, Z., & Elgamal, A. (2001). Sand Boils and Liquefaction--Induced Lateral Deformation. *15th International Conference on Soil Mechanics and Geotechnical Engineering*, *1989*, 345–350.

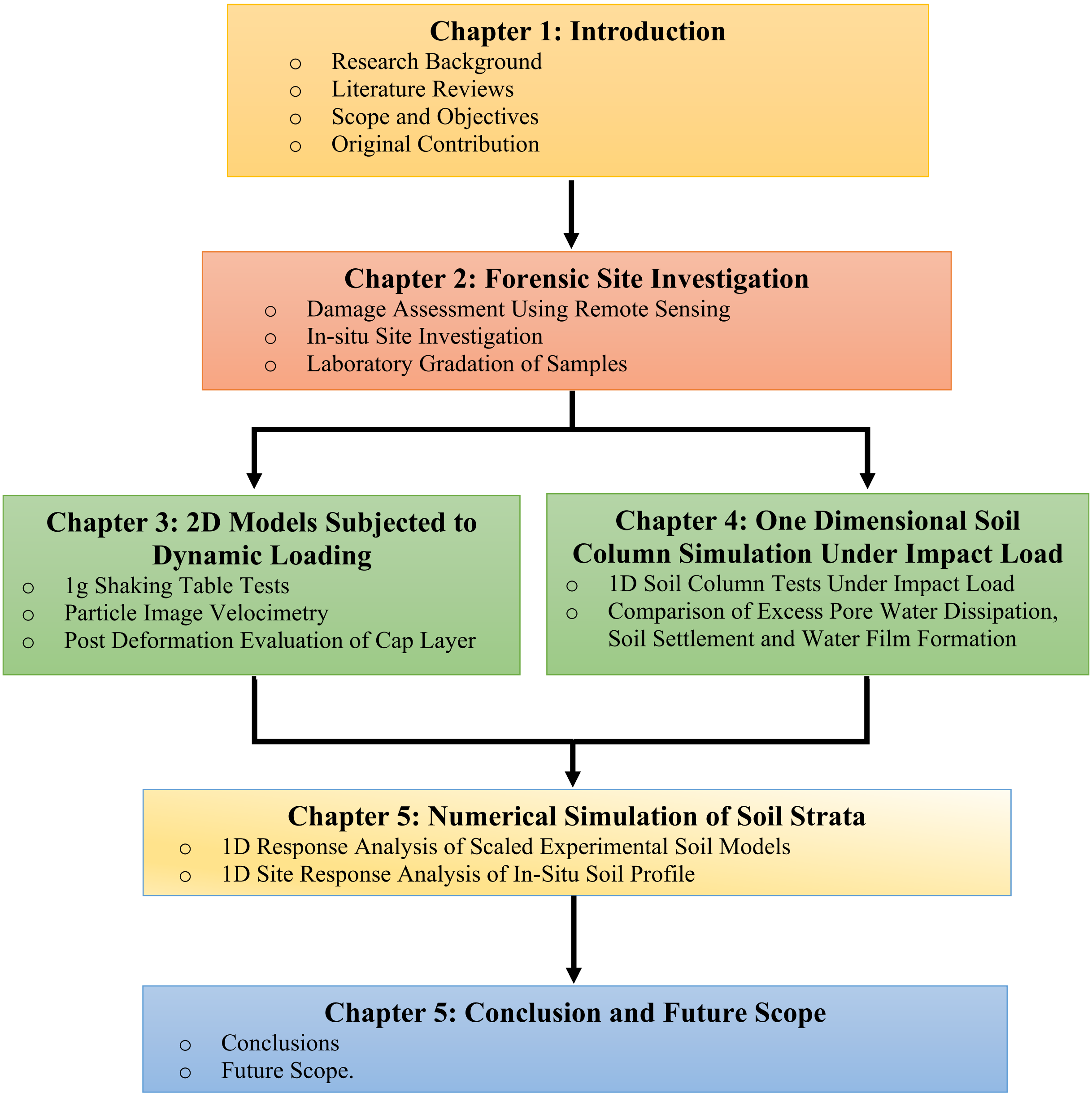
Chapter 1: Introduction
Research Background
Literature Reviews
Scope and Objectives
Original Contribution
Chapter 2: Forensic Site Investigation
Damage Assessment Using Remote Sensing
In-situ Site Investigation
Laboratory Gradation of Samples
Chapter 3: 2D Models Subjected to Dynamic Loading
1g Shaking Table Tests
Particle Image Velocimetry
Post Deformation Evaluation of Cap Layer
Chapter 4: One Dimensional Soil Column Simulation Under Impact Load
1D Soil Column Tests Under Impact Load
Comparison of Excess Pore Water Dissipation, Soil Settlement and Water Film Formation
Chapter 5: Numerical Simulation of Soil Strata
1D Response Analysis of Scaled Experimental Soil Models
1D Site Response Analysis of In-Situ Soil Profile
Chapter 5: Conclusion and Future Scope
Conclusions
Future Scope.

CHAPTER 2

FORENSIC SITE INVESTIGATION

2.1 INTRODUCTION

The flowslides triggered due to the 2018 Sulawesi earthquake were of unique in nature owing to the sheer size of the area engulfed, the gentle gradient of the ground in which it occurred and the time of triggering. Although the precise reason behind the triggering of this large-scale geotechnical disaster is yet unknown, many hypotheses have been proposed by researchers on the exact cause of such massive flowslides. One of them is the water film formation due to liquefaction under the low permeable cap layers, while the other proposes the rupture of an underground aquifer, supplying additional water to the already liquified surface layer, sustaining the flow for long-distance and duration (JICA, 2018). Alternatively, the existence of a shallow water table beside the seepage from unlined irrigation canal destabilizing the already metastable alluvial fans was also proposed (Watkinson & Hall, 2019; Bradley et al., 2019). However, no flowslides were observed in other locations in Palu despite the presence of shallow water table, unlined canal and rice fields, therefore, this theory alone cannot be generalized for all the sites. Furthermore, assuming that the flowslides were triggered by the formation of water film, it is required that the water film is formed over a large are which necessitates, the presence of a continuous cap layer over a large area.

Therefore, to make clear the mechanism and identify the site geological and geotechnical factors which might have been involved in the triggering of the flowslides, detailed field investigations were conducted. To assess the damage caused the earthquake, aerial reconnaissance was conducted using unmanned aerial vehicle

(UAV). Investigation of soil profiles through vertical cliff walls near the head scarp was performed in Jono Oge, while geological and geotechnical investigation of the soil lithology in the trenches excavated in Sibalaya (Okamura et al., 2020; JICA, 2019) was also conducted. The soil profile of the failed areas was thoroughly investigated from the trenches excavated at the site, and soil samples were collected from different elevations in the trenches. Furthermore, to assess the in-situ soil strength, portable dynamic cone penetration tests (PDCPT) were conducted at few locations and compared with the actual soil profile. The N-values obtained from PDCPT sounding (Nd) were then converted to Standard Penetration Test (SPT) N values using the empirical equations available in Takase and Sasada (2013). The tests were performed according to JGS 1433-2012. The N values were then used to define the compactness of the soil strata as follows:

Table 2.1 Soil compactness based on SPT N values (after Teng, 1962).

Compactness	**SPT N (blows per foot)**
Very loose	0-4
Loose	5-10
Medium	11-30
Dense	31-50
Very Dense	>51

The slide areas were all located along the edges of Palu valley, where the new alluvial fans meet the old alluvial fan deposits of Palu river. Landslide in Balaroa (northwest side of Palu valley) occurred on a moderate to gentle ground with average slope of 4% and partially or fully damaged surrounding residential buildings. The rest of three flowslides Petobo, Jono Oge and Sibalaya are situated in the east side of Palu valley and distributed within the 25 kilometers of Palu city. Figures 2.1 a, b, c and d depict extent of damage to housing structures in Balaroa, Petobo, Jono Oge and Sibalaya respectively (BNPB).

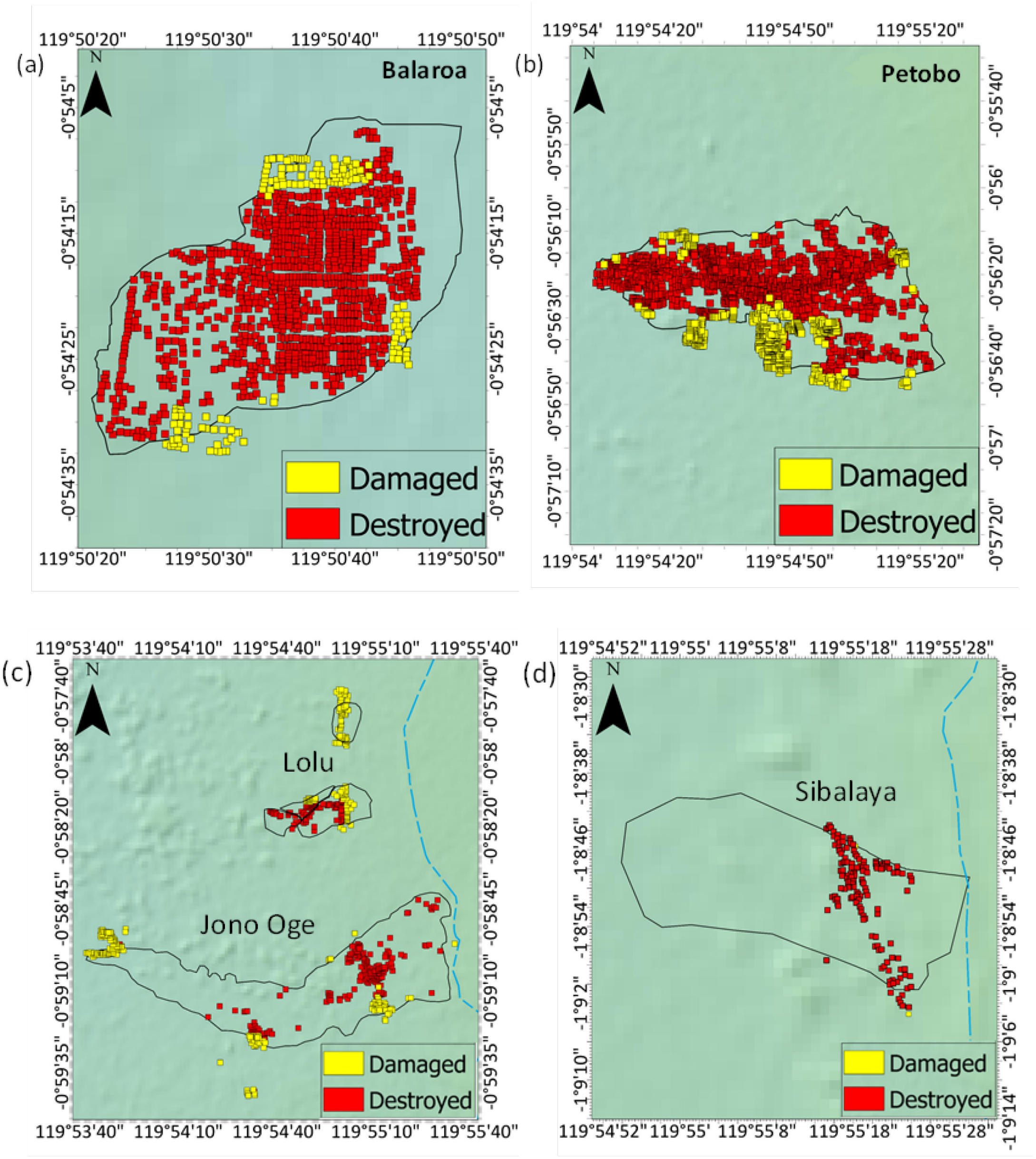

Figure 2.1 Extent of damage to housing infrastructure due to flowslides: (a) Balaroa, (b) Petobo, (c) Jono Oge and Lolu and (d) Sibalaya (Modified from BNPB ArcGIS Map Service, Copernicus Data Source).

2.2 DAMAGE ASSESSMENT USING REMOTE SENSING

The damage due to the liquefaction induced flowslides was evaluated by creating Normalized Differential Vegetation Index (NDVI) image from the Landsat 8 data (Global Change Master Directory (GCMD), 2020). NDVI is a graphical index which provides the measure of green vegetation, where the value from -1 to 1 are defined in the index, with values towards positive 1, define good plant health and vegetation and vice versa. The calculation is made from individual measurements as shown below:

$$NDVI = \frac{(NIR - Red)}{(NIR + Red)}$$

where, NIR is the spectral reflectance measurement acquired in near-infrared regions and Red is for the red region (visible). The before and after NDVI image for the Palu valley shown in Figure 2.2. Figure 2.2 here, shows two images, one taken on September 23, 2018 (before the earthquake) and the later on October 2, 2018 (after the earthquake). The Petobo, Jono Oge and Sibalaya locations had significant area covered with rice paddy and coconut plantations which were completely destroyed and displaced due to the flowslides. This change in vegetation cover is clearly visible from the contrasting images, where before the earthquake these areas show a healthy green cover with NDVI index value nearing (+)1 while after the earthquake NDVI index of these areas is towards (-)1.

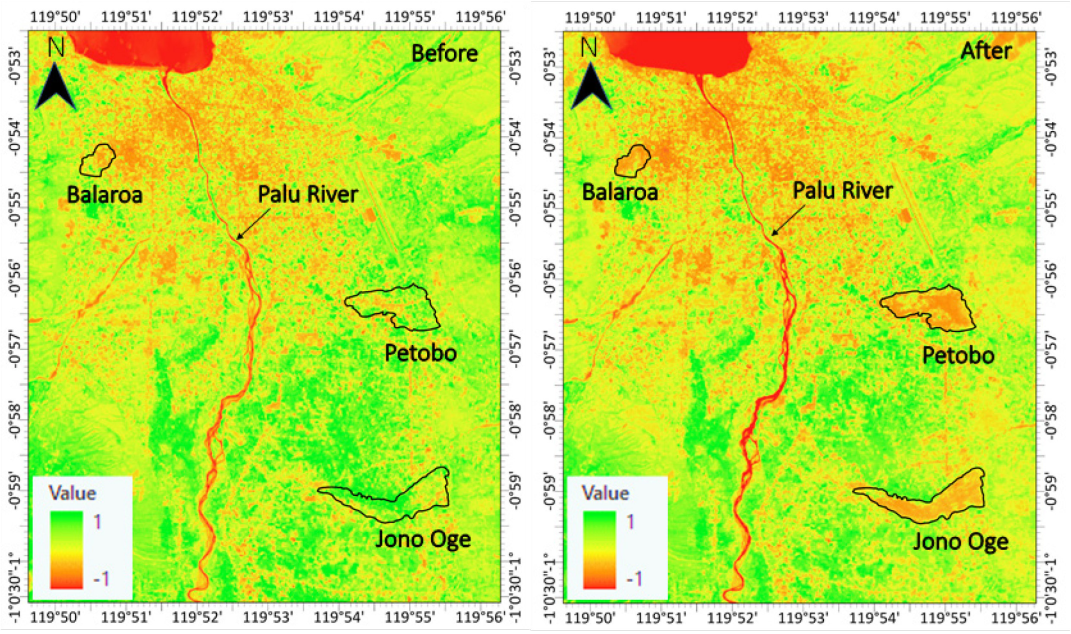

Figure 2.2 NDVI graphic representation of Palu Valley before (September 23, 2018) and after (October 2, 2018) the 2018 Sulawesi earthquake.

2.3 FLOWSLIDE AT BALAROA

The Balaroa flowslide site was situated towards the seaside of the Palu valley. It had a dense urban setting, due to which the damage to human lives was much higher as compared to Jono Oge and Sibalaya which had larger area coverage, also the direction of flow was opposite to the latter two and Petobo. In addition to it, there was no canal structure aligned near this location. The Balaroa flowslide engulfed an area of 0.4 km^2 with a destruction of more than 1300 structural units. Balaroa site also had a very gentle ground slope of less than 5% on an average before the flowslide (Kiyota et al., 2020) but comparatively steeper than other locations. Our team could perform limited reconnaissance of this site due to access issues and time constraints. Figure 2.3 a and b depicts the before and after images of the Balaroa site respectively. The site could be divided into two zones, tensile zone and compression zone. The flowslide started from the tensile zone with the ground movement in large blocks with the overlying housing structures, which then stacked up in the compression zone.

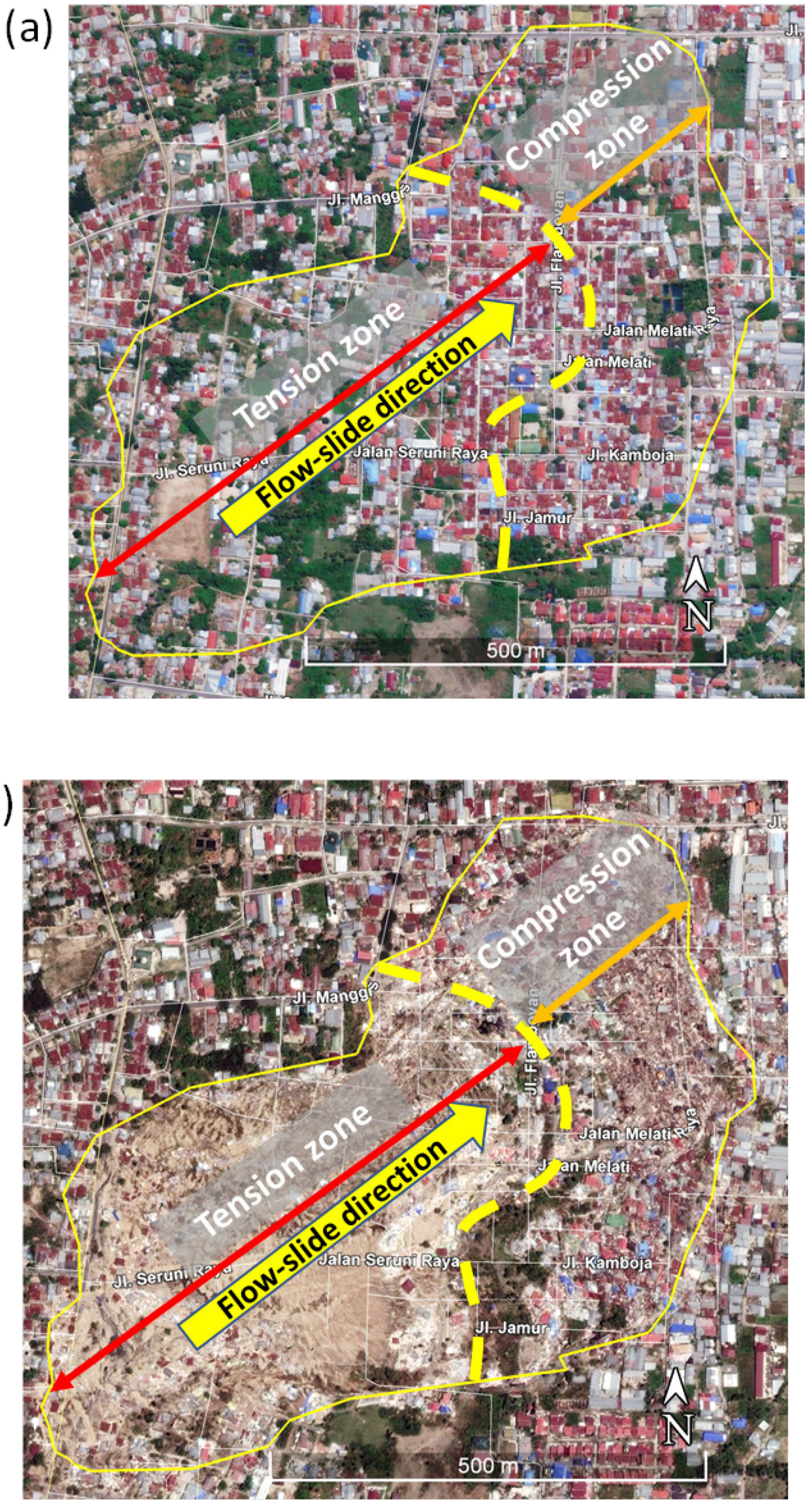

Figure 2.3 Aerial view of Balaroa flowslide site: (a) before (March 11, 2018) and (b) after (March 21, 2019) the earthquake (Modified from Google Earth).

A 3D image generated from the drone survey data analysis using Agisoft PhotoScan Professional software, is shown in Figure 2.4 a. The extent of vertical ground displacement could be ascertained from Figure 2.4 b, in which the height of the vertical soil profile near the crown appears to be around than 3 times the normal ground level structures present on the edge from visual observation. The height of the partially demolished housed is assumed as 1N, where N is in meters. The vertical reduction in ground elevation seemed to be around 3 times (3N) the height of the house. Furthermore, the site had a very shallow water table which was almost at the surface as observed by the authors during the survey. This could be confirmed by the presence of natural ground water gushing out from the debris (Figure 2.4 c). Furthermore, it confirms the theory of presence of an artisan aquifer by Kiyota et. al., (2020).

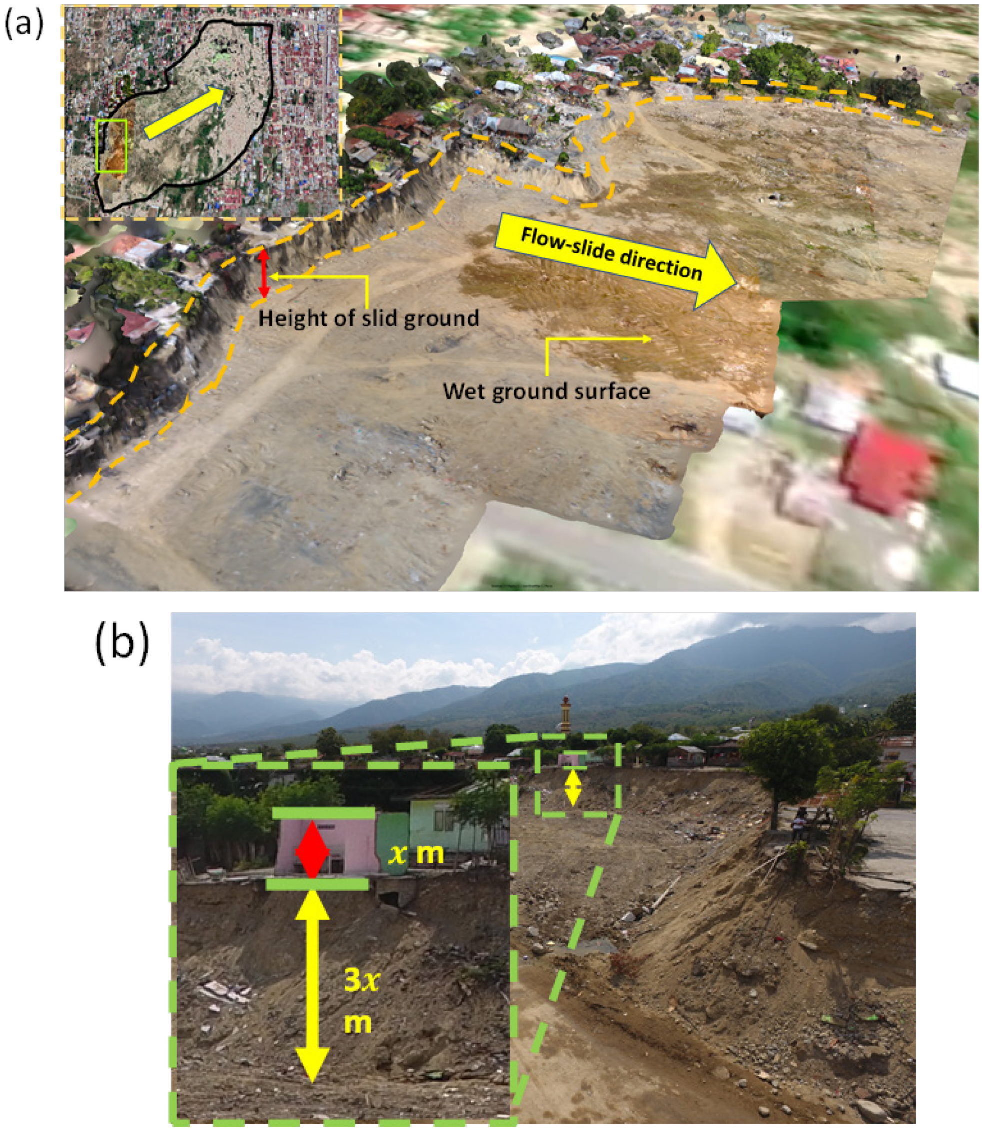

(c)

Figure 2.4 Site investigation results from Balaroa: (a) 3D model generated from drone survey. (b) extent of vertical ground displacement and (c) water gushing from underground stream (Survey done on November 3, 2018).

2.4 FLOWSLIDE AT PETOBO

Petobo site was located near the Palu airport and had a semi-urban setting like with houses and paddy fields, while the hydrological features were similar to Jono Oge and Sibalaya. The Petobo flowslide devoured an area of about 1.81 km^2 and destroyed more than 1900 housing structures. The site was more densely populated as compared to Jono Oge and Sibalaya and had a gentle ground slope profile of less than 3% in average. The surficial soil of Petobo site consisted of old alluvium fan deposit on the upstream part while the downstream part was composed of alluvial deposit, flood deposit and the old river channel deposit which could also be classified as fluvial deposit (Kusumawardani et al., 2021). Here in Figure 2.5 a and b the satellite images of the site at different time frames are shown to represent the change in geomorphology and ground condition. Here too, the site had two sections of the flowslide where the upstream area saw abrupt ground displacement horizontally as well as vertically and the downstream area observed an increase in elevation along with the accumulation of debris from the upstream.

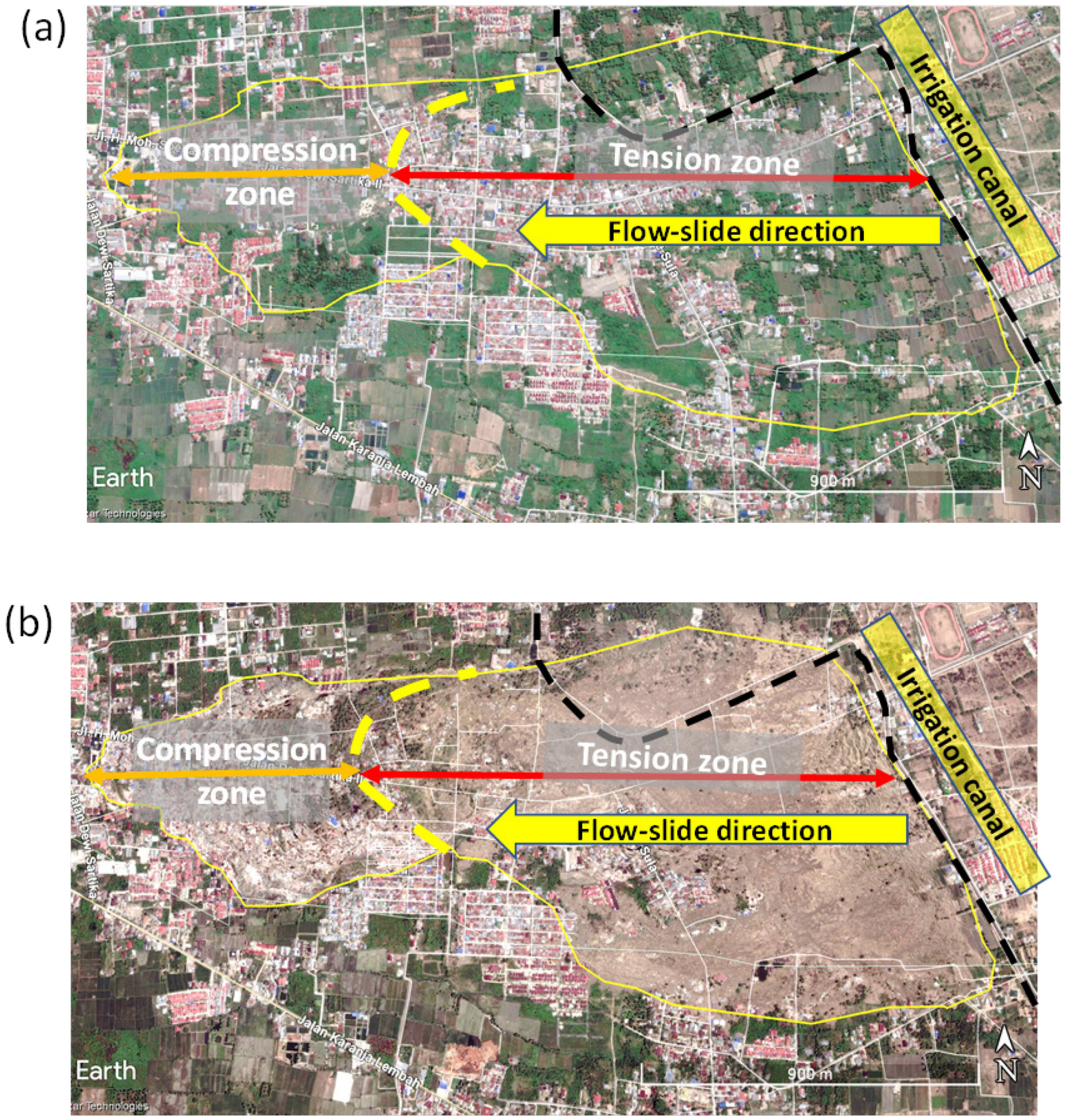

Figure 2.5 Petobo flowslide site: (a) Before (August , 2018) and (b) after (October 2, 2018) the earthquake (Modified from Google Earth).

Figure 2.6a shows the aerial view of the site, which highlights the extent of tensile cracks developed near the head scarp or crown. It also signifies an incremental slip of the ground surface in large blocks which is termed as slump deformation. The extent of vertical decrease in elevation could also be seen in Figure 2.6 b where the paddy field was partially intact while a major part had slid down. It has been reported that, the elevation drop near the crown of the site was around 5-8m, while the elevation increased from 4-10m in the compression zone due to accumulation of the debris and bulging due to forward thrust from the sliding. In addition to it, presence of artisan aquifer and ponded water after the flowslide have also been observed in the Petobo site (Kusumawardani et al., 2021).

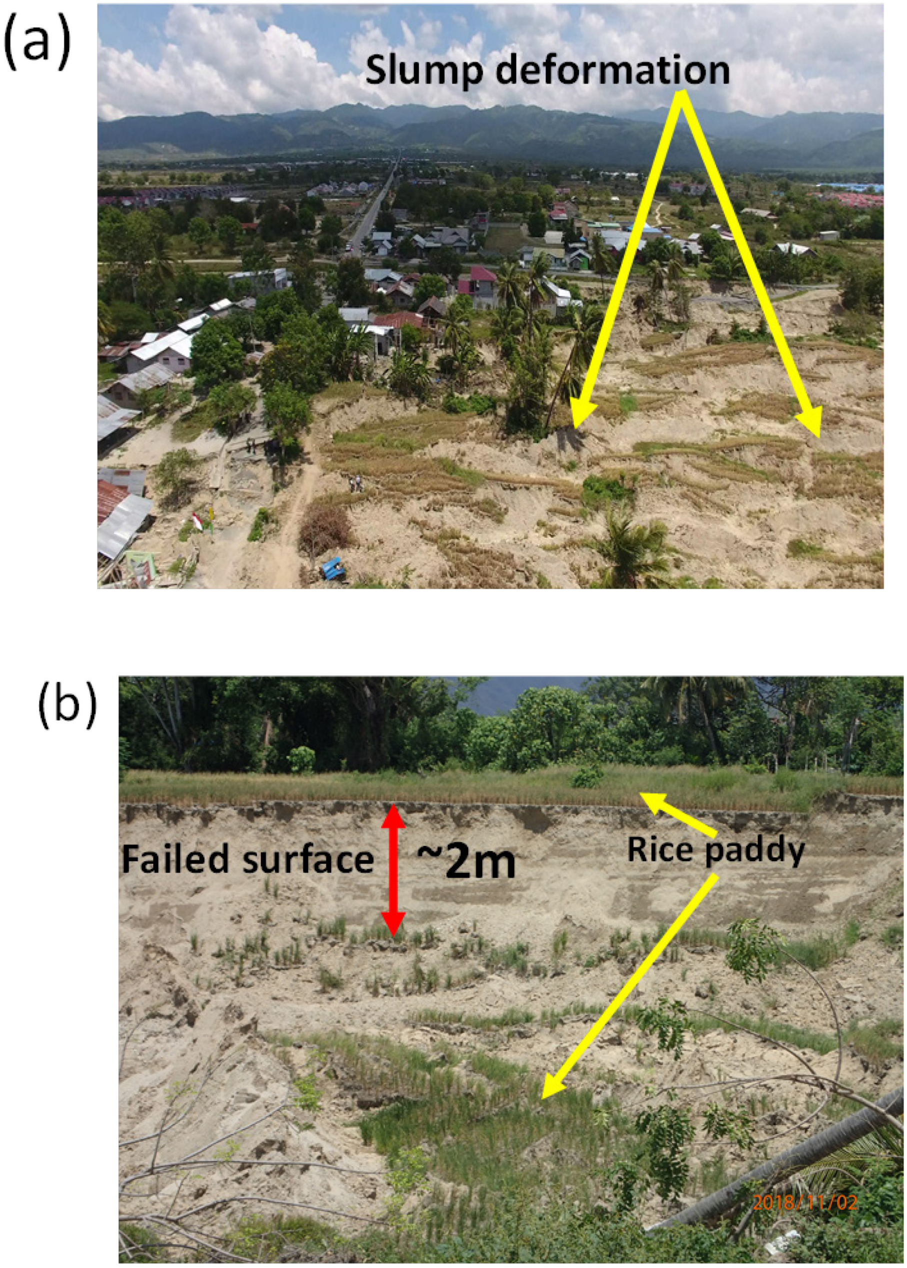

Figure 2.6 Images from Petobo flowslide site: (a) aerial view of the crown area showing slump deformation (, (b) vertical soil profile of location near crown (Survey done on November 2, 2018).

2.5 FLOWSLIDE AT JONO OGE

Jono Oge village was considered the worst damaged, with respect to the ground movement observed. Around 2.095 km^2 of residential and agricultural area was destroyed due to the flowslide and mudflow originating from the breached canal which was flowing at full capacity during the earthquake (BNPB, 2018). The surface geology of Jono Oge was similar to Petobo with part old alluvium fan deposit on the upstream, alluvial deposit, flood deposit and old river channel deposit on the downstream (Kusumawardani et al., 2021; Mason et al., 2021). The flowslide occurred on a very gentle slope of around 4% on an average (Hazarika et al., 2021). Our team performed aerial reconnaissance using a drone for damage assessment and a comprehensive view of the site. Although the survey could not cover the vast area of the site, but it was instrumental in identifying many key characteristics of the flowslide as well as the destruction caused by it. An orthomosaic image was prepared using the drone images collected from the aerial survey as shown in Figure 2.7. The tensile cracks appear from the crest of the flowslide, which then diminish as we go down towards the middle of the flowslide zone in the SW-direction. Also, it is important to note the breach of the canal near the crest of the slide, which shows sign of soil erosion due to the flow of water from the canal during the earthquake. This breach intensified the damage due to the slide by creating mudflow in the major part of the site. Furthermore, the stream flowing along right bank of the slide also seems to be breached with a lot of sediment residues being deposited outside its usual streaming channel. This breach was larger than the canal breach and seems to be the most obvious cause of failure of the bridge connecting the site by scouring of its abutment foundation.

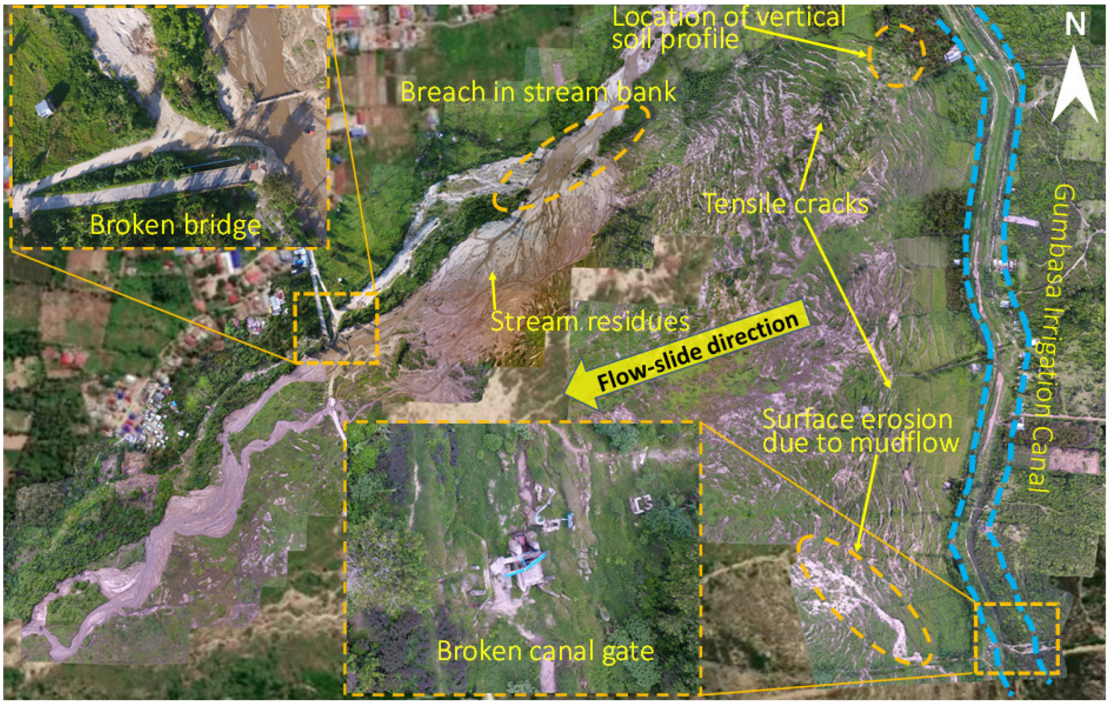

Figure 2.7 Orthomosaic image of the Jono Oge site with key observations (Surveyed during 2/11/2018) (Map not to scale).

Furthermore, the geomorphological change to the site was evaluated from the pre- and post-earthquake terrain elevation profile of the area (Figure 2.8 a and b). The pre-earthquake elevation profile was obtained from the open access DEMNAS data source of Geospatial Information Agency (BIG) of Indonesia, while the post-earthquake elevation data was obtained from the Digital Elevation Model (DEM) generated from drone image analysis conducted. In Figure 2.8 a, the profile has a gentle slope with consistently decreasing elevation profile while in Figure 2.8 b, a sudden sump is observed in the tension zone from where the ground sliding occurred. While an increase in elevation can be seen in the downstream side, which is due to the accumulation of the debris and soil blocks along with humping of ground due to forward thrust provided by the slide.

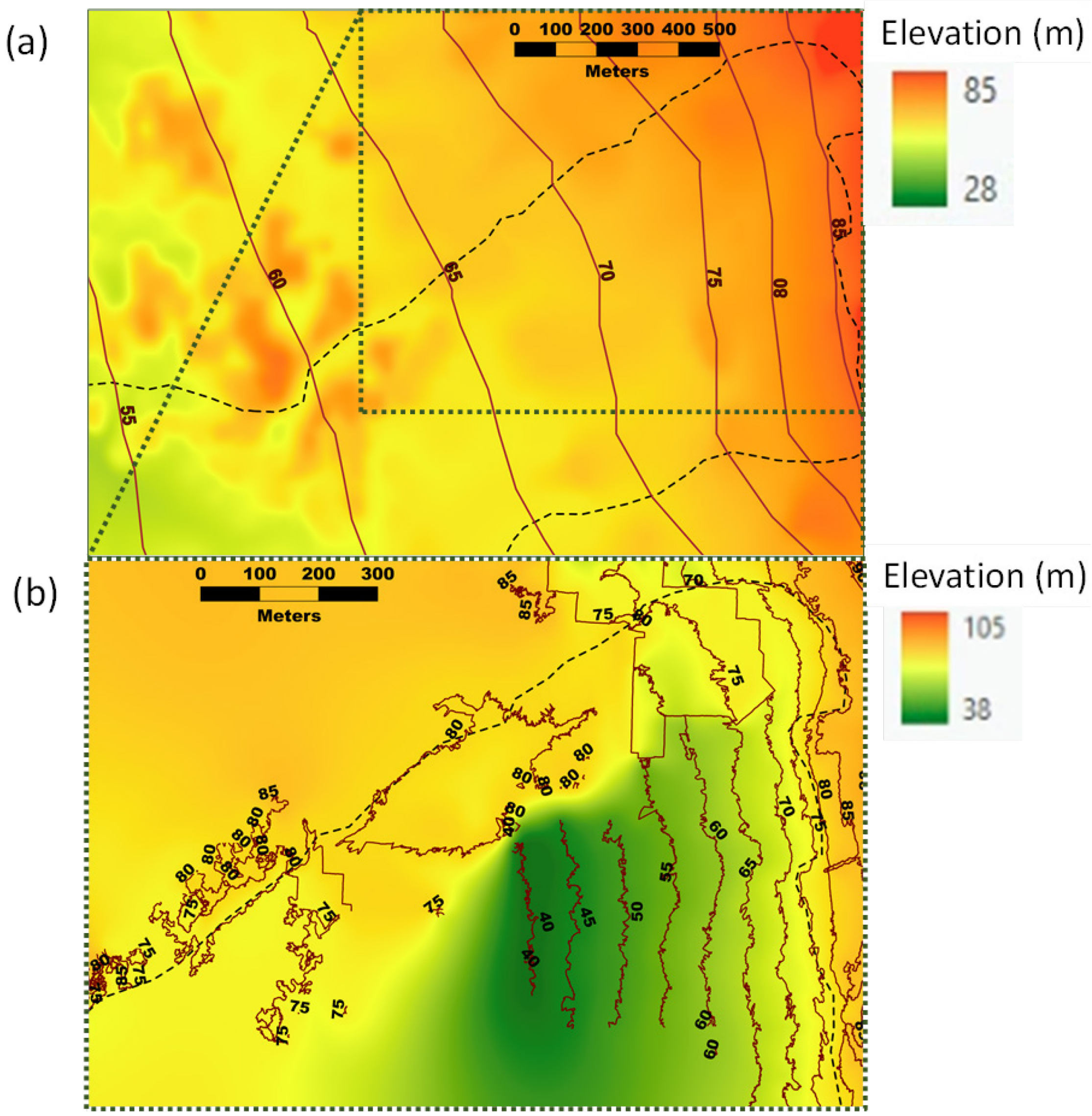

Figure 2.8 Raster elevation profile of the Jono Oge flow-slide site: (a) before earthquake and (b) after the earthquake (Survey performed on 2/11/2018).

2.5.1 In-situ tests

In order to make clear the mechanism and progression of long-distance flowslide at Jono Oge, we performed in-situ tests using the Portable Dynamic Cone Penetrometer Tests (called hereafter PDCPT), and also collected soil samples from the flowslide sites. These field tests, together with laboratory testing of the collected soil samples and visual observation of site condition, can provide valuable information on subsurface properties. Fig. 2.9 shows the locations where soil samples were collected and PDCPT were conducted. As can be seen from the figure, the location of the PDCPTs (PDCPT1, PDCPT4, PDCPT5, PDCPT6, PDCPT8) were selected such that, they cover some locations within the flowslide zones and outside of the flowslide zone in North-South (alongside the damaged main access road connecting North to south of Jono-Oge) and South-North-East directions. Furthermore, some PDCPTs were also conducted in the areas upstream of the Jono Oge flowslide site to compare the in-situ bearing strength with the failed area. These were located around 1.5 km away from the head scarp as shown in Figure 2.10. Figure 2.11 here shows the setup of PDCPT. In this test, a hammer weighing 5±0.05kg is dropped from a height of 500 mm ± 10 and the number of blows for a 100mm penetration are recorded as N_d. The PDCPT N_d values were then converted to SPT N values based on the correlations provided in Takase and Sasada (2013).

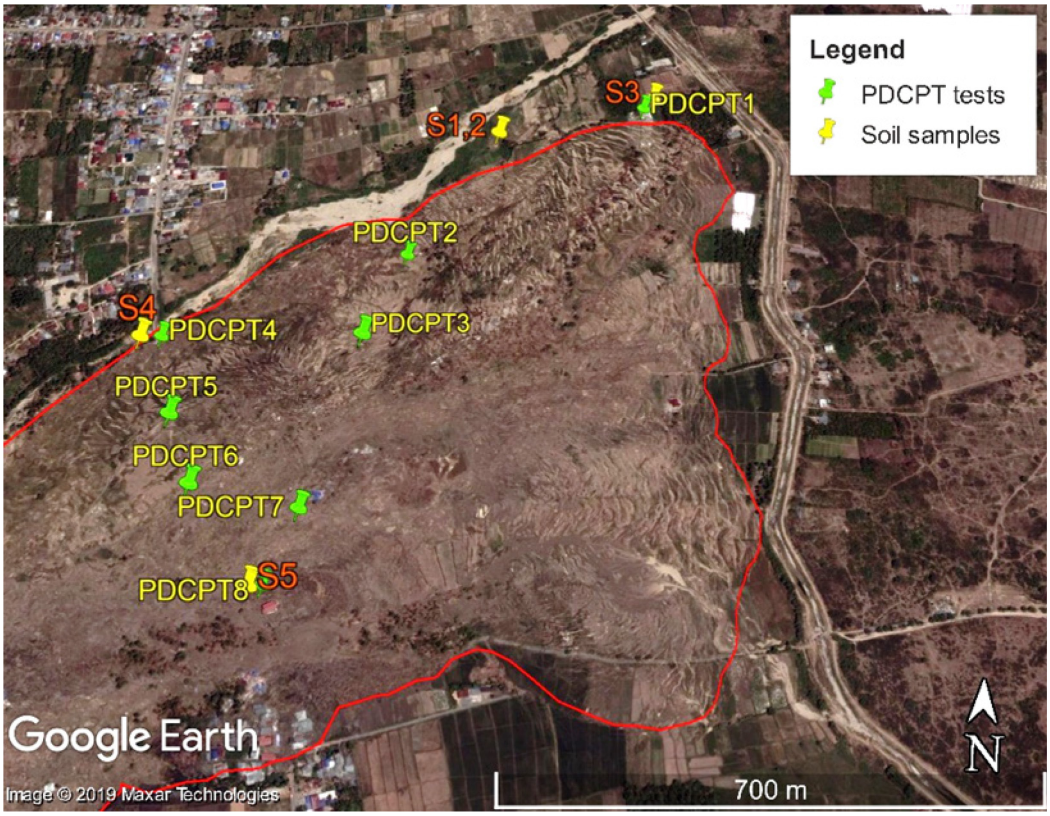

Figure 2.9 Locations of the PDCPT and collected soil samples at Jono-Oge.

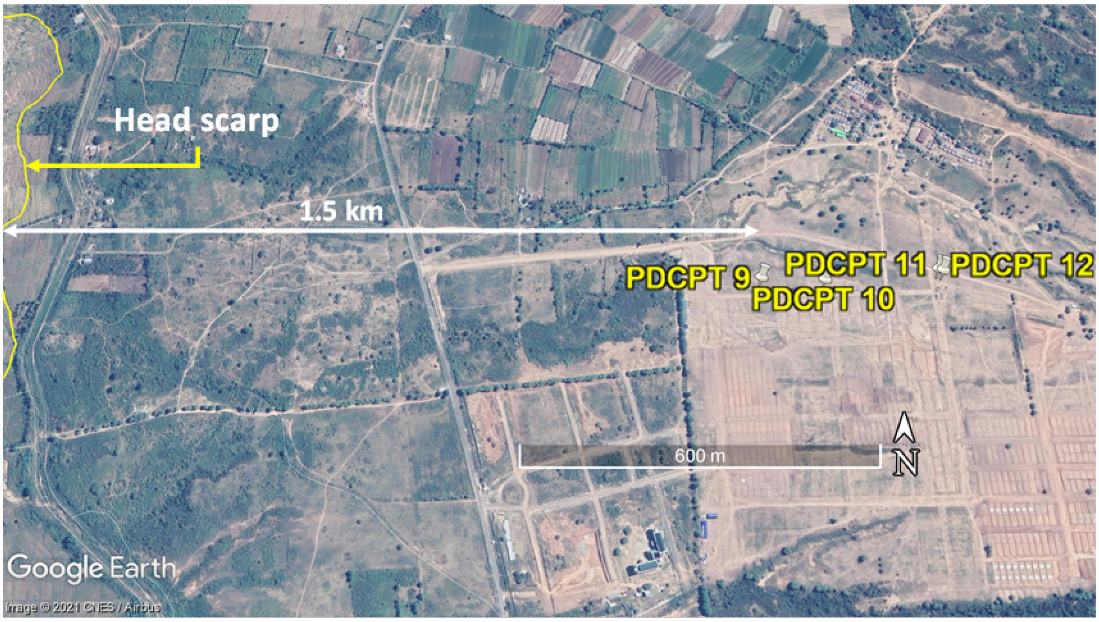

Figure 2.10 Locations of the PDCPTs conducted in the un-failed area, upstream of Jono Oge flowslide site (modified from Google Earth).

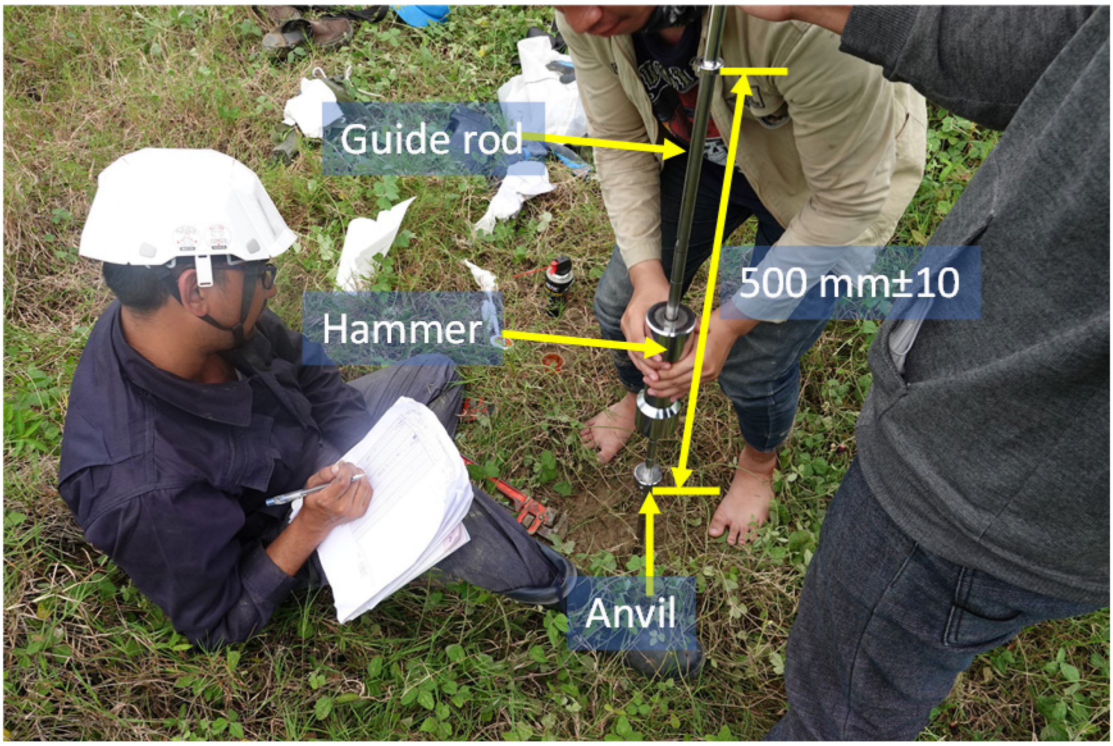

Figure 2.11 Typical test setup of PDCPT in field.

Results from the tests conducted outside the flowslide zone

PDCPT1 was conducted outside of failure zone on the margin far from extensional cracks. Since the original stratification of ground is well preserved outside of flowslide area, the result of PDCPT1 can be a good benchmark for evaluating the results of PDCPT tests within the failure zones. Fig. 2.12a, shows the aerial view of PDCPT1 location which was conducted on the agriculture farm (paddy fields and tomato farm) and the resulting N-value which vary with depth. A clear decrease in the N value for the soil layers below 3.5 m would be an indication of loose liquefiable layers. The very high ground water level (which was higher than water level at the time of testing G.W. L=2.3m) also contributes to increasing the risk of liquefaction in shallow underground layers.

In order to identify the soil profile of PDCPT1, an image of a cliff in neighboring extensional crack with depth of around 2.5 m is shown in Fig. 2.12b. Soil stratification is clearly visible and less disturbed due to flowslide downhill. The surface layer is composed of 10-20 cm of organic soil followed by 30-40 cm of clay and silty clay layer. The underlying 10-20 cm thick silty sand layer is sandwiched between upper clayey layer and lower 10-20 cm thick clay silt layer. Below the silty layer, there were several layers of sandy and gravelly sand layers which appeared to be affected by liquefaction in underlying layers. The presence of these low permeable layers at the top might have created a possible formation of water film between them and the underlying gravelly sand layers as described in Kokusho (1999). Some soil samples were collected from the exposed parts of extensional cracks, and basic physical properties of soils in the stratified layers were determined.

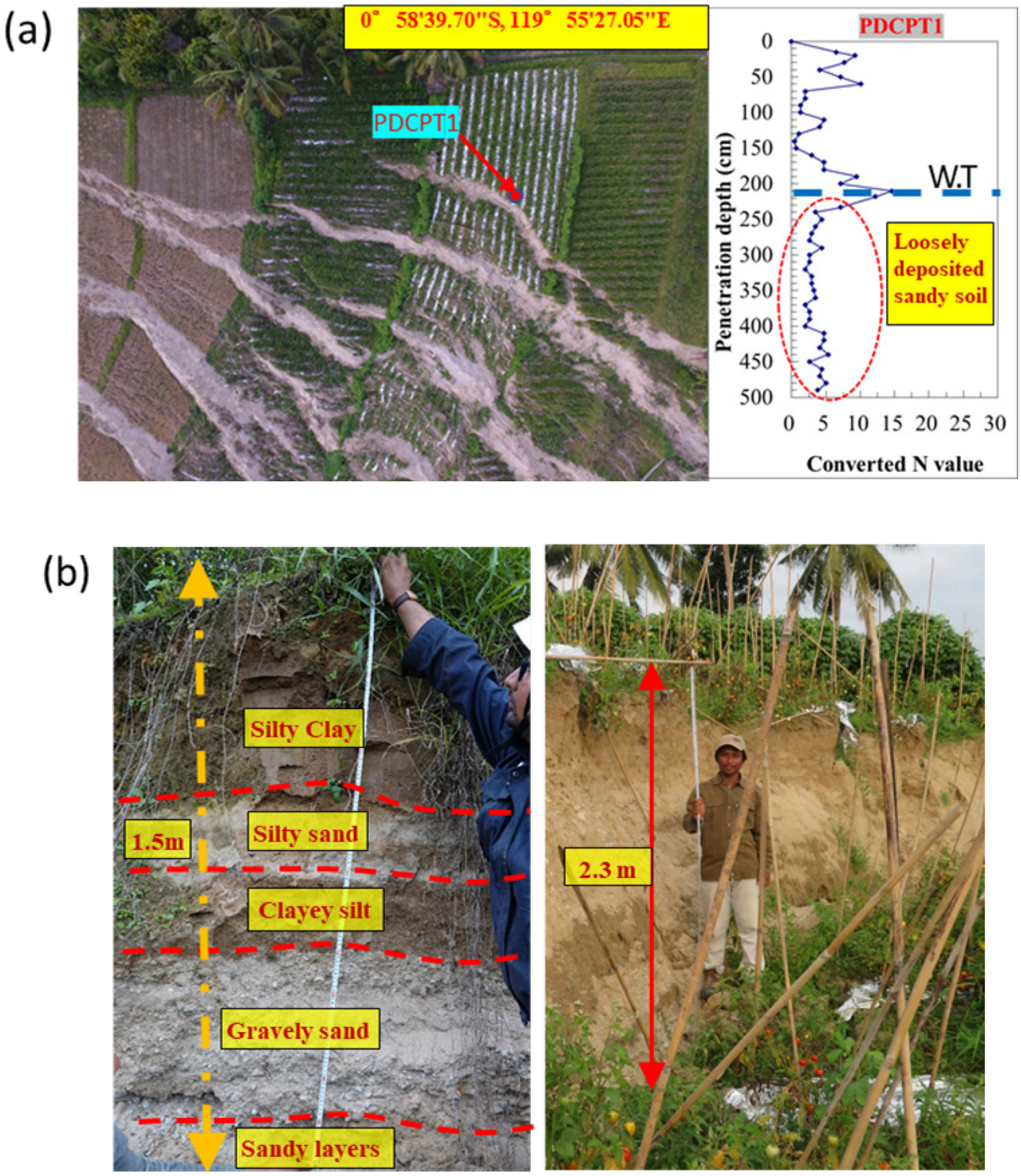

Figure 2.12 PDCPT conducted within Zone (I) (a) location and (b) test result at PDCPT1 (c) Profile of exposed soil layers at cliff created by extensional cracks.

PDCPT9~PDCPT12 were conducted around 1.5 km from the head scarp of the Jono Oge flowslide site. The N value vs depth profile for the PDCPTs is shown in Figure 2.13. The location of these PDCPTs seemed undisturbed from the flowslide and was selected as one of the planned resettlement site for the displaced people. As observed from the converted N values the subsoil can be classified as medium soil according to

(Teng, 1962). As we go upstream from the head scarp the soil bearing strength increases as seen chronologically from PDCPT 9 to 12, this was one of the possible reasons no damage in this area. Furthermore, there was no presence of shallow water table as observed in the flowslide area.

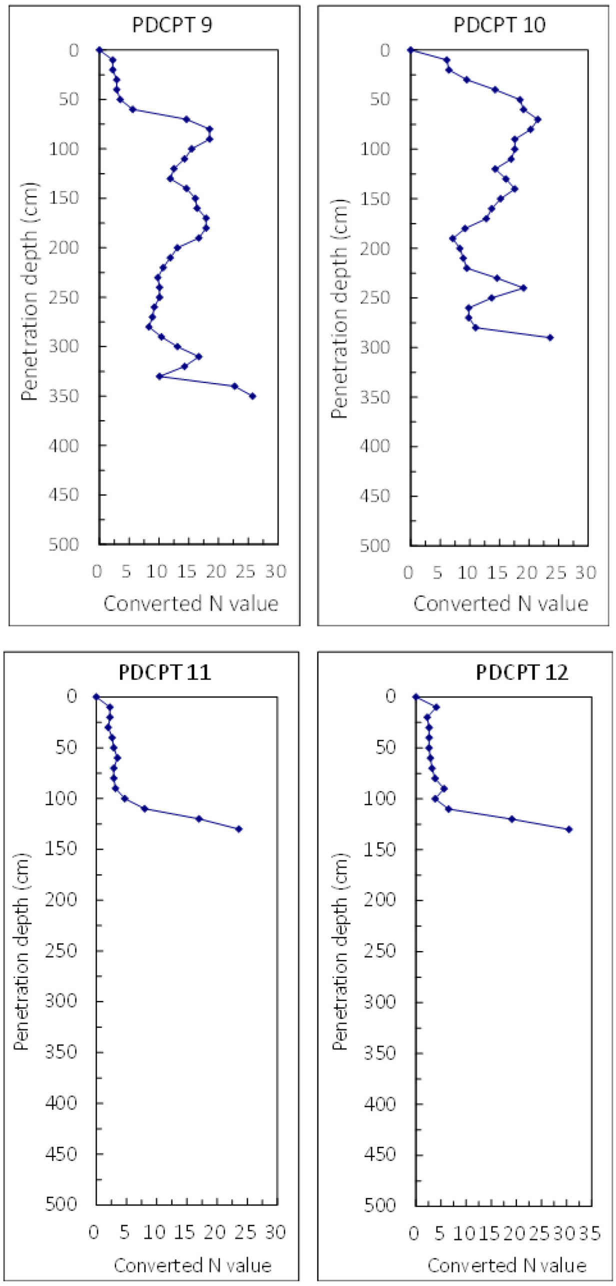

Figure 2.13 Converted N value vs depth profile for PDCPT 9, 10, 11 and 12.

Results from the tests conducted within the flowslide zone

As shown in Fig. 2.9, the PDCPT4, 5, 6, 7 and 8 were conducted alongside the damaged road, which connects the North and South of flowslide region. The locations and results of PDCPT4, 5, 6, 7 and 8 are shown in Fig. 2.14 a ~ e. PDCPT4 was conducted right next to collapsed bridge in the North of Jono-Oge (Fig. 2.14a). PDCPT5 and 6 were conducted within the tension zone, where there were many soil blocks, which were dragged and rafted together into the failure area (compression zone) (Fig. 2.14b and c). PDCPT7 was conducted where the flowslide was believed to have started (Fig. 2.14d). PDCPT8 was conducted few meters away from the red building (Fig. 2.14e) which miraculously remained in its original position defying the ground movement. during the flowslide and did not experience displacement unlike other structures in the flowslide zone. Although, some structural damages had occurred which made the building uninhabitable. This was attributed to the massive raft foundation of the structure, which is elaborated in detail by Kiyota et. al. (2020).

The N values obtained from all the PDCPTs for depth less than 5 meters ranged between 5 - 10, which represent very loose to loose soil (Teng, 1962). The N values obtained here correspond to the critical Ncr values for potentially liquefiable within this range of depth (Koizumi, 1966). This is believed to be a loosely deposited sand and silty sand layers which were transported from upstream of flowslide region. However, by comparing the results of PDCPT 4, 5, 6 and 7 with PDCPT 8, it could be ascertained that, the N-values in PDCPT 8 are greater than 10 beyond the depth of 3.5 m. PDCPT 8 which was conducted close the red house has higher N-values. A trend similar to PDCPT 8 was observed in the tests conducted by Kiyota et. al. (2020) in the same vicinity. While in PDCPT 5 an out of trend peak could be seen, which could be attributed to presence of gravelly layer at 2.5 m, which are assumed to be liquefied. While, liquefaction of gravelly soils are rare as per historical records, some cases of liquefaction in gravelly soils were observed in past earthquakes such as during the 1995 Hyogoken Nambu earthquake, Japan as well as during the 1983 Borah Peak earthquake in USA, in which extensive liquefaction took place in fluvial sandy gravel layers (Kokusho, 2003).

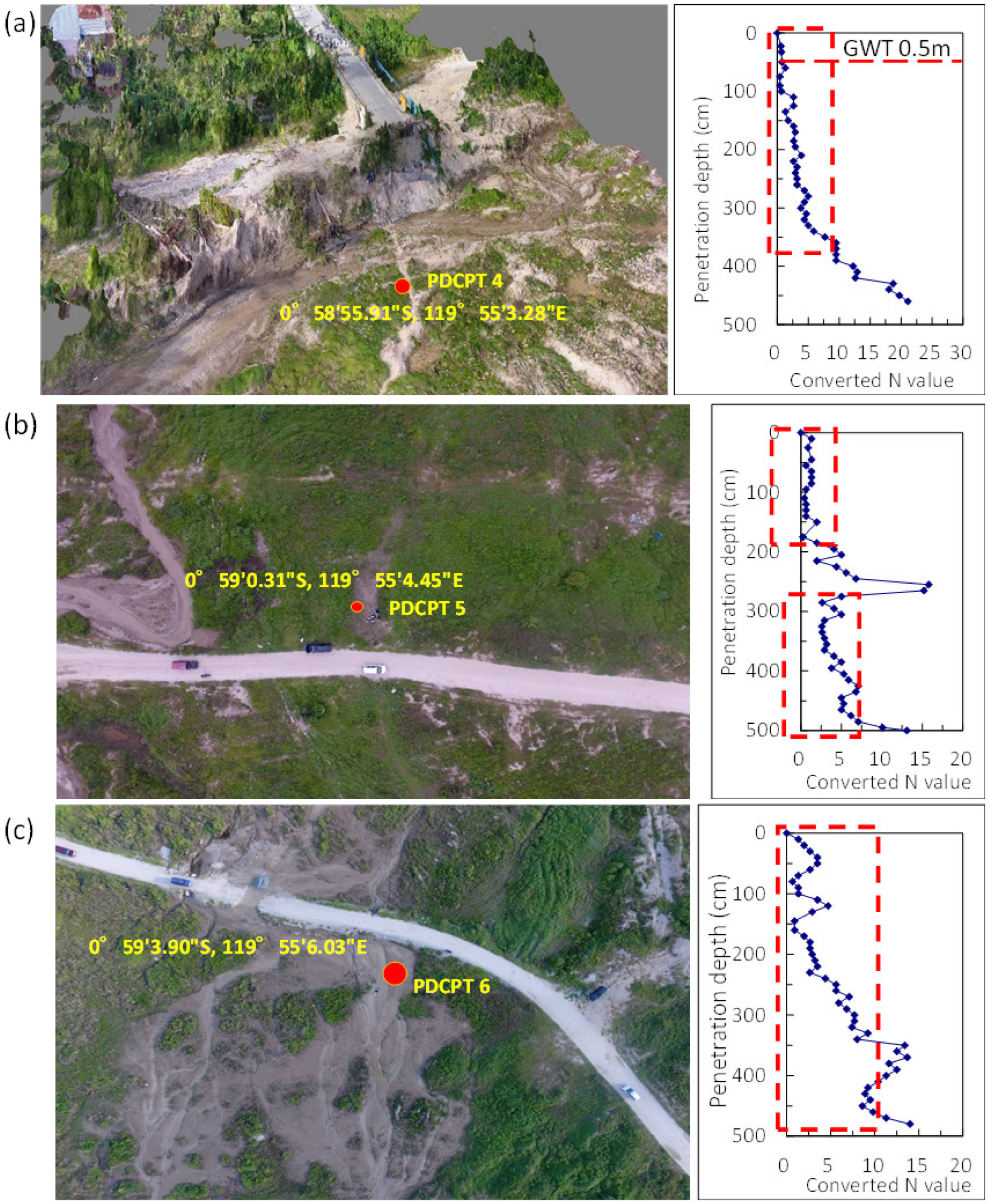

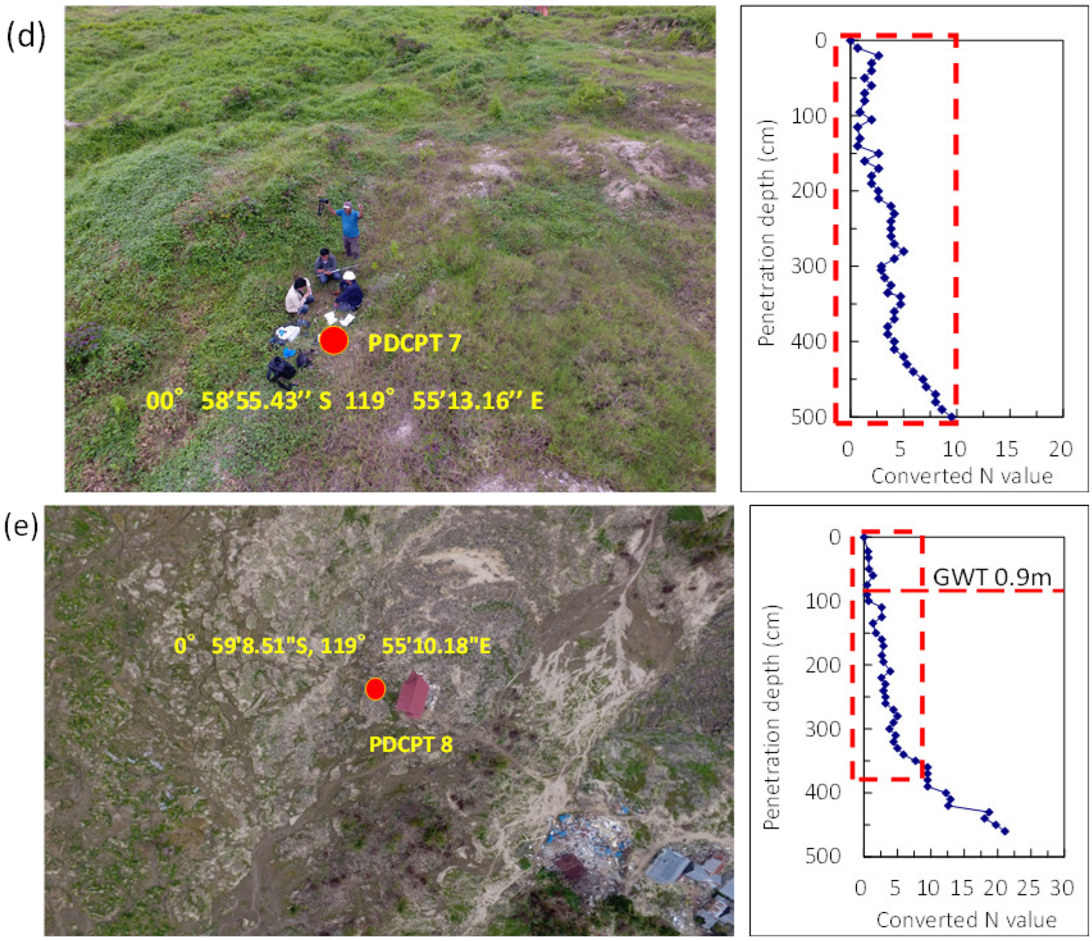

Figure 2.14 Drone imagery of locations of PDCPT and N_{SPT} versus depth values (a) PDCPT4 (b) PDCPT5 (c) PDCPT6 (d) PDCPT7 and (e) PDCPT 8.

2.5.2 Gradation of soil samples

Soil samples were collected from locations near the PDCPT tests in the failure zone as already shown in Fig. 2.9 were tested to determine the grain size distribution. Grain size distribution curves of soil samples S1, S3 and S5 are shown in Fig. 2.15. These soil samples can be classified as silt with low plasticity (ML) as per Japanese Geotechnical Society Standards (JGS 0051-2009). These soils were either carried away by the flow slide or by the succeeding mudflow or deposited as residual soils. As published in the handbook of Port and Harbor Research Institute of Japan (PHRI, 1997) the gradation of these soil samples can be classified as potentially liquefiable.

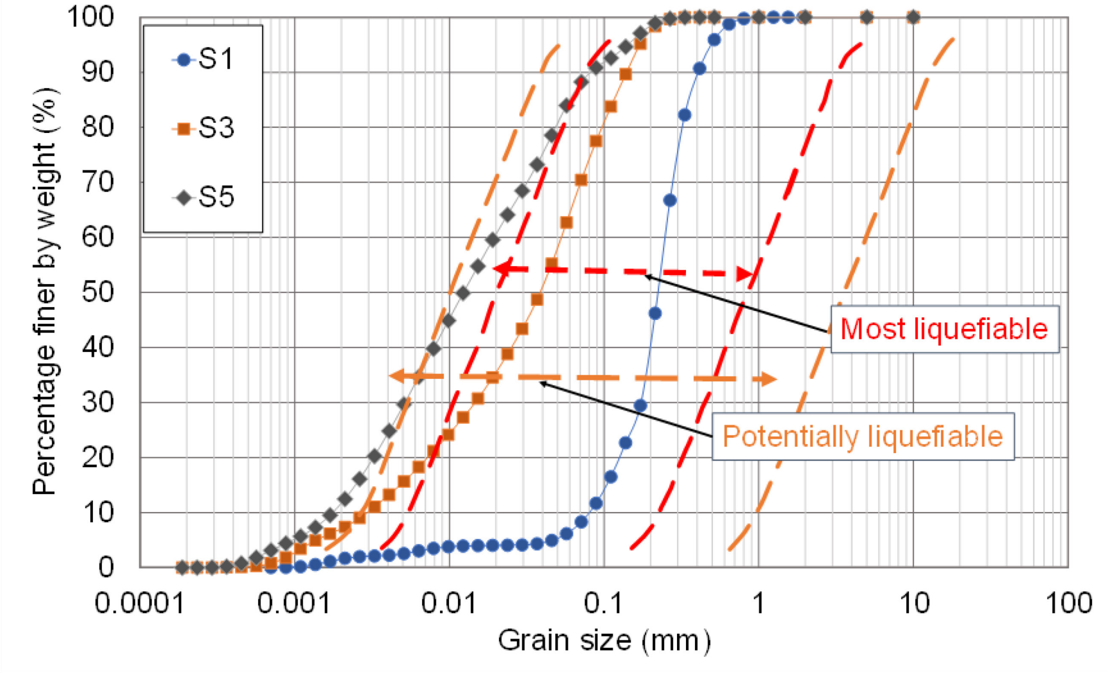

Figure 2.15 Gradation of soil samples S1, S3 and S5 collected from the field.

2.6 FLOWSLIDE AT SIBALAYA

Sibalaya site was located much far from the other three flowslide locations and was sparsely populated. Most of the residential structures which got destroyed were located near the main road passing through the village. The flowslide engulfed an area of about 0.529 km^2 and destroyed around 125 housing units. As similar to Jono Oge, this site was also on a relatively level ground with the slope grade from 2 – 6 % (Gallant et al., 2020). Our team conducted aerial survey of the site and in-situ PDCPT tests as well as disturbed and un-disturbed soil sampling from the trenches dug out at the site during our survey. The observations of soil profile from the trenches, PDCPT results and classification of soil from disturbed samples are discussed here.

An orthomosaic image of the site was created from the drone survey to identify key geologic features, terrain, and damage to the site (Figure 2.16). Here, excessive scouring and erosion near the head scarp is observed, which was not seen in Jono Oge where complete displacement of ground in large soil block occurred. The scouring had occurred from both the flanks and the middle portion of the head scarp seemed partly intact; this implies to a slightly different mechanism of the flowslide as compared to other sites. Most of the houses which were located near the road, were destroyed by the flowslide and washed away with the mud flow caused by the canal breach which discharged an enormous quantity of water towards the residential areas. Also, a large section of the road was displaced around 350 m towards the downstream side as shown in Figure 2.16. Here too, the tensile cracks can be seen on the either side of the revamped road.

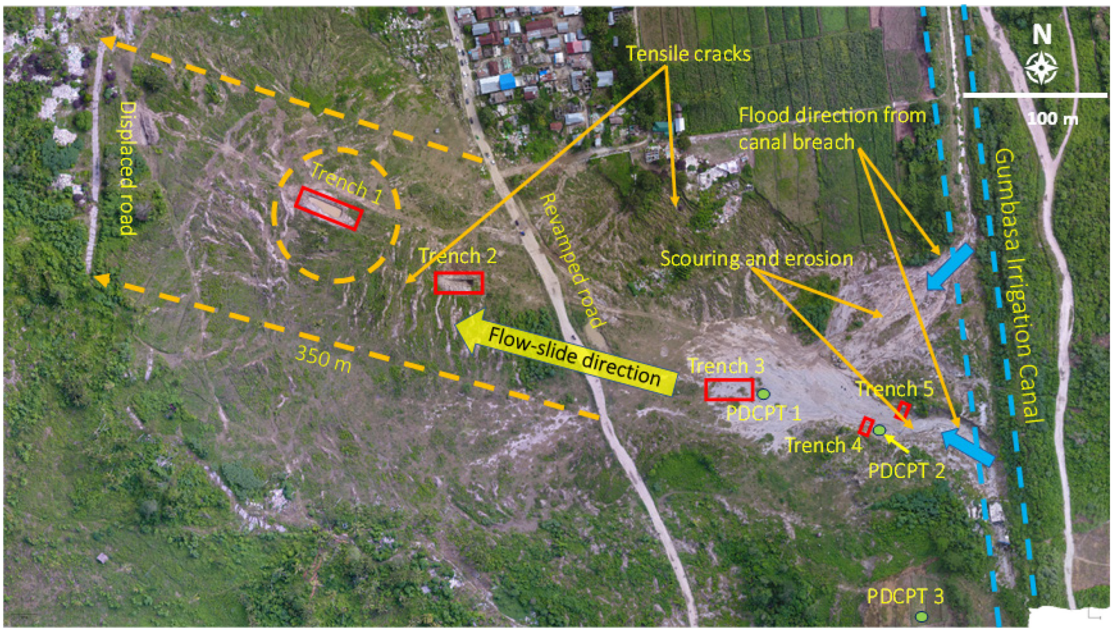

Figure 2.16 Orthomosaic image of Sibalaya flow-slide site with identification of key features and trench locations (Surveyed on July 1, 2019).

The change in elevation profile of the Sibalaya site was evaluated by generating the raster images from the contour data of pre- and post-earthquake condition in a similar way to Jono Oge. The raster image with the elevation profile before the earthquake is shown in Figure 2.17 a while, Figure 12.17 b represents the terrain after the earthquake. As observed from Figure 2.17 b, the scouring due to the canal breach can be clearly observed through low elevation of the location. While the ground elevation contours were smoother before the earthquake, the post-earthquake contours show an uneven surface due to the undulation resulted from the elevation depreciation and heaving of ground caused by the flowslide. The intact cliff walls behind the Trench 4 and 5 are also identifiable from the elevation profile.

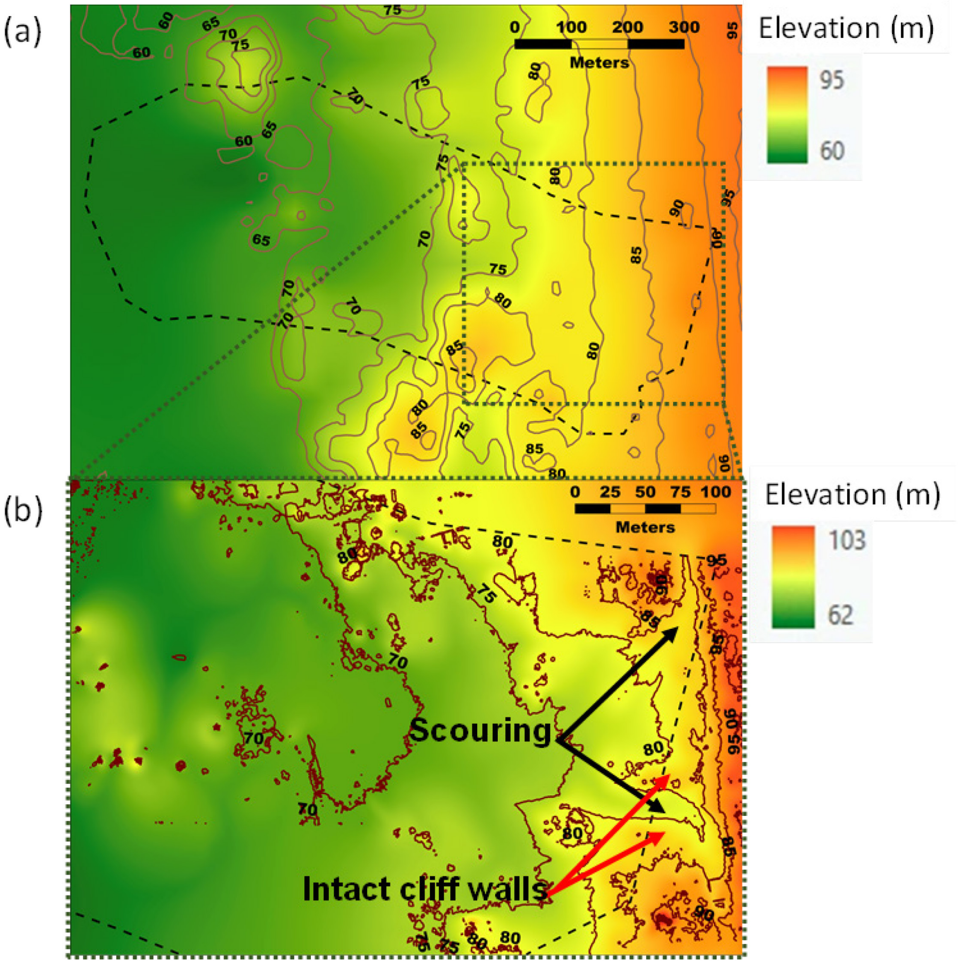

Figure 2.17 Raster elevation profile of the Sibalaya flow-slide site: (a) before earthquake and (b) after the earthquake (Surveyed on June 29, 2019).

Furthermore, to evaluate the lithology of the sub-surface soil, visual inspection of the excavated trenches was undertaken at the site. The detailed soil stratification of the site at different locations and flowslide direction is discussed as follows:

Trench 1

Trench 1 was excavated on the left side of the road passing through the Sibalaya site (see Figure 2.16). An image of the soil lithology from the right wall of the Trench 1 is shown in Figure 2.18 a. The trench was excavated in a sloped manner with the deeper side towards the upstream direction of the flowslide, the deepest part of the trench was more than 3.6 m in height. The soil profile here seemed highly stratified with layers of coarse (gravely sand) and fine (silty sand and sandy, clayey silt) soil. The right wall is divided into two pictures in Figure 2.18 a, the one on the left, which is in the deeper section of trench shows no such stratification while the other on the right shows clear stratification. Also, it is important to note the sand ejecting towards the surface, most probably after the flowslide occurred and the overburden soil was displaced. Furthermore, a converging soil boundary were observed, with gravely sand layer subducting below the clayey sand layer. This could have been due to the forward thrust provided by the slide due to which the clayey soil might have tried to bend the stratified soil layers seen in the right picture. The left wall also had a similar soil stratification while the front wall seemed to be of mostly of sandy layer. Figure 2.18a also shows the sampling locations of the disturbed soil samples (S1~S5). The grain size distribution curves of these samples are shown in Figure 2.18 b and the fines content of the samples given in Table 2.2. Here samples S3 and S5 which seems to have higher fines content as well as look sticky from the surface have higher fines content and lies under the range of most liquefiable soil type, while sample S1 lies partially in the most liquifiable to potentially liquefiable and samples S2 and S4 come under the category of potentially liquefiable soil type. The soil gradation is in confirmation with the visual observation at the site.

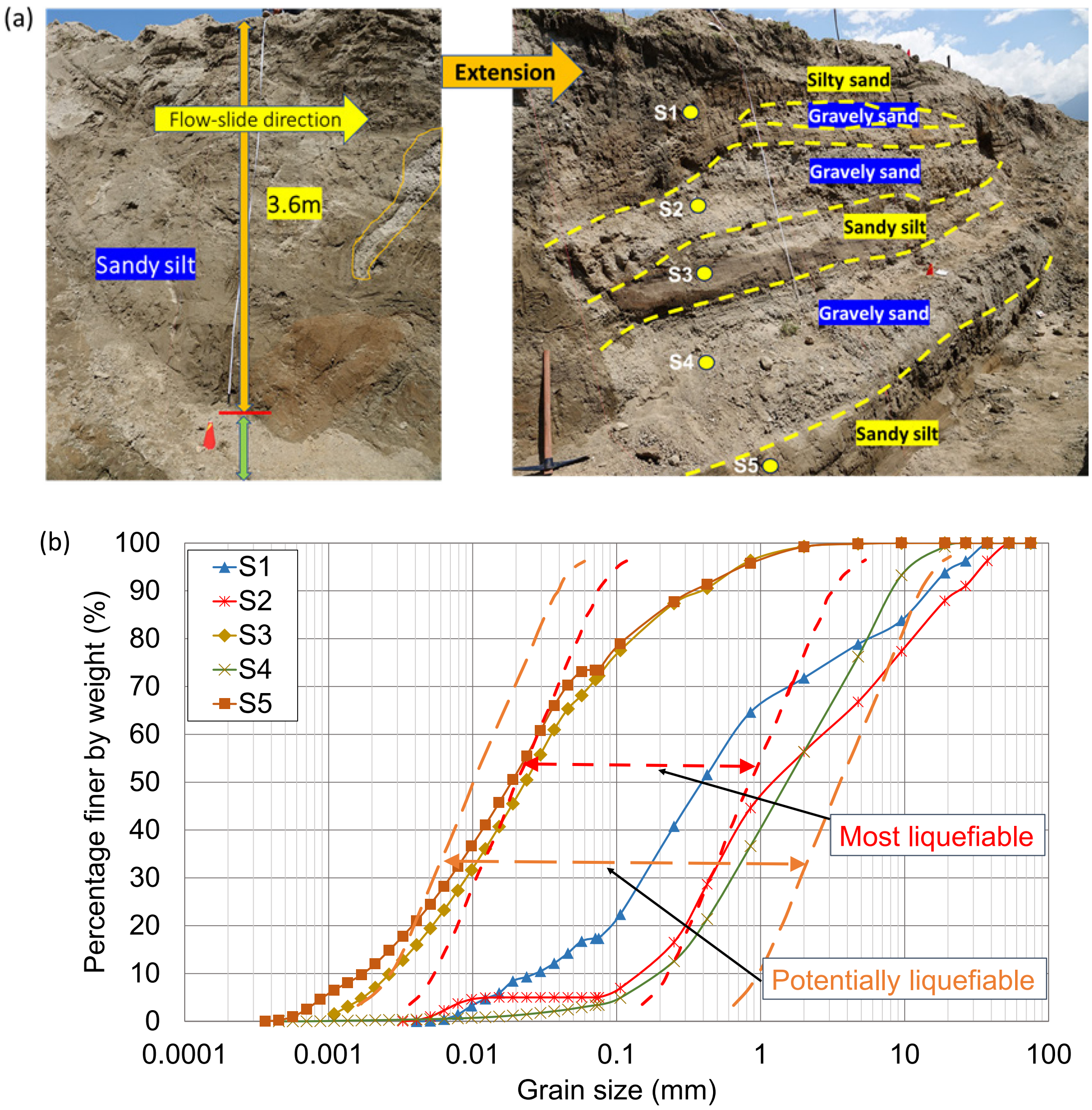

Figure 2.18 Trench 1 in Sibalaya flow-slide site: a) soil lithology from the right wall with sampling locations for disturbed soil samples S1 ~ S5 and (b) grain size distribution of the samples S1~S5.

Table 2.2 Fines content for samples S1~S5 at Trench 1 in Sibalaya.

	S1	**S2**	**S3**	**S4**	**S5**
Gravel (>2mm)	28.2	43.6	0.8	43.7	0.8
Sand (2mm～75μm)	61.5	61.8	27.6	72.8	26.4
Silt (75μm～5μm)	17.3	4.0	52.8	3.0	49.0
Clay (<5μm)	0.1	1.0	19.4	0.5	24.4
C_u	25.0	11.33	13.46	11.50	16.57
C_c	1.33	0.79	0.89	0.86	0.97
Fines content (%)	17.4	5.0	72.2	3.4	73.4

Trench 2

Trench 2 was located near Trench 1 and was in a similar orientation. The soil profile of the left wall of the trench is shown in Figure 2.19. This trench also had the identical soil stratification as Trench 1 although the synclinic orientation of the shallower soil strata is unique, which was not observed in the Trench 1. This feature might have been resulted from the forward push applied from the soil blocks moving towards the downstream section during the flowslide and the resistance provided from the soil layers in the compression zone.

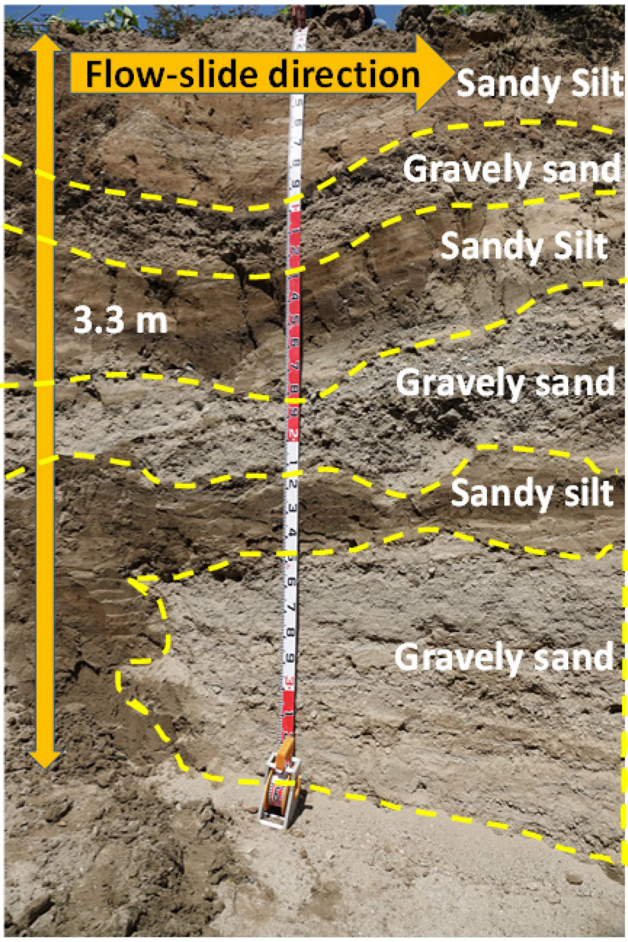

Figure 2.19 Soil lithology from the right wall of Trench 2 (Image shot on June 28, 2019).

Trench 3

Trench 3 was located in the central section of the flowslide with the deeper side towards the upstream of the flowslide. Figure 2.20 a shows the soil profile of the left wall of Trench 3, with much thicker overlying sandy silt layer. The top layer mainly consisted of the soil transported from the upstream areas of the flowslide, also some debris of plant roots and plastic bags were seen sandwiched in the soil. The surface of the soil layers in this profile was very soft and damp. This was confirmed by the PDCPT 1 conducted next to this trench, and shown in Figure 2.20 b. The PDCPT 1 values ranged around 5 for sandy silt, silty clay, clay layers, these soil layers could be classified as very loose soil (USACE, 1994).

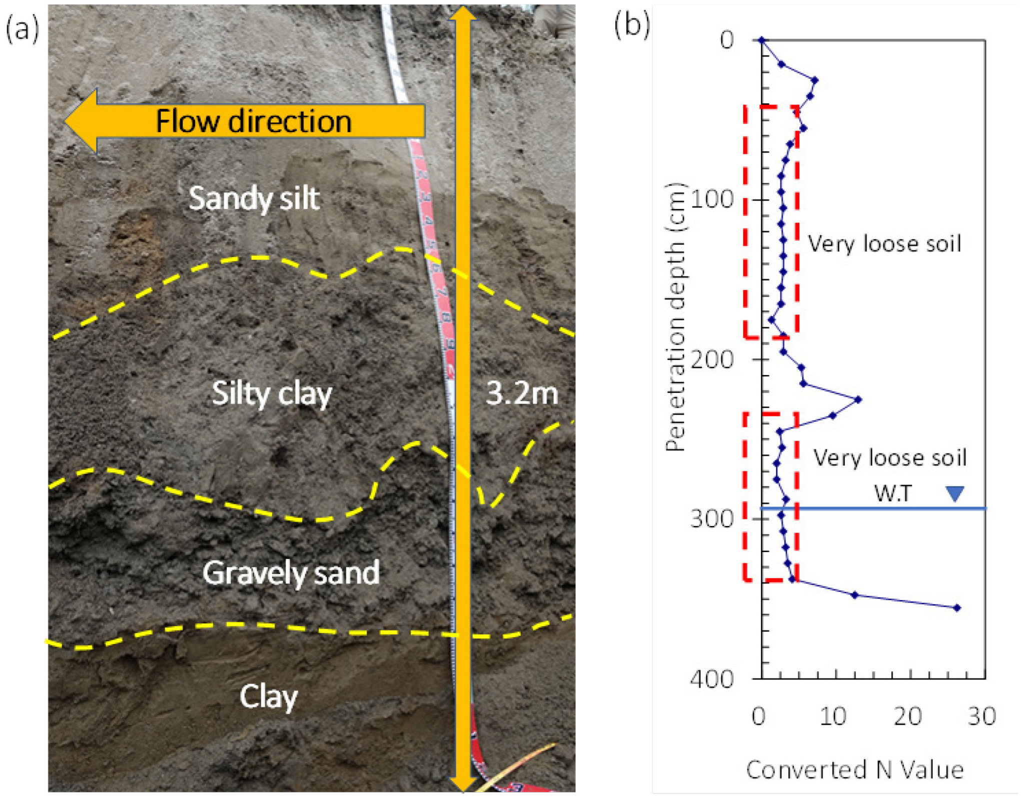

Figure 2.20 Trench 3: (a) Soil lithology from the left wall of Trench 3 (Images taken on June 30, 2019) and (b) NSPT versus depth values for PDCPT 1.

Also, these N values are in coherence with the critical Ncr values for soils categorized as potentially liquefiable at this range of depths (Koizumi, 1966). Furthermore, the N increased up to 15 for the gravely sand layer, which then again drops down for the clay layer and then rises at higher depth below the clay layer confirming a hard stratum at the bottom.

Trench 4 and 5

The trench 4 and 5 were excavated closer towards the location of the crown. The length of the trenches was oriented perpendicular to the flow direction of the ground. Here, Figure 2.21a shows the vertical soil profile of face wall of Trench 4, while Figure 2.21b depicts the N value versus depth profile of the PDCPT 2 conducted just next to the trench. Here the surface soil mainly consists of the gravelly sand with small rocks and boulders as seen in Figure 2.21a, while the underlying layers of sandy and clayey silt, coarse sand with gravel and sandy silt, each layer stacked over the other subsequently. The PDCPT 2, which was conducted next to Trench 4, confirmed the presence of very loose sand till 1.5 m after which it gained sudden strength and the cone would not go any further even after 40 blows. This could have been due to presence of dense gravel as also seen from the profile the sandy gravel layer at that depth. A PDCPT sounding was also conducted in the un-failed area in the fields behind the Trench 4, with ground elevation 6m above the location of PDCPT 2. The location of this PDCPT 3 is given in Figure 15 and the N value versus depth profile is given in Figure 2.21 c.

Trench 5 was excavated on the opposite side of Trench 4, with the flowslide direction perpendicular to the length of the trench as shown in Figure 2.22. The facing wall of Trench 5 has thin seams of fine silt at higher elevation or can be said at shallow depths prior to failure. The soil stratification of this trench was mainly composed of gravely and sandy soil with presence of multiple gravel layers in between sandy clay layers. Also, the surface soil at this trench had predominantly gravely soil, with cobbles and stones. The presence of more coarser soil layers in this stratum could be one of the main reasons it stayed intact during the flowslide. Furthermore, the holes seen on the wall of the trench, were the nests of the Rainbow bee-eater bird, which typically makes its nests in loose gravely and sandy soil. This also confirms the looseness of the soil layers in the site. Although, the vertical walls of Trench 4 and 5 did not fail during the flowslides due to presence of predominant gravely sand at shallow depth, they could have become soft after being exposed to rain post flowslide so that the birds could dig in the loose gravely soil.

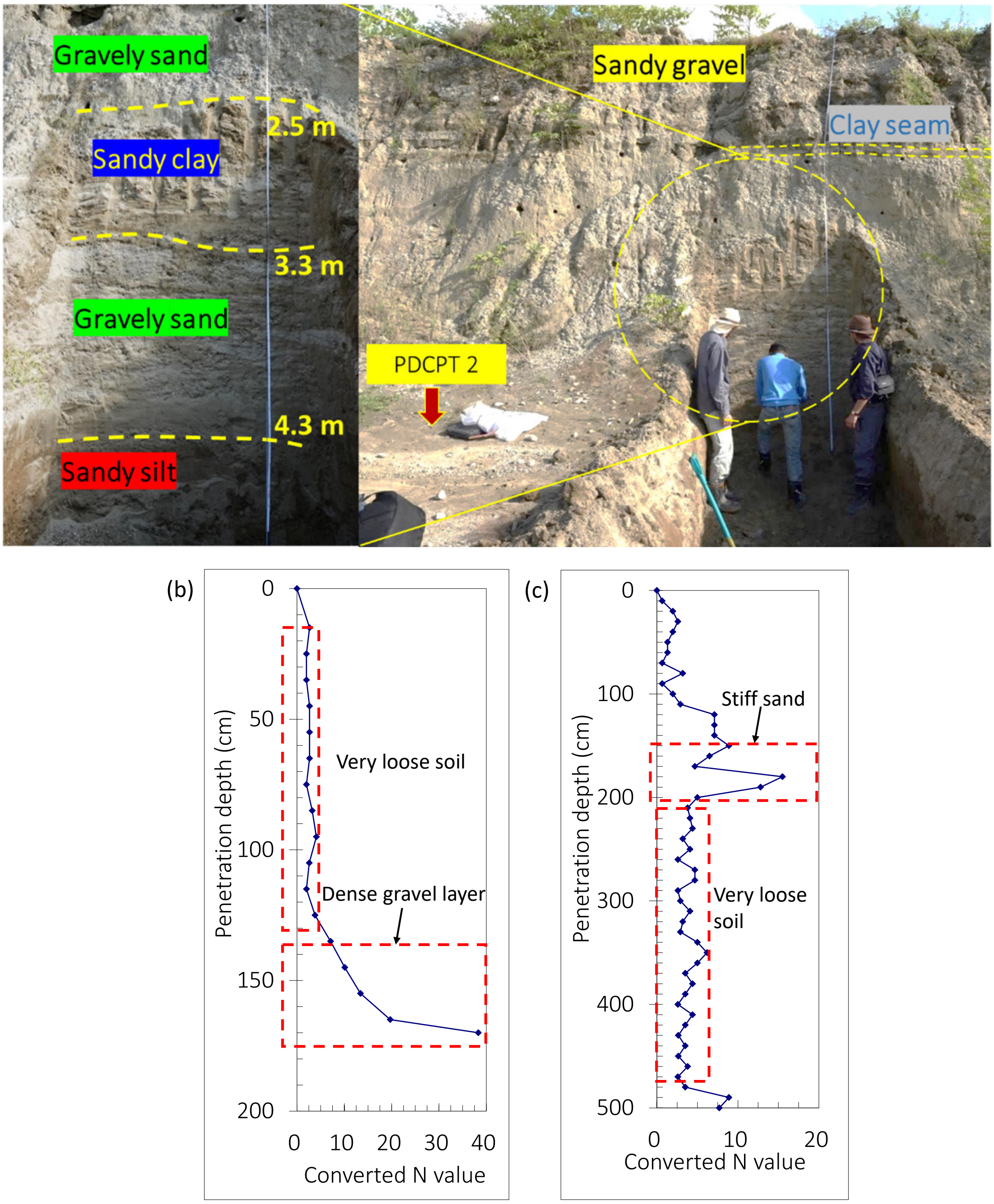

Figure 2.21 Trench 4: (a) Soil lithology of Trench 4, and NSPT versus depth profile for (b) PDCPT 2 and (c) PDCPT 3.

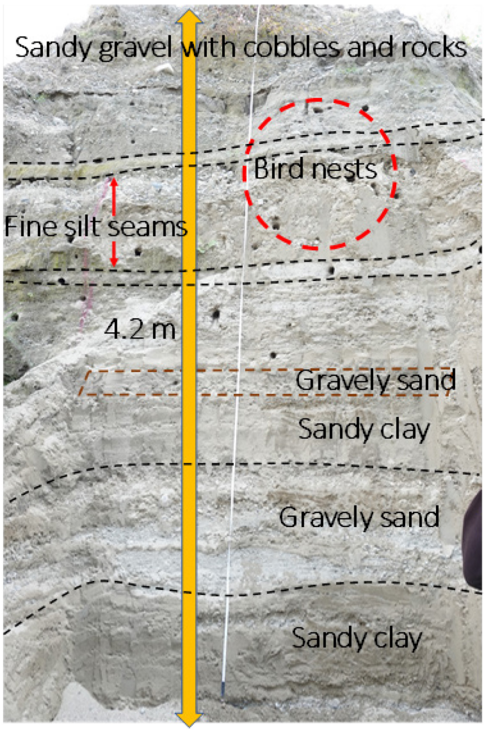

Figure 2.22 Soil lithology of Trench 5 with stratified interlayer seams (Image taken on June 29, 2019).

2.7 CONCLUSIONS

This chapter provides an insight into the outcomes of the forensic geotechnical survey conducted aftermath the 2018 Sulawesi earthquake. Detailed in-situ field investigation was performed in two phases during October-November 2018 and June-July 2019. The first phase involved disturbed and undisturbed sampling, PDCPT sounding and aerial reconnaissance, while the second phase involved detailed geological and geotechnical investigation through trenching. Key factors which might have contributed to the triggering of flowslide were identified and evaluated. The findings of the survey from all the locations according to site accessibility and available time are presented. Based on the perishable data and information accumulated during the survey, the following conclusions could be made:

- The presence of shallow water table along with presence of sub-surface artisan aquifer made the ground water to be under high hydraulic gradient. Also, the breach in water canal further aggravated the damage by triggering mudflow.

- The soil strata were highly stratified along with sharp change in particle size types causing contrasting permeability characteristics vertically which influences the transmitting velocity of the pore water within the layers, thereby affecting the residual strength of the soil after the liquefaction.
- In Jono Oge, the soil strata outside the flowslide area was found to be comparably firm and non-liquefiable.
- Through the trench surveys in Sibalaya, it was found that, the multiple cap layers were present across the flowslide site. Although, the properties and particle size of the cap layers varied from trench to trench.
- The presence of liquefiable deposit along with the presence of multiple capping layers might have contributed to triggering the flowslides.

The findings from this chapter are published in,

Hazarika, H., Rohit, D., Pasha, S. M. K., Maeda, T., Masyhur, I., Arsyad, A., & Nurdin, S. (2021). Large distance flow-slide at Jono-Oge due to the 2018 Sulawesi Earthquake, Indonesia. *Soils and Foundations*, 61(1), 239–255.

REFERENCES

Bradley, K., Mallick, R., Andikagumi, H., Hubbard, J., Meilianda, E., Switzer, A., Du, N., Brocard, G., Alfian, D., Benazir, B., Feng, G., Yun, S. H., Majewski, J., Wei, S., & Hill, E. M. (2019). Earthquake-triggered 2018 Palu Valley landslides enabled by wet rice cultivation. *Nature Geoscience*, *12*(11), 935–939. https://doi.org/10.1038/s41561-019-0444-1

Gallant, A. P., Montgomery, J., Mason, H. B., Hutabarat, D., Reed, A. N., Wartman, J., Irsyam, M., Simatupang, P. T., Alatas, I. M., Prakoso, W. A., Djarwadi, D., Hanifa, R., Rahardjo, P., Faizal, L., Harnanto, D. S., Kawanda, A., Himawan, A., & Yasin, W. (2020). The Sibalaya flowslide initiated by the 28 September 2018 MW 7.5 Palu-Donggala, Indonesia earthquake. *Landslides*, *17*(8), 1925–1934.

Global Change Master Directory (GCMD). (2020). *GCMD Keywords, Version 9.1.5. Greenbelt, 473 MD: Earth Science Data and Information System, Earth Science Projects Division, 474 Goddard Space Flight Center (GSFC) National Aeronautics and Space Administration 475 (NASA).* https://earthdata.nasa.gov/gcmd-forum

Hazarika, H., Rohit, D., Pasha, S. M. K., Maeda, T., Masyhur, I., Arsyad, A., & Nurdin, S. (2021). Large distance flow-slide at Jono-Oge due to the 2018 Sulawesi Earthquake, Indonesia. *Soils and Foundations*, *61*(1), 239–255.

Japanese Geotechnical Society Standard. (2016). *Method for portable dynamic conepenetration test (JGS 1433-2012)*.

Japan International Cooperation Agency (JICA) (2019). *Report of the technical committee on the 2018 Sulawesi earthquake, Indonesia*.

Kiyota, T., Furuichi, H., Hidayat, R. F., Tada, N., & Nawir, H. (2020). Overview of long-distance flow-slide caused by the 2018 Sulawesi earthquake, Indonesia. *Soils and Foundations*, *60*(3), 722–735.

Koizumi, Y. (1966). Changes in density of sand subsoil caused by the niigata earthquake. *Soils and Foundations*, *6*(2), 38–44.

Kokusho, T. (2003). Current state of research on flow failure considering void redistribution in liquefied deposits. *Soil Dynamics and Earthquake Engineering*, *23*(7), 585–603.

Kusumawardani, R., Chang, M., Upomo, T. C., Huang, R., Fansuri, M. H., & Prayitno, G. A. (2021). Understanding of Petobo liquefaction flowslide based on site reconnaissance. *Landslides*. https://doi.org/https://doi.org/10.1007/s10346-021-01700-x

Mason, H. B., Montgomery, J., Gallant, A. P., Hutabarat, D., Reed, A. N., Wartman, J., Irsyam, M., Simatupang, P. T., Alatas, I. M., Prakoso, W. A., Djarwadi, D., Hanifa, R., Rahardjo, P., Faizal, L., Harnanto, D. S., Kawanda, A., Himawan, A., & Yasin, W. (2021). East Palu Valley flowslides induced by the 2018 MW 7.5 Palu-Donggala earthquake. *Geomorphology*, *373*. https://doi.org/10.1016/j.geomorph.2020.107482

Okamura, M., Ono, K., Arsyad, A., Minaka, U. S., & Nurdin, S. (2020). Large-scale flowslide in Sibalaya caused by the 2018 Sulawesi earthquake. *Soils and Foundations*, *60*(4), 1050–1063.

Takase, A., & Sasada, M. (2013). The application of portable dynamic cone penetration test to the geo-disaster reconnaissance (in Japanese). *Japan Geotechnical Consultants Association Technical Forum*, 64–65.

Teng, W. C. (1962). *Foundation Design*. Prentice Hall.

Watkinson, I. M., & Hall, R. (2019). Impact of communal irrigation on the 2018 Palu earthquake-triggered landslides. *Nature Geoscience*, *12*(11), 940–945.

CHAPTER 3

2D MODELS SUBJECTED TO DYNAMIC LOADING

3.1 INTRODUCTION

Liquefaction induced flow failure or lateral spreading has been a major cause of damage during earthquakes. Such failures may or may not take place during the shaking but often trigger after the cease of the ground motion as seen during the 2018 Sulawesi earthquake, where the flowslides initiated after a couple of minutes of the cease of ground motion (Hazarika et al., 2021). In past, flow failures at delayed duration were observed in the Hakusan District during the 1964 Niigata earthquake where a large area slide with a displacement of few meters and the sliding continued even after the earthquake stopped (Kokusho, 2000). During the 1971 San Fernando earthquake, the Lower San Fernando Dam, observed liquefaction induced flow failure half a minute after the earthquake ceased to happen (Seed, 1987). Furthermore, during the 1987 Edgecumbe earthquake in New Zealand, a bridge became unserviceable due to the lateral spreading of foundation soil around one hour after the end of ground motion (Berrill et al., 2001). Furthermore, in past flow failures have also known to occur in a very gently sloping ground, mainly in a sub-marine environment, for example flow failure off the California Coast during a 1980 medium magnitude earthquake. In this case, a large sub-sea area of 2 km x 20 km, slipped and levelled in elevation. It was reported that the slide surface had a pre-failure slope of 0.25° and consisted of sand and mud (Field et al., 1982). Similar to it, large scale loss of property and life was observed during a submarine flow failure in Valdez and Seward port cities in Alaska, USA. The large slip surface of more than 2km had an average slope of 5° (Coulter & Migiliaccio, 1966; Lemke, 1967).

While several mechanism views have been postulated until now on the flow mechanism in liquefied ground, one of them is the effect of void redistribution or water film formation in layered soils (Kokusho & Kabasawa, 2003), which is also one of the postulated mechanisms of the 2018 Sulawesi earthquake (JICA, 2019). The term void redistribution was initially coined by NRC (1985). This phenomenon occurs when, a loose liquefiable sand layer is sandwiched by a low-permeability silt or clay layer on either side (Figure 3.1). During an earthquake motion, the sand layer tends to approach its maximum excess pore pressure post shaking. This will cause and upward hydraulic gradient across the sand layer due to transmission of pore water from deeper sections of the layer. Due to the presence of a low permeable cap layer, the dissipation of pore water to the surface will be hindered and lead to the formation of a thin water film was water based layer underneath the cap layer. Furthermore, as the water is expulsed from the lower section of the liquefiable layer near point Q, it will consolidate and densify. While due to excess ingress of water near point P, the area will dilate and loosen, leading to reduction in localized reduction in shear strength (Kamai et al., 2008). Due to the formation of localized zone of low shear strength, localized shear strains may develop at the interface of the cap layer. The development of these shear strains may be influenced by the permeability of the cap and layer which controls the diffusion rate of the excess pore water pressure.

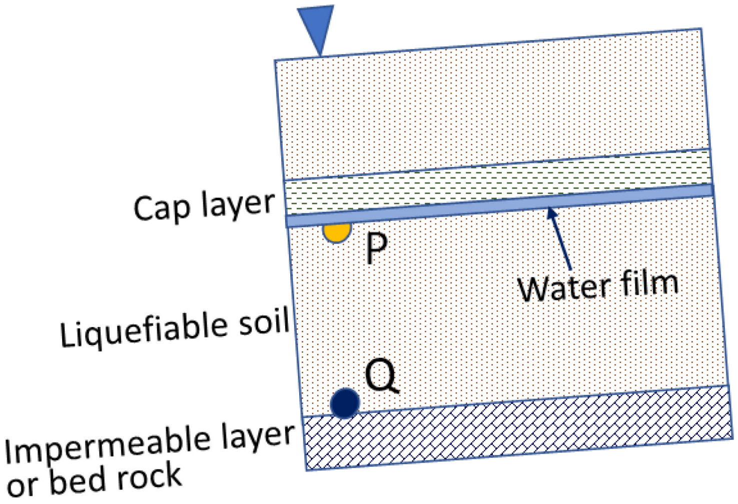

Figure 3.1 Schematic view of an infinite slope with a liquifiable layer sandwiched between cap layers (modified from Kamai et. al., 2008).

Multiple physical modelling studies (1g shake table and centrifuge tests) have depicted that the impact of void redistribution on shear strain localization in liquefiable soils are significantly influenced by factors like initial relative density (D_r), soil lithology, permeability of cap layers (k) and dynamic loading conditions (frequency content and intensity) (Kokusho, 1999; Kokusho, 2003; Maharjan & Takahashi, 2013; Malvick et al., 2006; Yang & Elgamal, 2001).

Although these studies provided the insights into the influence of cap layer on the overall soil surface deformation and dissipation of excess pore water pressure, the particle movement within the liquefiable layer and the cap layer during the failure is yet not clear. Therefore, in order to evaluate the particle movement during the sliding, 1g shaking table tests were conducted with the application of Particle Image Velocimetry (PIV), and the soil particle movement was tracked during the deformation phase. The particle movement in 2D soil models with and without the cap layers were compared and a generalised particle movement trend was developed.

3.2 PARTICLE IMAGE VELOCIMETRY

Once triggered, the soil deformation may occur at a quick pace and the exact particle movement and point of initiation of the flowslide may not be known. Therefore, it is necessary to use particle tracking techniques like Particle Image Velocimetry (PIV) in order to track the particle movement to evaluate the deformation of soil layers. This also helps in evaluating the zone of influence in a soil strata as overall displacement or deformation of soil may not occur. PIV technique has been widely used in past to measure the soil deformation at micro and macro scale as well as track the particle movement (Knappett et al., 2006; Lam et al., 2012; Tan et al., 2015), although, very few PIV studies have been performed on a submerged soil slope (Carey et al., 2018).

The objective this test is to track the particle movement and obtain a generalized deformation trend of the soil. In this chapter, the video recording of the tests is performed, and each individual frame is then separated to evaluate the particle movement through PIV technique. A user-friendly graphic user interface (GUI) PIV software, PIVLab V 2.53, which is based on MATLAB was used for this purpose (Thielicke & Sonntag, 2021). For the analysis, a Discrete Fourier Transform (DFT) method, based on Fast Fourier Transform (Soria, 1996) is used, which basically transforms the finite sequence of equally-spaced samples (pixels in case of images) into an equal-length sequence of equally spaced pixels.

3.3 TEST SETUP

A model test setup was prepared in a small lucite box of size 60 cm x 27 cm x 40 cm (length x width x height). The box was first filled with water to a 10cm height and then toyoura sand was deposited hydraulically in a loose state (Dr: 35-40%). The water level in the box was incrementally increased as the box was filled with sand. Kaolin was used as a cap layer in between the Toyoura sand layers. The kaolin layer was placed over the lower sand layer after making a smooth paste of it with water. The water level was kept just at the surface of the sand layer while placing the Kaolin. The water level was raised again of a height of 10 cm from the clay surface and then the sand was deposited again. The average thickness of the clay layer was kept 2 cm, as it was difficult to keep an exact uniform thickness. A vertical barrier was placed in the box in front of the sand to prevent the overall model from getting level during the shaking and it also provided the space for the top surface to slide down. The top surface to sand was kept almost level with a slope in the downstream for the sliding to occur. Horizontal lines with red dyed Toyoura sand were placed in the soil at every 5 cm vertically to record the deformation of soil layers. Figure 3.2a and b show the schematic side elevation of the model, (a) without cap layer (Case I) and (b) with cap layer (Case II), while Figure 3.3 a and b show the actual model for Case I and II respectively. Furthermore, to perform PIV analysis, K4 sand dyed with black spray paint was used as tracing particle. The sand was mixed with toyoura sand and placed on the glass facing surface towards the camera.

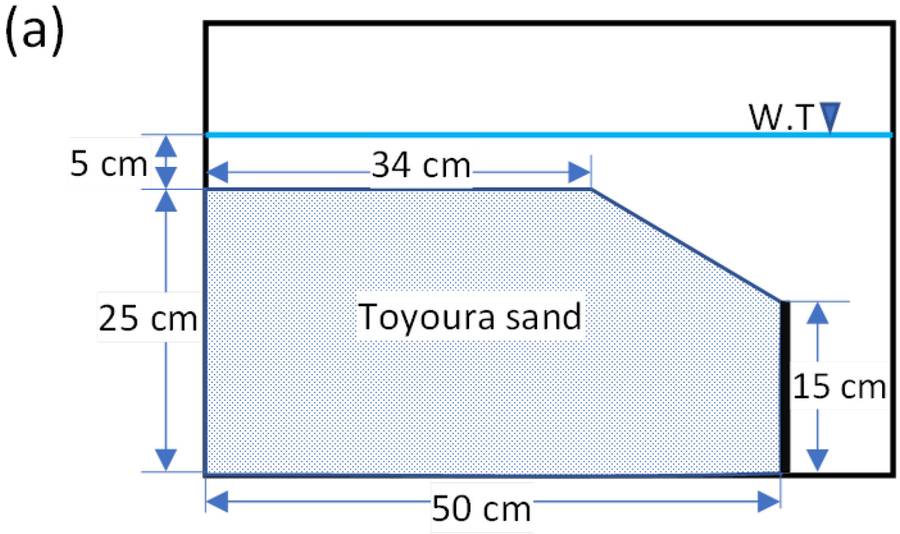

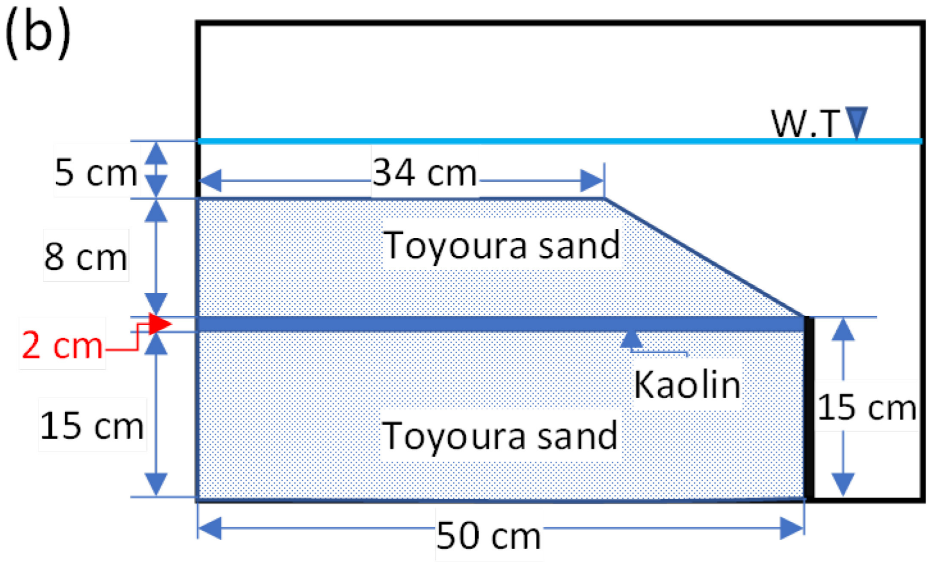

Figure 3.2 Schematic elevation of the soil model: (a) without cap layer (Case I) and (b) with cap layer (Case II).

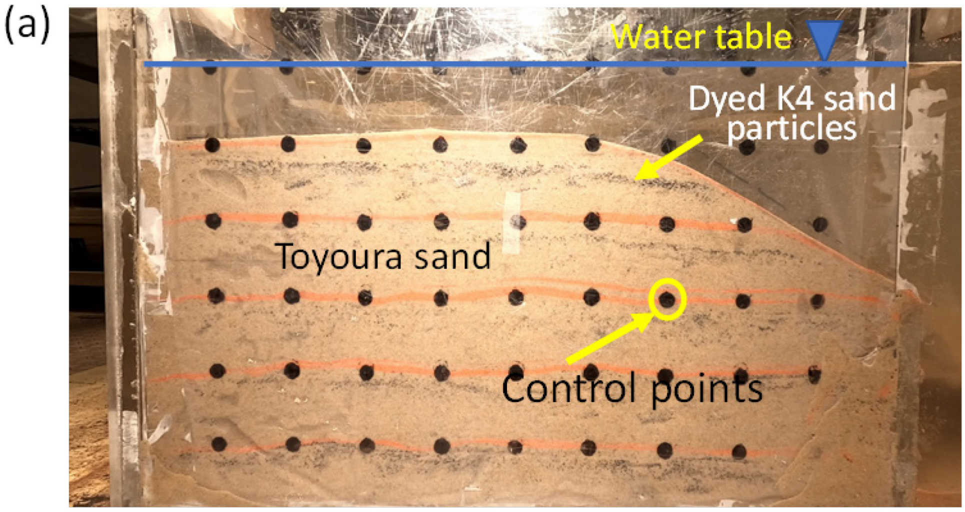

(b)

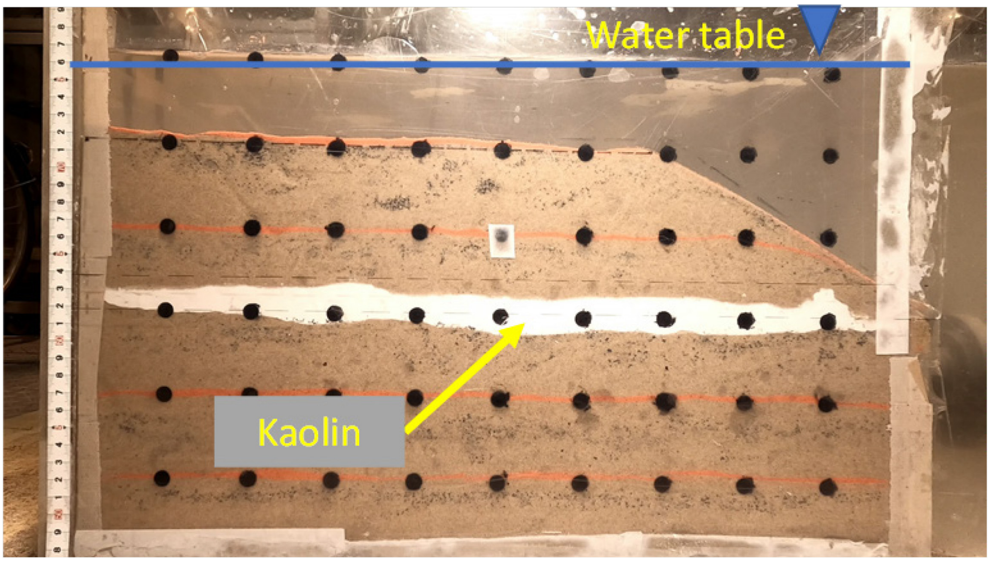

Figure 3.3 Actual side view of the soil model: (a) without kaolin layer and (b) with kaolin layer.

3.4 MODEL DESCRIPTION AND PARAMETRIC CASES

The model was oriented in such a way that the motion of the shaking table was in horizontal to the direction of soil slope. This was done to avoid the inertia during the shaking as also mention in Kokusho (1999). The model design of the small box and the barrier was inspired from Kawakita et. al., (2020). The GoPro cameras were setup and fixed on the shaking table so that their movement is relative to the soil box. The overall model setup on shaking table is shown in Figure 3.4. The properties of the toyoura sand and clay are shown in Figure 3.5a along with grain size distribution curve. An input motion of 300 Gal, with frequency 3 Hz was provided for a duration 10 secs (Figure 3.5b). The acceleration magnitude, frequency content and duration were selected after verifying the model response against various input motions and liquefaction potential at desired relative density.

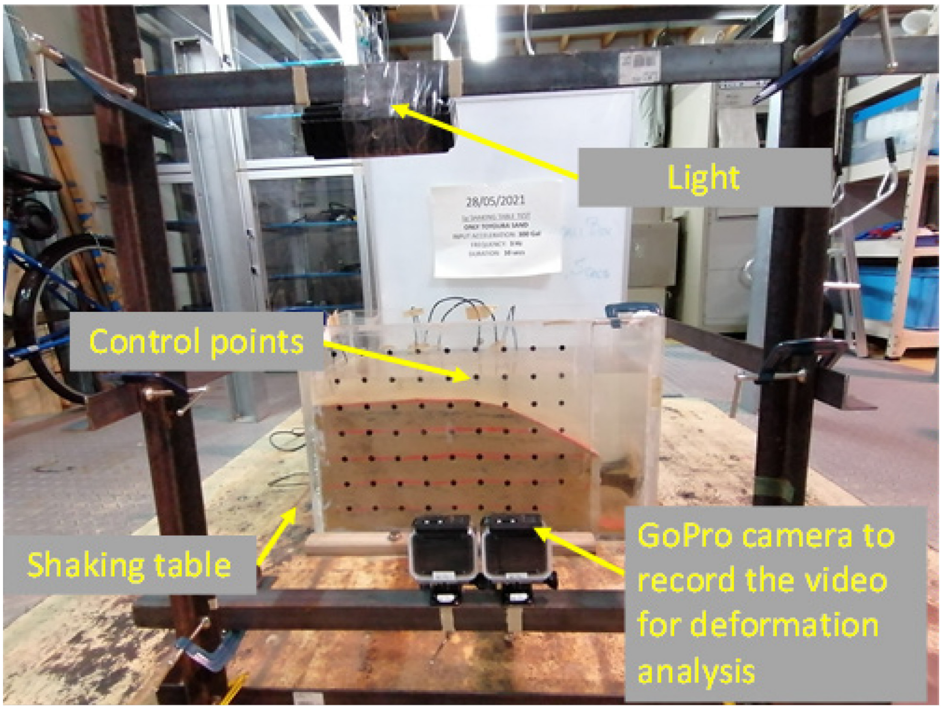

Figure 3.4 Model setup with recording instrumentation.

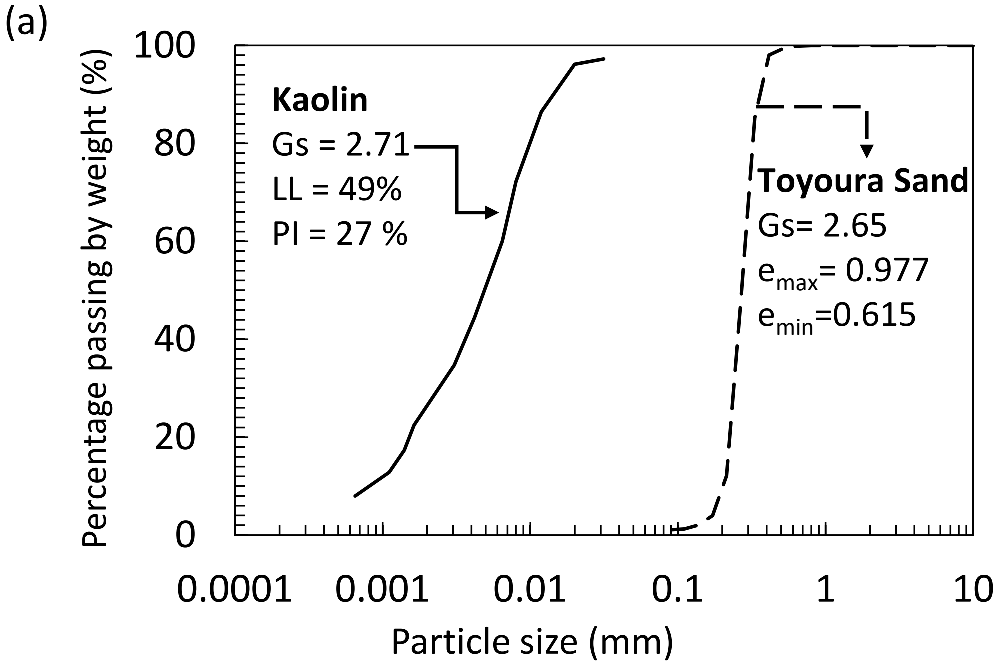

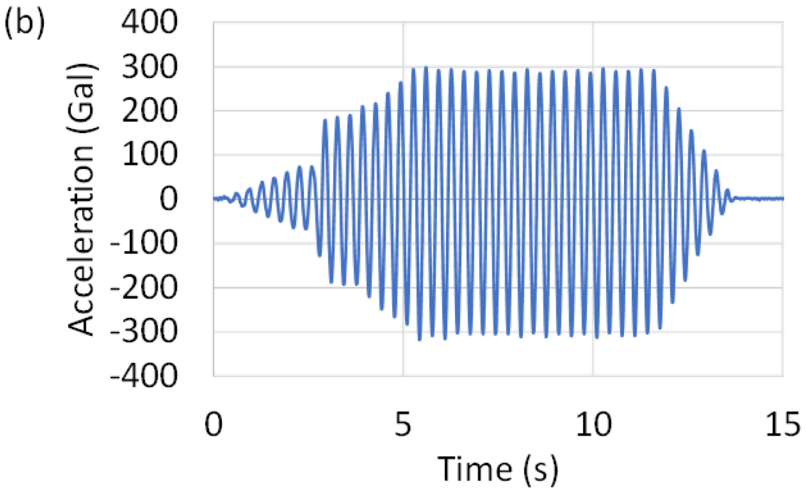

Figure 3.5 1g shaking table model characteristics: (a) soil properties and (b) input acceleration motion.

3.5 RESULTS AND DISCUSSIONS

3.5.1 Visual deformation of the soil layers

The time (t) relative deformation of the soil surface was analysed using video recordings of the tests. The recordings were divided into frames for each second and the comparison for both the cases was performed (Figure 3.6). It can be seen from the Figure 3.4 that, after 10 s of the initiation of the shaking, the soil layers had significantly settled, although the settlement in Case II was less as compared to Case I. Furthermore, after 10 s the sagging of the clay layer is initiated. At 15s the settlement for both the models is almost similar, while it is to be noted that the Kaolin layer starts mixing with the overlying and underlying sand layers and at this instant, the formation of sand boils in the Case II start. To mention, the shaking has already ceased at 10s. Furthermore, from 15 s the upward movement of the red marker lines is observed in both the cases, which is due to the upward movement of pore fluid. With time, the pounded water becomes more and more muddy due to the migration of clay particles from the boils formed on the surface. Strangely, there was no deformation of the soil layers at the deeper depth, this would have been due to the confining effect of the barrier provided in the downstream of the slope.

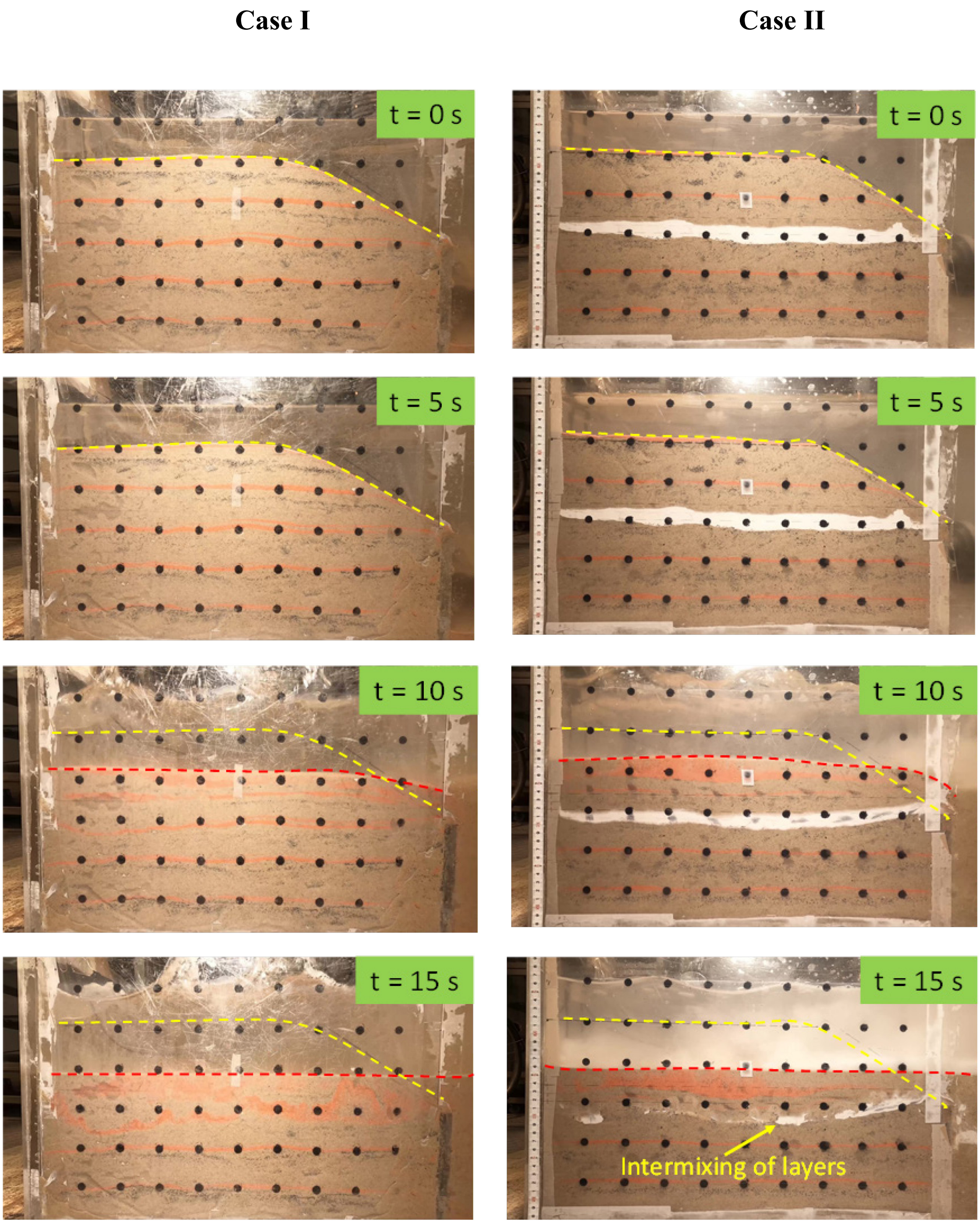

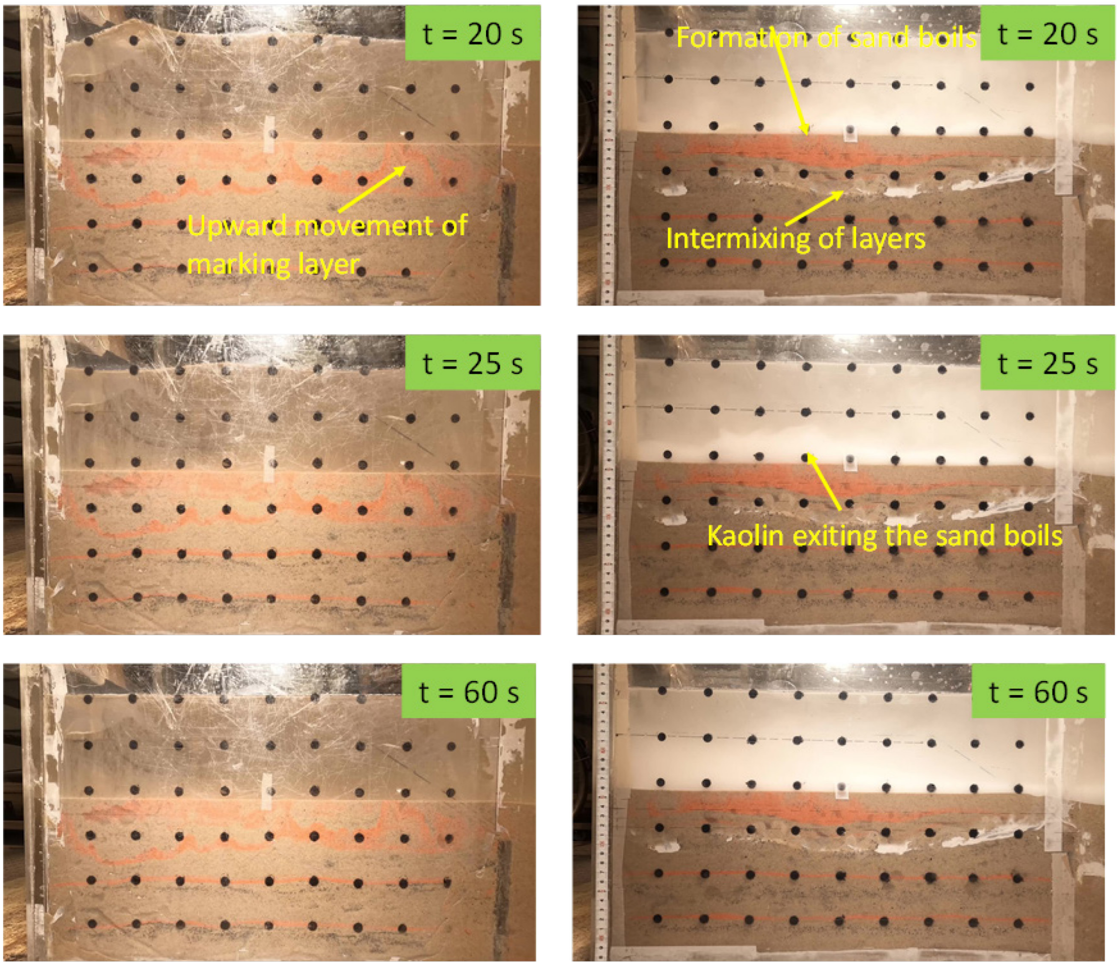

Figure 3.6 The deformation of soil surface and layers relative to elapsed time and the formation of sand boils.

3.5.2 Deformation trend based on particle vectors

To evaluate the soil deformation at micro and macro basis, particle vectors obtained from the PIV analysis are presented in Figure 3.7a~h and compared for Case I (i) and II (ii) parallelly. Each figure is presented as per the pair number and pairs 1-7 are continuously presented after which the last figure for pair 12 is shown to provide the final deformation profile. As seen from Figure 3.7c, the initiation of sliding occurs in the Case II due to cap layer at a delayed time, while in Case I, the initiation of sliding occurs from pair 1 (Figure 3.7a). The soil disturbance is observed at a higher depth due to the cap layer. Furthermore, as the topsoil settles in the upstream direction of the slope, it then pushes the clay layer vertically down thereby uplifting the downstream side of clay layer.

Case I **Case II**

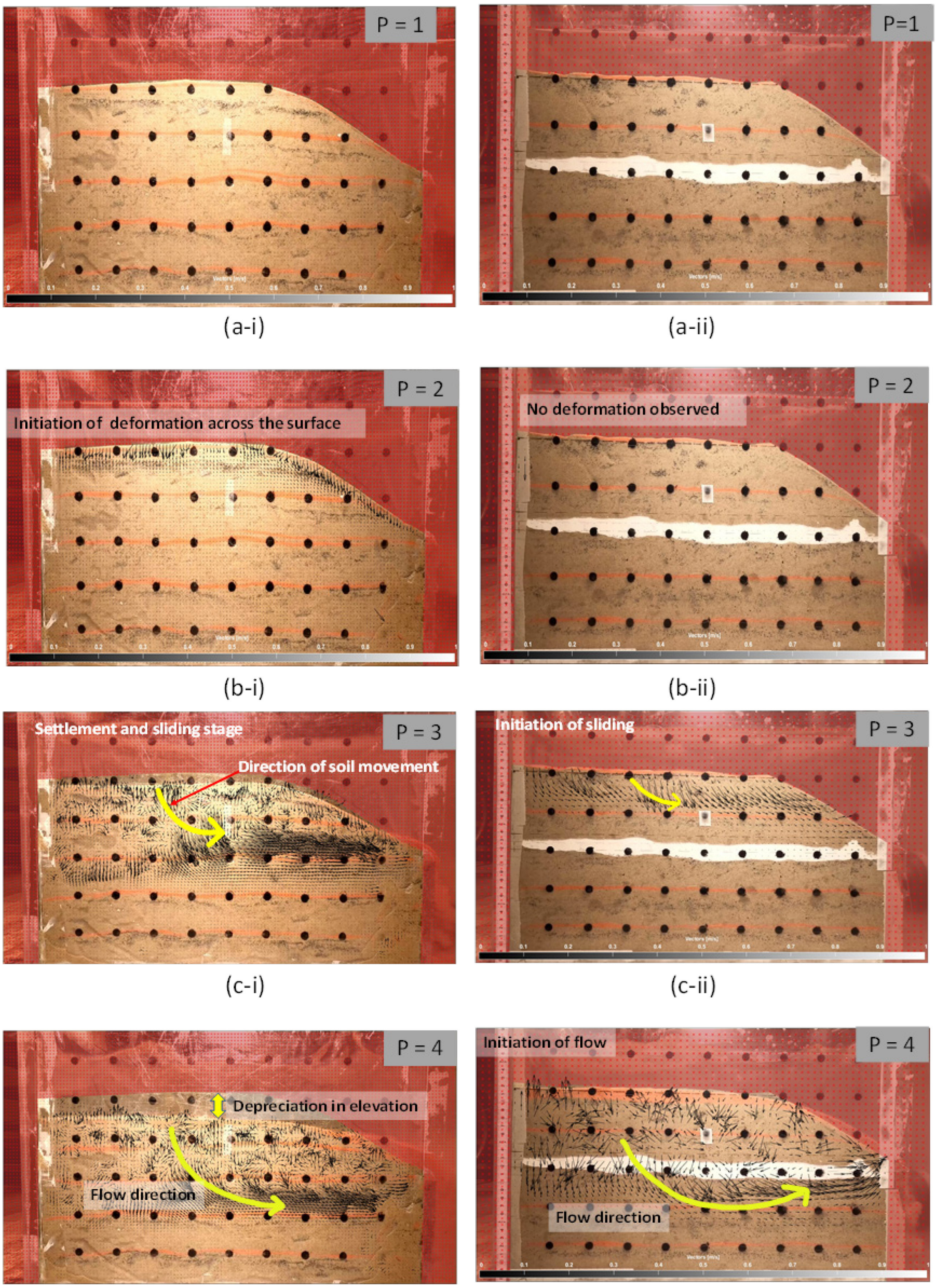

(a-i) (a-ii)

(b-i) (b-ii)

(c-i) (c-ii)

(d-i) (d-ii)

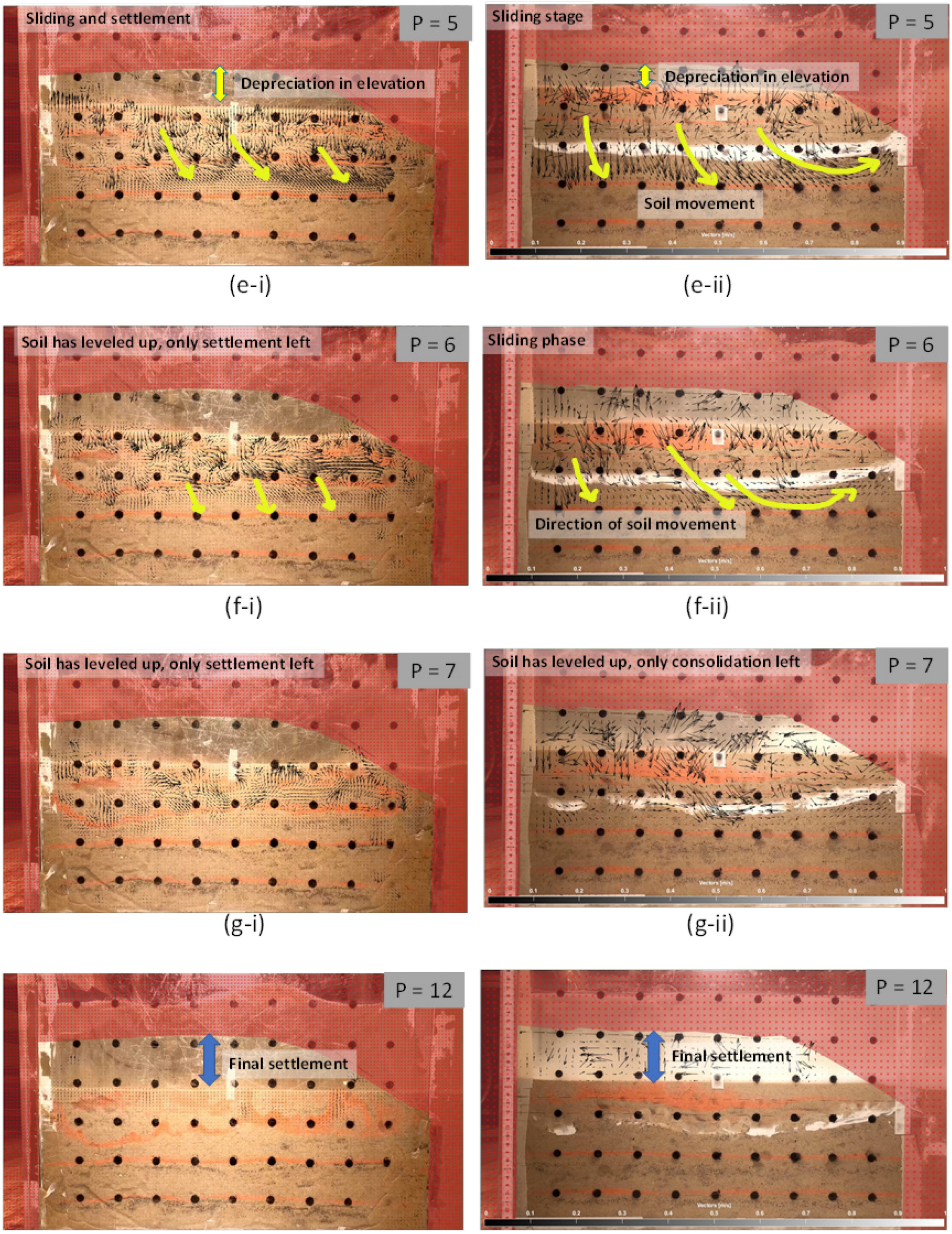

(e-i) (e-ii)

(f-i) (f-ii)

(g-i) (g-ii)

(h-i) (h-ii)

Figure 3.7 Particle deformation vectors during the 1g soil model shaking with (i) no cap layer, (ii) cap layer for: (a) Pair 1, (b) Pair 2, (c) Pair 3, (d) Pair 4, (e) Pair 5, (f) Pair 6, (g) Pair 7 and (h) Pair 8.

3.5.3 Generalised particle movement trend

From the vector profile a generalized particle movement trend was generated, and the soil profile was divided into different zones based on the general particle movement direction. The particle movement trend for Case I is shown in Figure 3.8a, while the profile for Case II is depicted in Figure 3.8b. The soil model was divided into three zones (I, II and III) based on the particle vector direction. Zone I is the upstream section of the slope, Zone II is the middle section, while Zone III is the downstream section of the slope. For Case I, it was observed that, the zone I experienced mainly vertical settlement of soil particles, while in Zone II, the particle moved in vertical as well as lateral direction towards the downstream side. Furthermore, in the Zone III, the soil movement was mainly in the lateral direction due to the thrust from upstream soil motion. While for Case II, the Zone I saw vertical as well as lateral movement of soil, while Zone II and III had almost similar. Although, a scooping effect was observed in Case II, in which the downward movement of overlying soil tried to suppress the cap layer and then push it out from the soil barrier.

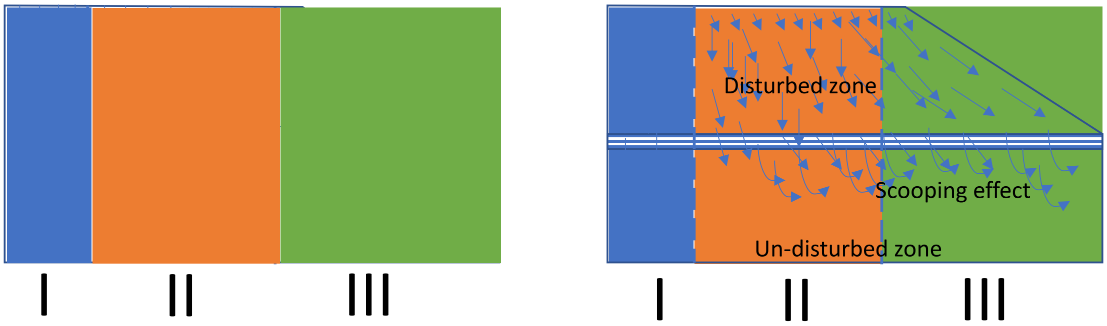

(a) (b)

Figure 3.8 Generalized particle vector profile for (a) Case I and (b) Case II.

3.5.4 Assessment of soil surface post shaking

The model in Case II was allowed to settle for some time after the shaking. A thin film of Kaolin had formed on the sand surface (Figure 3.9 a) due to the formation of sand boils, which are clearly visible after removal of the overhead water (Figure 3.9 b). The layers were excavated to see the integrity of underlying capping layer, and it was found that the capping layer was partially intact (Figure 3.9 c). During the field investigations, very thin silt seams were found wedged in between the gravelly and sandy layers (see Figure 2.19), this kind of activity through which a large amount of fine soil sediments are ejected from the underlying layers could be one of the reasons of formation of very thin seams.

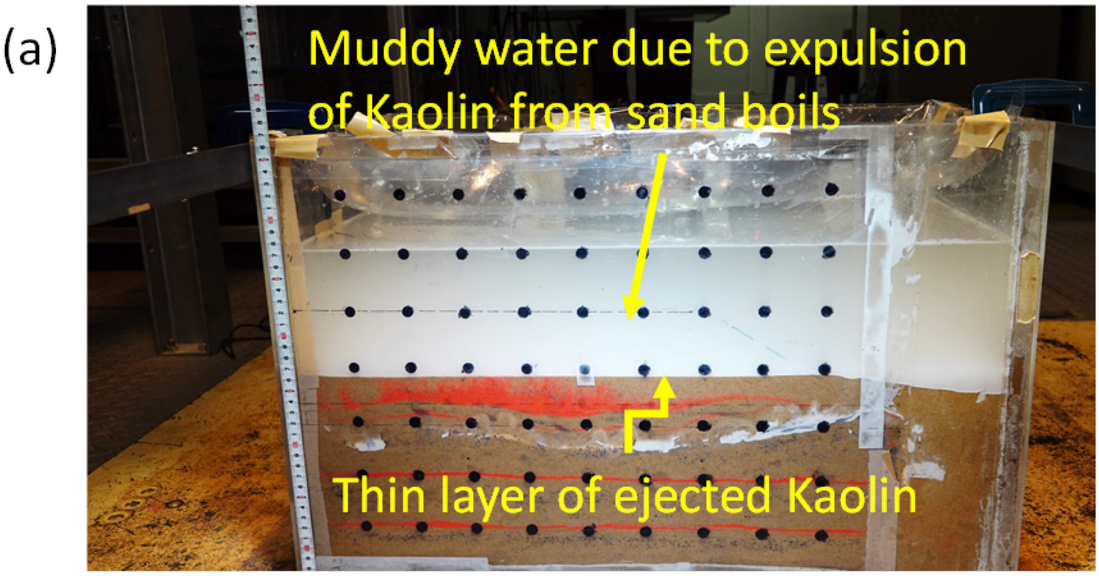

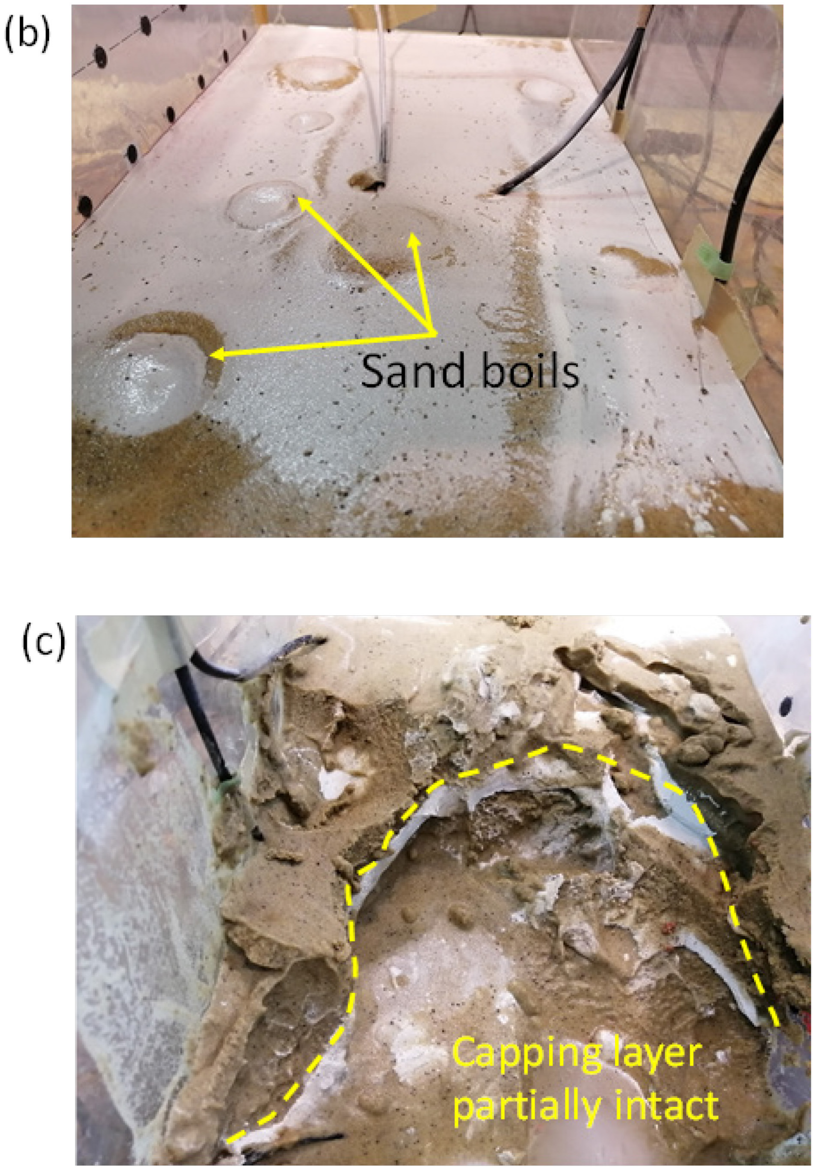

Figure 3.9 Post-shaking assessment of the soil surface: (a) formation of thin clay seam ejecta on surface, (b) location of sand boils and (c) integrity of capping layer.

3.6 CONCLUSIONS

A preliminary study on soil models with and without capping layers on a 1g shaking table was performed. The model was imparted with an input motion and the particle movement was evaluated using particle image velocimetry (PIV) technique. A generalized deformation profile was developed from the particle vector direction during the shaking. As it was a demonstrative study, therefore the similitude laws were not considered during modelling. Following outcomes were achieved from the tests:

- Presence of capping layers delayed the initiation of sliding in soil layers by about 4 secs.
- Upward migration of water from underlying layers was observed in both the cases, however sand boils were clearly defined in Case II due to higher upward hydraulic pressure developed under the capping layer.
- Formation of multiple sand boils in a small area may also be a reason for the water film to not form.
- As the soil particles from upstream tried to destabilize and scoop out the cap layer, it caused the deformation in soil layer up to deeper depth.
- It was observed on excavation that, the cap layer was partially intact after the shaking.

REFERENCES

Berrill, J. B., Christensen, S. A., Keenan, R. P., Okada, W., & Pettinga, J. R. (2001). Case study of lateral spreading forces on a piled foundation. *Geotechnique*, *51*(6), 501–517.

Bolton, S. H. (1987). Design Problems in Soil Liquefaction. *Journal of Geotechnical Engineering*, *113*(8), 827–845.

Carey, T., Stone, N., Kutter, B., & Hajialilue-Bonab, M. (2018). A new procedure for tracking displacements of submerged sloping ground in centrifuge testing. *Physical Modelling in Geotechnics*, 829–834.

Coulter, H. W., & Migiliaccio, R. . (1966). *Effects of theeEarthquake of March 27,* *1964 at Valdez, Alaska. Geological Survey Professional Paper 542-C, US Department of the Interior*.

Field, M. E., Gardner, J. V., Jennings, A. E., & Edwards, B. D. (1982). Earthquake-induced sediment failures on a 0.25 o slope, Klamath River delta, California. *Geology*, *10*(10), 542–546.

Hazarika, H., Rohit, D., Pasha, S. M. K., Maeda, T., Masyhur, I., Arsyad, A., & Nurdin, S. (2021). Large distance flow-slide at Jono-Oge due to the 2018 Sulawesi Earthquake, Indonesia. *Soils and Foundations*, *61*(1), 239–255.

JICA, J. I. C. A. (2019). *Report of the technical committee on The 2018 Sulawesi earthquake, Indonesia*.

Kamai, R., Boulanger, R. W., Kano, S., Marinucci, A., Howell, R., Rathje, E., Conlee, C., & Gallagher, P. (2008). Effects of void redistribution on post-earthquake residual strengths for liquefiable soils. *Association of Dam Safety Officials - Dam Safety 2008*.

Kawakita, S., Asahina, D., Takemura, T., Hosono, H., & Kitajima, K. (2020). Effect of hydraulic and mechanical characteristics of sediment layers on water film formation in submarine landslides. *Progress in Earth and Planetary Science*, *7*(1).

Knappett, J. A., Haigh, S. K., & Madabhushi, S. P. G. (2006). Mechanism of failure for shallow foundations under earthquake loading. *Soil Dynamics and Earthquake Engineering*, *26*, 91–102.

Kokusho, T. (1999). Water film in liquefied sand and its effect on lateral spread. *Journal of Geotechnical and Geoenvironmental Engineering*, *125*(10), 817–826.

Kokusho, T. (2000). Mechanism for Water Film Generation and Lateral Flow in liquified Sand Layer. *Soils and Foundations*, *40*(5), 99–111.

Kokusho, T. (2003). Current state of research on flow failure considering void redistribution in liquefied deposits. *Soil Dynamics and Earthquake Engineering*, *23*(7), 585–603.

Kokusho, T., & Kabasawa, K. (2003). Effect of void redistribution or water films on shear strength of liquefied deposits. *First Japan-U.S. Workshop on Testing, Modeling, and Simulation*, 475–503.

Lam, S. Y., Elshafie, M. Z. E. B., Haigh, S. K., & Bolton, M. D. (2012). A new apparatus for modelling excavations. *International Journal of Physical Modelling in Geotechnics*, *12*(1), 24–38.

Lemke, R. (1967). Effects of the earthquake of March 27, 1964 at Seward, Alaska. *Geological Survey Professional Paper*, *542-E*, 53.

Malvick, E. J., Kutter, B. L., Boulanger, R. W., & Kulasingam, R. (2006). Shear Localization Due to Liquefaction-Induced Void Redistribution in a Layered Infinite Slope. *Journal of Geotechnical and Geoenvironmental Engineering*, *132*(10), 1293–1303.

National Research Council. (1985). *Liquefaction of Soils During Earthquakes.* The National Academy Press. https://doi.org/10.17226/19275

Soria, J. (1996). An investigation of the near wake of a circular cylinder using a video-based digital cross-correlation particle image velocimetry technique. *Experimental Thermal and Fluid Science*, *12*(2), 221–233.

Tan, K. Q., Tung, Q. Y., Lee, F. H., & Goh, S. H. (2015). Enhancing images for particle image velocimetry in centrifuge models. *15th Asian Regional Conference on Soil*

Mechanics and Geotechnical Engineering, ARC 2015: New Innovations and Sustainability, 2553–2558. https://doi.org/10.3208/jgssp.SIN-05

Thielicke, W., & Sonntag, R. (2021). Particle Image Velocimetry for MATLAB: Accuracy and enhanced algorithms in PIVlab. *Journal of Open Research Software*, *9*(12). https://doi.org/10.5334/jors.334

Yang, Z., & Elgamal, A. (2001). Sand Boils and Liquefaction--Induced Lateral Deformation. *15th International Conference on Soil Mechanics and Geotechnical Engineering*, *1989*, 345–350.

Yang, Z., & Elgamal, A. (2002). Influence of Permeability on Liquefaction-Induced Shear deformation. *Journal of Engineering Mechanics*, *128*(7), 720–729.

CHAPTER 4

ONE-DIMENSIONAL SOIL COLUMN SIMULATION UNDER IMPACT LOAD

4.1 INTRODUCTION

During the site investigation of the flowslide sites, it was observed that the soil stratification in the flowslide areas was highly heterogenous and had alternating layers of low and high permeability soil. At each trench it was observed that the alternating cap layers had different soil characteristics like plasticity and grain size based on visual observation. Kokusho et. al. (2004) elaborated that in soil layers where the overlying layer is a capping layer and the underlying layer is permeable and loose, a phenomenon called 'void redistribution' may occur in which the diffusion of excess pore water pressure (EPWP) from the liquefied underlying soil may lead to softening and strength loss at the interface between the capping layer and underlying permeable layer. This mechanism is also considered to be the key mechanism behind many liquefaction induced flow failures (Malvick et al., 2006; Mason et al., 2021). Model tests conducted on one dimensional soil columns have shown that, on impact, the cap layer tends to inhibit the dissipation of excess pore water pressure from underlying liquefied layers, thereby delaying the settlement of overall soil layers. It was also observed that, due to high hydraulic gradient underneath the cap layer, the overlying layer practically levitates over the water film till it disperses (Kokusho, 1999; 2000; Kokusho & Fujita, 2002; Kokusho, 2003; Rohit et al., 2021; Rohit et al., 2021). The high hydraulic gradient is also one of the factor responsible for the formation of sand boils post liquefaction, also the size of the sand boil depends on the volume of water accumulated in the water film (Kamai et al., 2008;.Yang & Elgamal, 2001). These studies have mostly used a uniform sand with either non-plastic fines or a clay as a cap layer. Although, in actual field conditions, multiple cap layer tend to exist at any particular location, also these cap layers may or may not be of same plasticity characteristics as observed during the field investigation of Palu flowslide sites (Hazarika et al., 2021; Kiyota et al., 2020; Okamura et al., 2020). There in order to simulate the effect of multiple cap layers with similar and different plasticity characteristics one dimensional (1D) soil column tests were conducted under the influence of impact load. The influence of soil heterogeneity on the magnitude and dissipation of excess pore water pressure is discussed along with the water film formation and soil settlement.

4.2 TEST SETUP

To simulate the formation of water film in a stratified soil, a simple one-dimensional soil model was prepared in a lucite tube of 9.6 cm diameter and 100 cm height. Toyoura sand was used as the permeable sand layer while Pearl clay (CL) and non-plastic (NP) fines with particle size <0.075 mm sieved from sand available in-house were used as capping layers. The properties of the sand and clay materials are given in Figure 4.1 a. The properties of Pearl clay are sourced from Sun et. al., (2004). The layers were prepared by air pluviating the sand at a calibrated height to maintain the relative density of approximately 50% throughout the height of the soil column. The thickness of clay and NP fines was kept 2 cm for all the tests with uniform mass maintained across all the tests. The 1D soil setup was imparted with an impact load using a concrete cylinder suspended from metal chains. The concrete cylinder had a mass of 3.77 kg, diameter 10 cm and height 20 cm. The setup was imparted with two shocks at the base, second shock greater than the first (Figure 4.1 b and Figure 4.2).

The second shock imparted after the EPWP completely normalized from the first shock. The kinetic energy (KE) imparted in each shock was controlled by maintaining the distance and height of release. It was taken care that the cylinder does not rebound and hit the setup again.

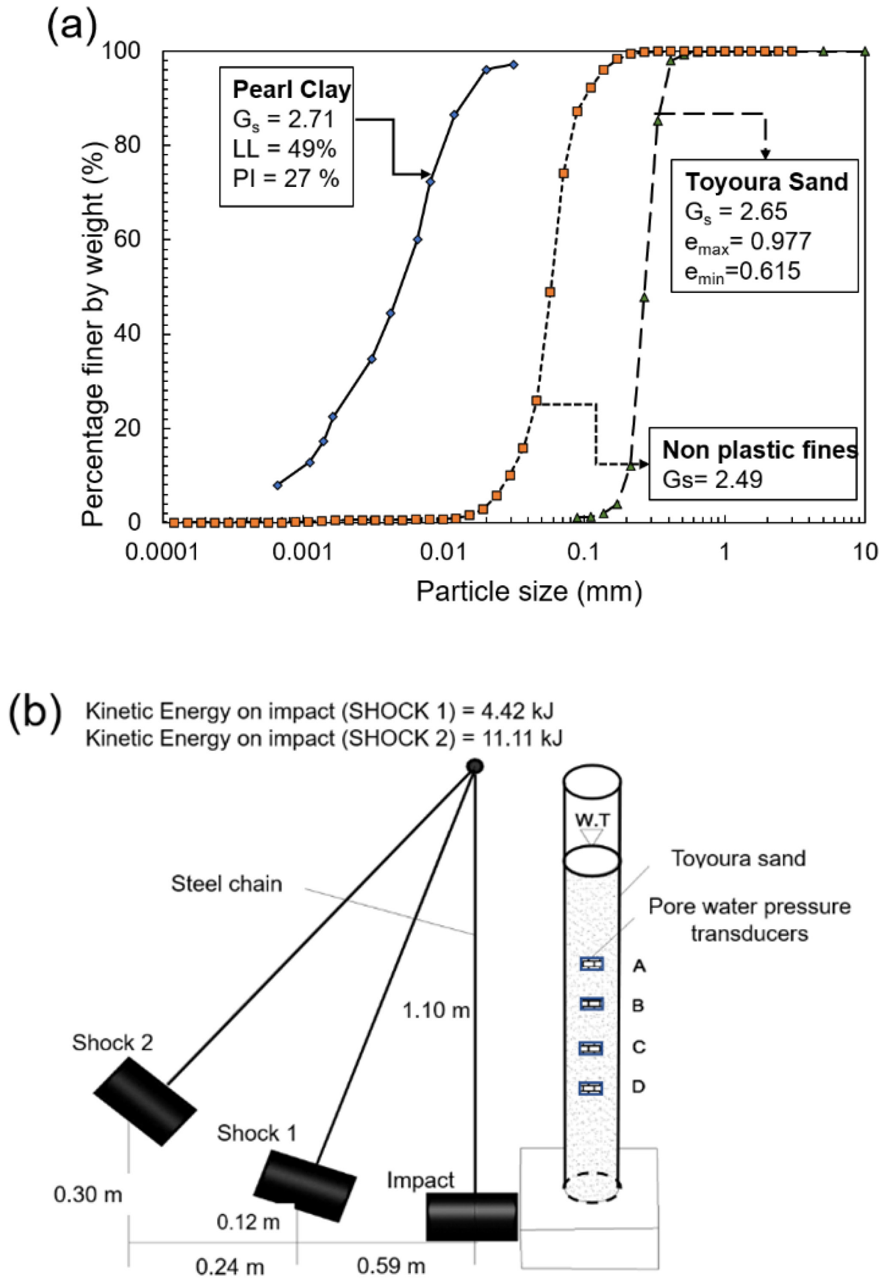

Figure 4.1 Experimental model setup: (a) properties of the soil material used and (b) setup for shock loading.

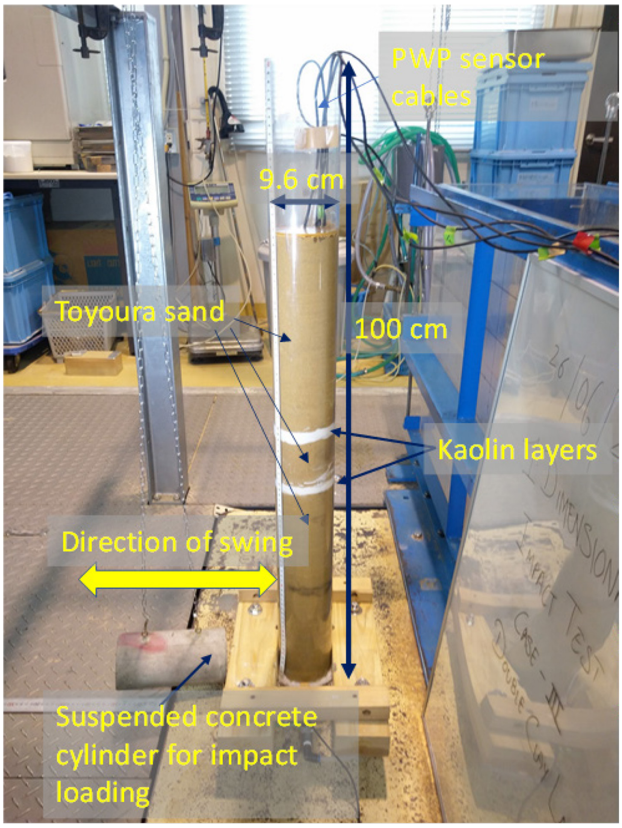

Figure 4.2 Actual setup for 1D soil column impact test.

Furthermore, to study different stratification conditions, four typical cases were considered as follows: Case I: only sand layer; Case II: a clay seam wedged between sand layers; Case III: two clay seams wedged between sand layers and Case IV: a clay seam at shallow depth and a NP fines layer at deeper depth. To record the change in EPWP in the soil, four PWP transducers namely A, B, C and D were placed at different heights (Figures 4.3 a~d).

As soon as the soil model was imparted with the shock through the concrete cylinder released from a calibrated height, the EPWP reached to its peak. The build-up and dissipation of EPWP was recorded through the transducers with a time step of 0.02 seconds. The role of low permeability fine soil layers (silt/clay) as a capillary barrier against the vertical flow of pore water on shock loading is evaluated for various stratification conditions

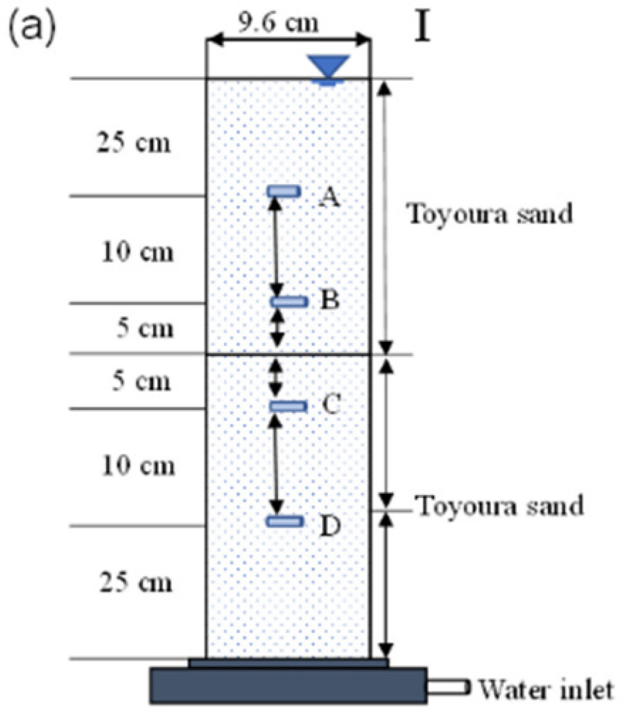
(a)
9.6 cm
I
25 cm
A
Toyoura sand
10 cm
B
5 cm
5 cm
C
10 cm
Toyoura sand
D
25 cm
Water inlet

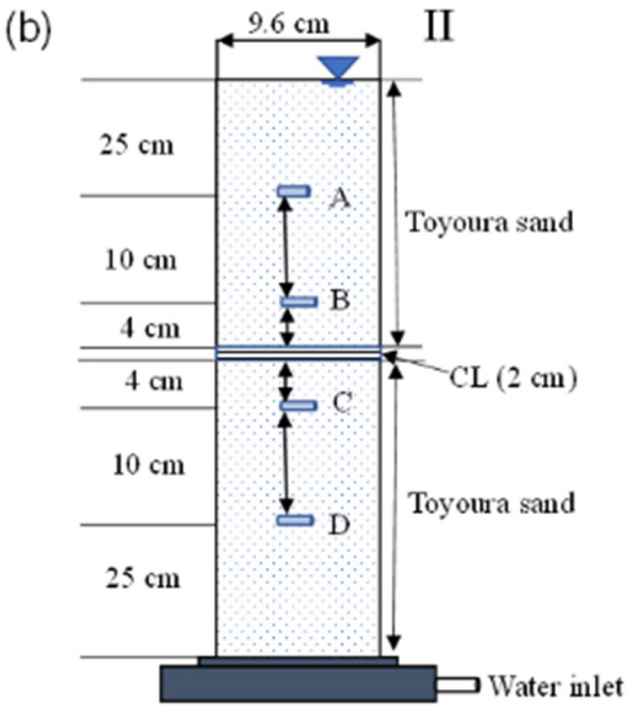
(b)
9.6 cm
II
25 cm
A
Toyoura sand
10 cm
B
4 cm
CL (2 cm)
4 cm
C
10 cm
Toyoura sand
D
25 cm
Water inlet

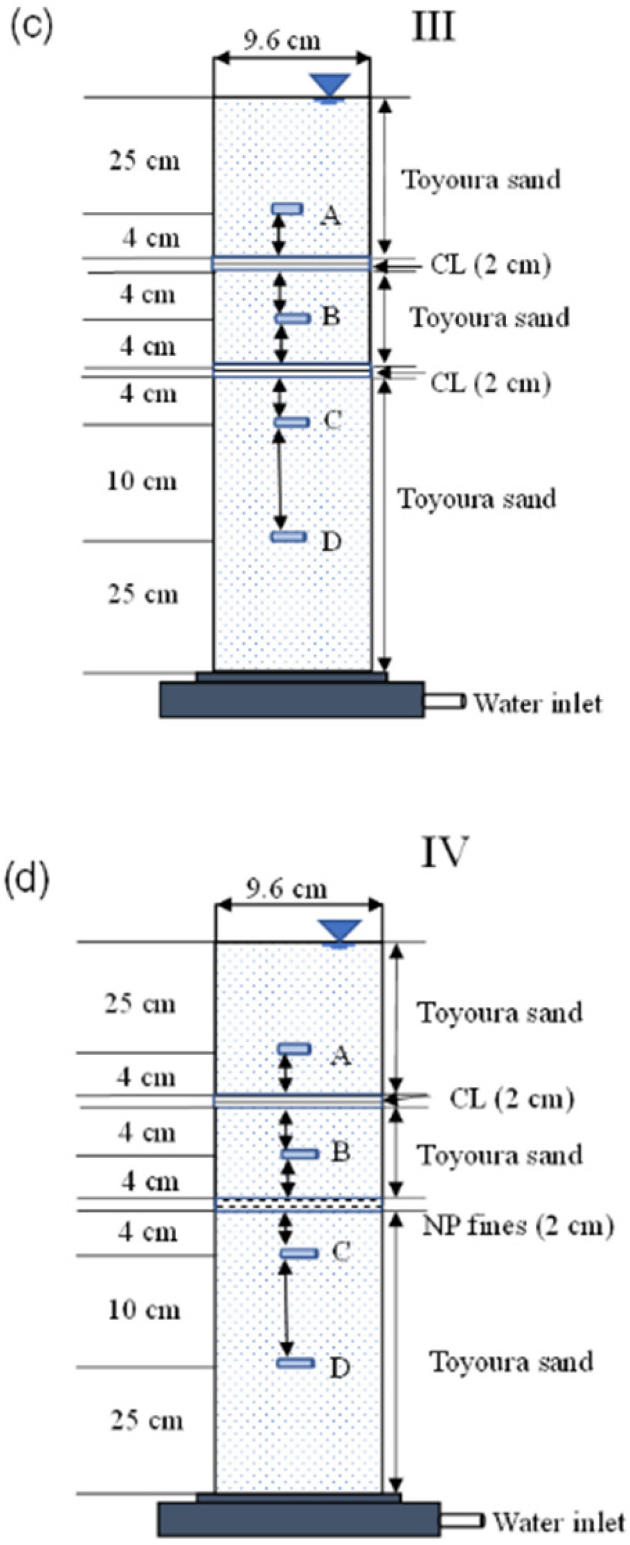

Figure 4.3 Parametric cases for 1D model test: (a) Case I: only toyoura sand; (b) Case II: single clay layer; (c) Case III: two clay layers and (d) Case IV: top clay layer and bottom NP fines layer.

4.3 RESULTS AND DISCUSSIONS

4.3.1 Dissipation of excess pore water pressure (EPWP) with respect to time

To evaluate the effect of presence of clay or silt layers on the dissipation of EPWP after the peak pore pressure is reached, the change in EPWP (Δu) is normalized to the change in maximum EPWP (Δu_{max}) and plotted against elapsed time (Figure 4.4 a~d). Each plot has an inset plot of maximum EPWP at respective PWP transducer, represented as a function of overburden stress (R_u). Here in Figure 4.4 a, where no capping layer is present (Case I), the EPWP once built-up, dissipates within 10 – 20 seconds for all the transducers for both the small (Shock 1) and large shock (Shock 2). In Figure 4.4 b, the presence of single clay layer (Case II), inhibits the dissipation of EPWP for transducers C and D as the delay can be easily observed in the plots. Furthermore, Case III, all the PWP transducers (B, C and D) placed below the clay layers show a much-delayed dissipation in the EPWP (Figure 4.4 c), due the presence of two hydraulic barriers. For Case IV where upper capping layer is of clay while lower layer is of NP fines (Figure 4.4 d), the EPWP just below the clay layer dissipates with a longer duration as compared to below the NP fines layer. This is due to the lower permeability of the clay as compared to the NP fines.

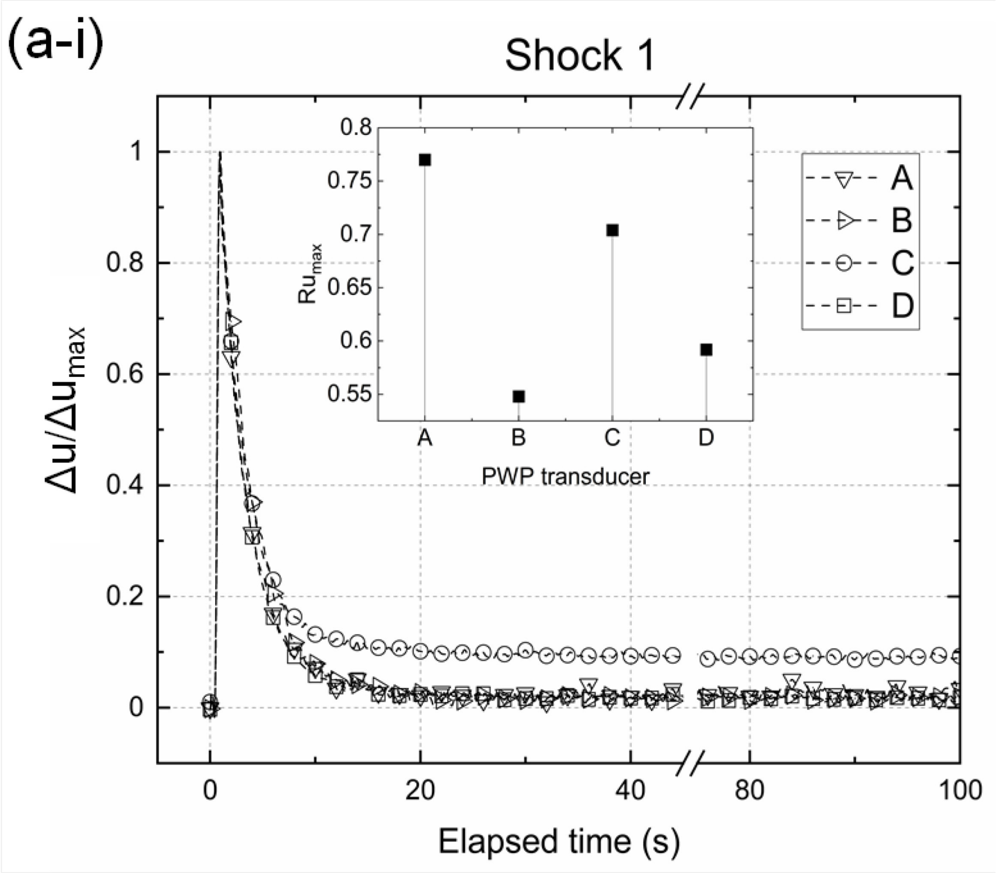
(a-i)
Shock 1
Δu/Δu_max
1
0.8
0.6
0.4
0.2
0
0
20
40
80
100
Elapsed time (s)
A
B
C
D
Ru_max
0.8
0.75
0.7
0.65
0.6
0.55
A
B
C
D
PWP transducer

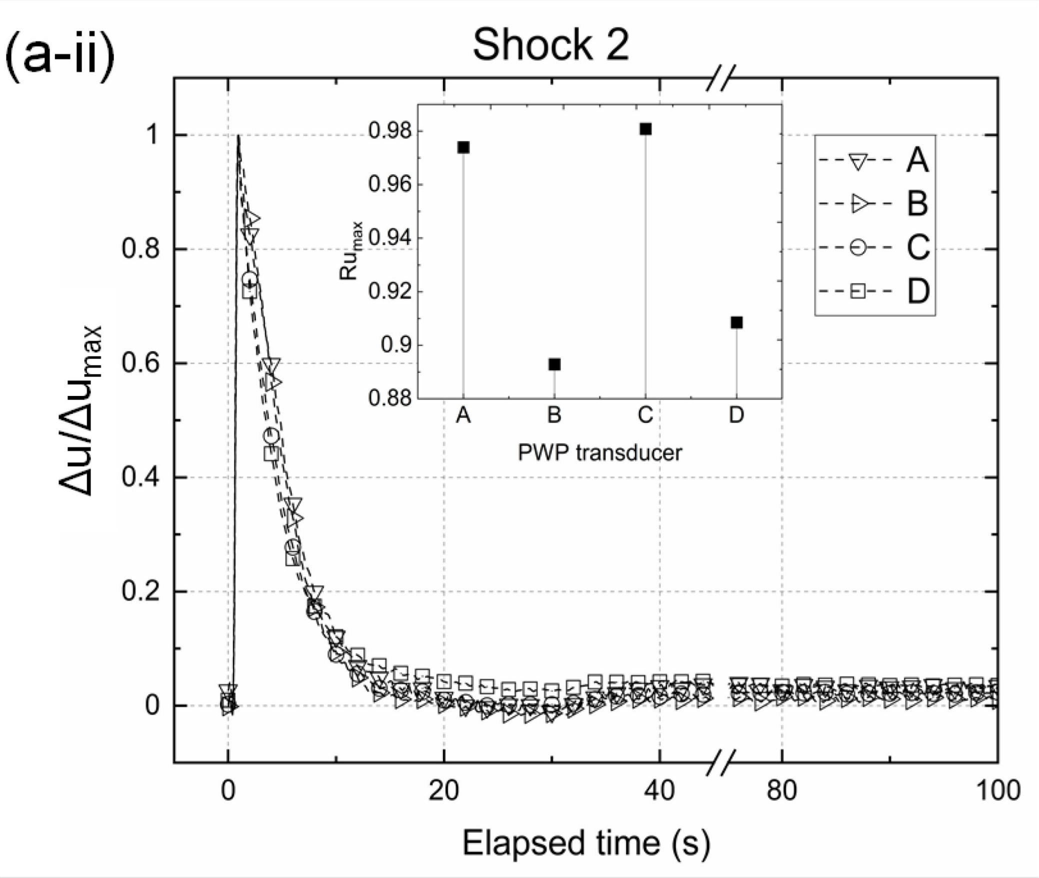
(a-ii)
Shock 2
Δu/Δu_max
1
0.8
0.6
0.4
0.2
0
0
20
40
80
100
Elapsed time (s)
A
B
C
D
Ru_max
0.98
0.96
0.94
0.92
0.9
0.88
A
B
C
D
PWP transducer

(b-i)

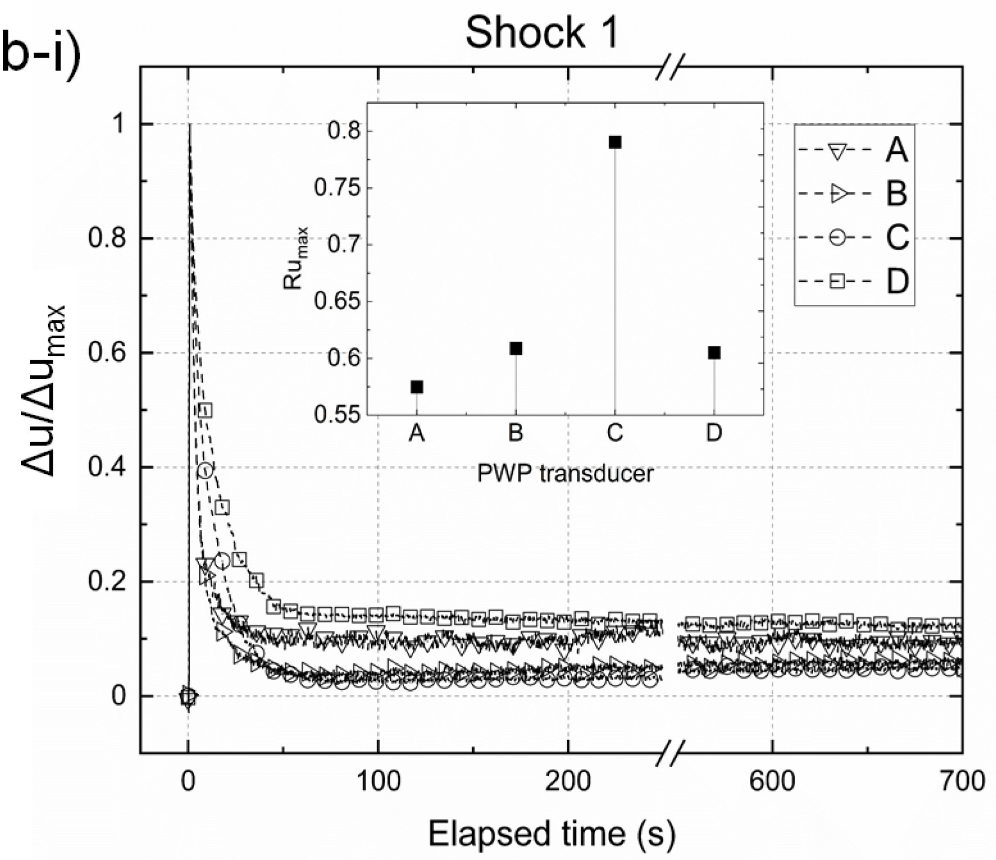
Shock 1
Δu/Δu_max
1
0.8
0.6
0.4
0.2
0
0
100
200
600
700
Elapsed time (s)
Ru_max
0.8
0.75
0.7
0.65
0.6
0.55
A
B
C
D
PWP transducer
A
B
C
D

(b-ii)

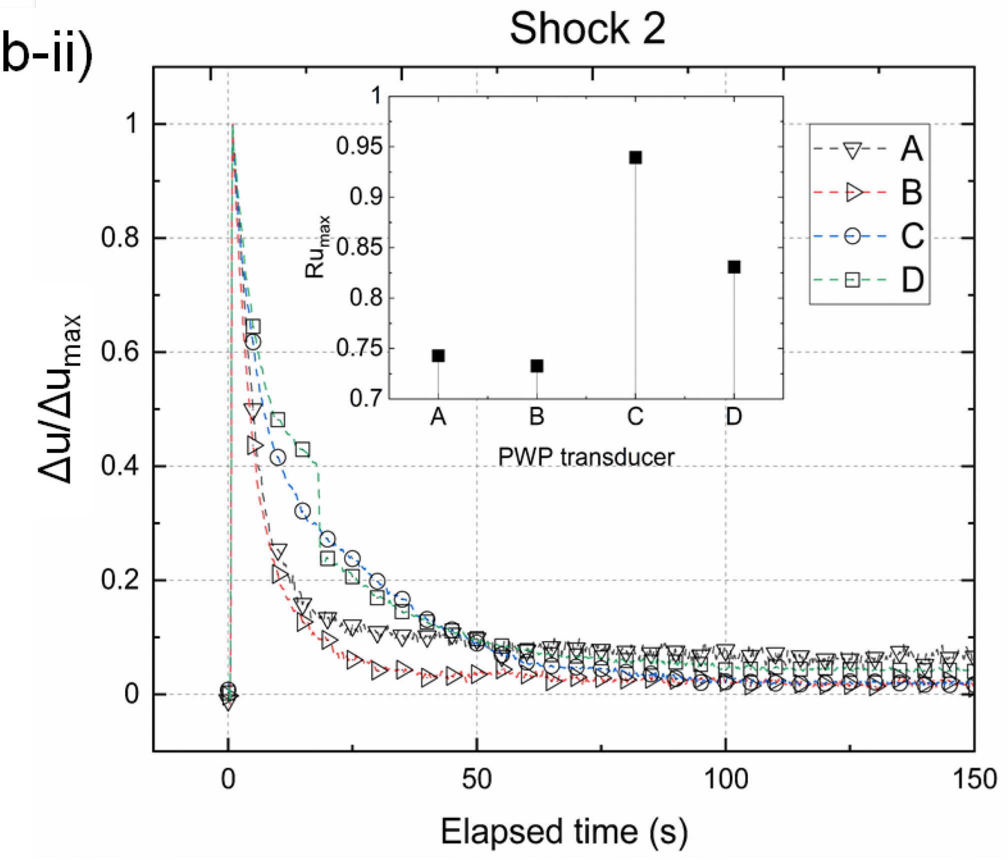
Shock 2
Δu/Δu_max
1
0.8
0.6
0.4
0.2
0
0
50
100
150
Elapsed time (s)
Ru_max
1
0.95
0.9
0.85
0.8
0.75
0.7
A
B
C
D
PWP transducer
A
B
C
D

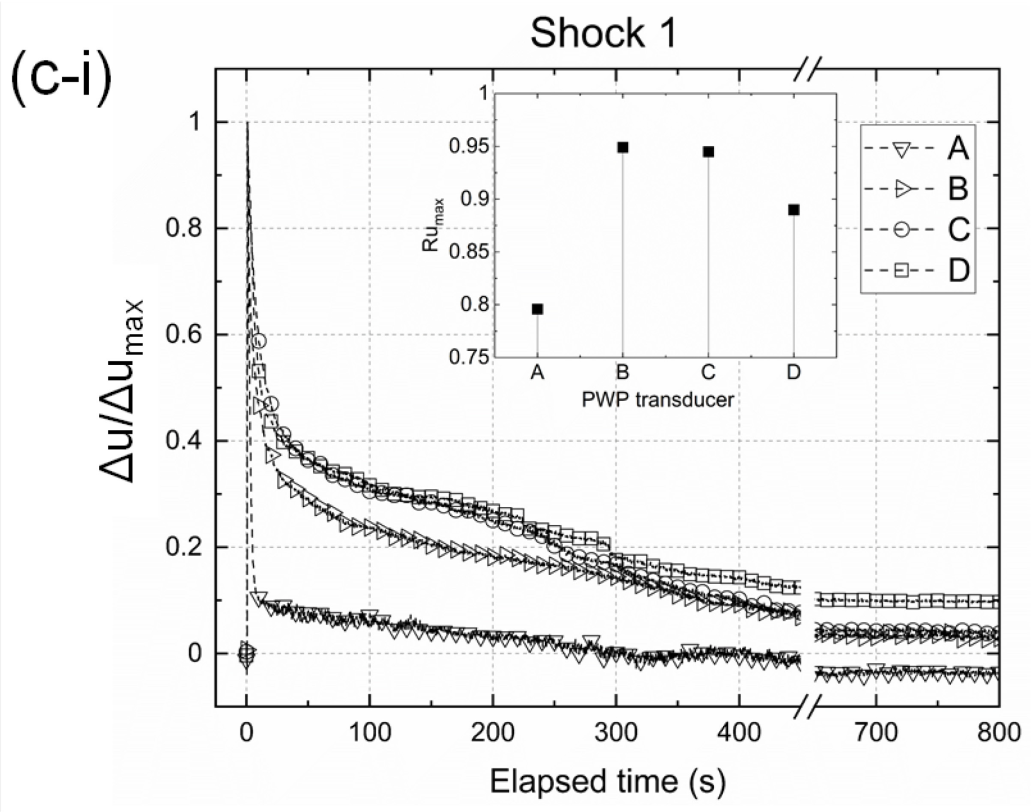
(c-i)
Shock 1
Δu/Δu_max
1
0.8
0.6
0.4
0.2
0
0
100
200
300
400
700
800
Elapsed time (s)
A
B
C
D
Ru_max
1
0.95
0.9
0.85
0.8
0.75
A
B
C
D
PWP transducer

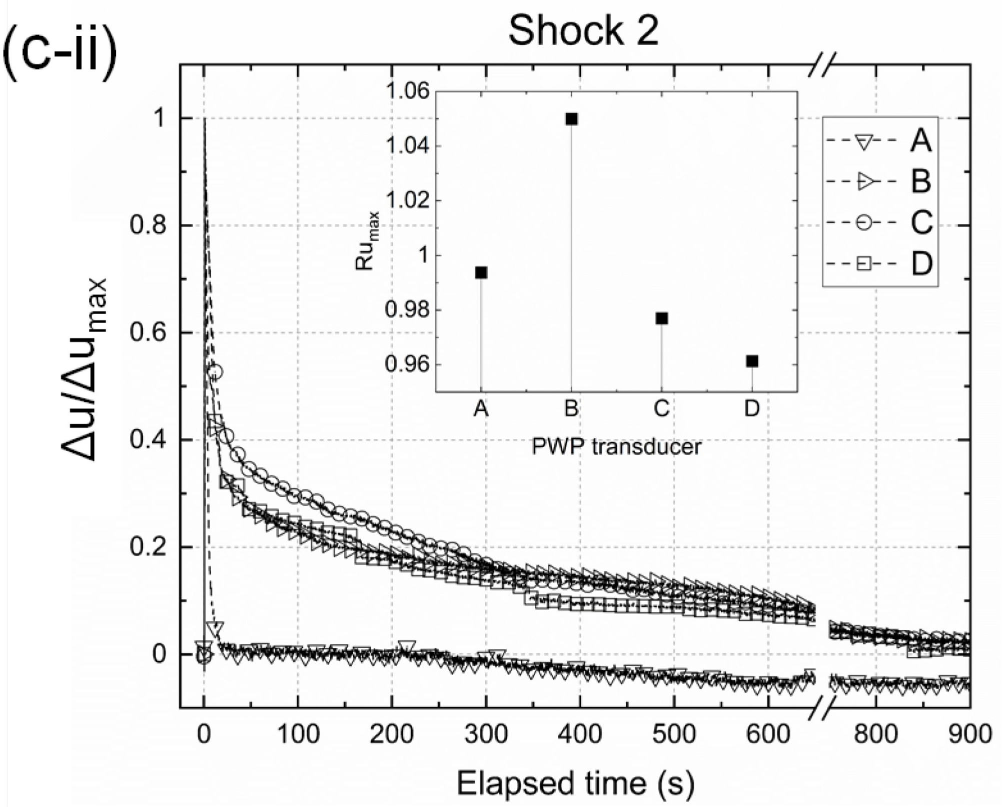
(c-ii)
Shock 2
Δu/Δu_max
1
0.8
0.6
0.4
0.2
0
0
100
200
300
400
500
600
800
900
Elapsed time (s)
A
B
C
D
Ru_max
1.06
1.04
1.02
1
0.98
0.96
A
B
C
D
PWP transducer

(d-i)

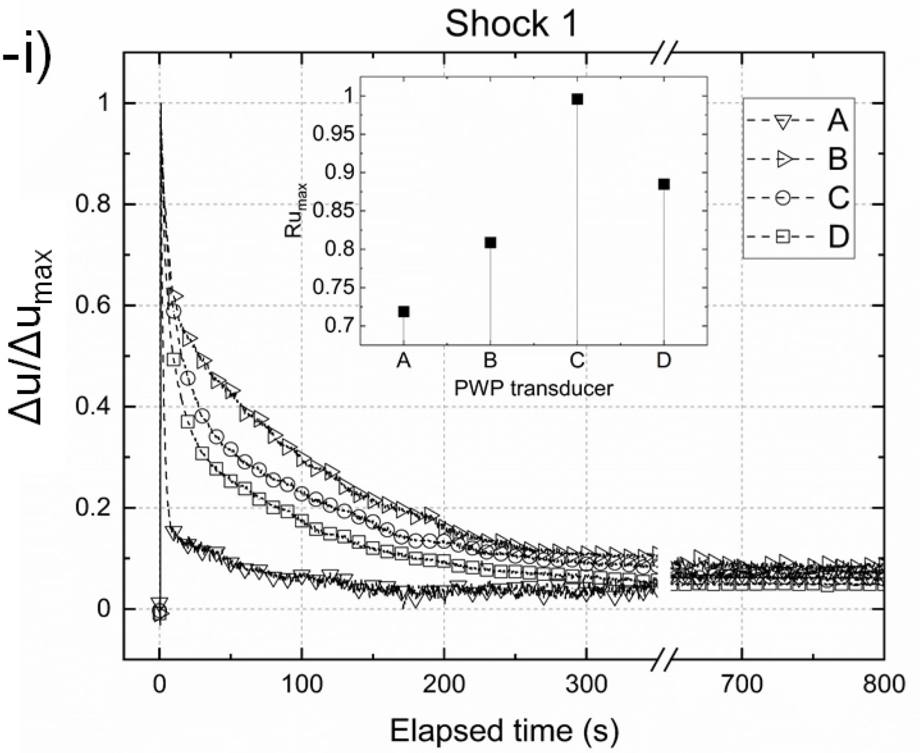

(d-ii)

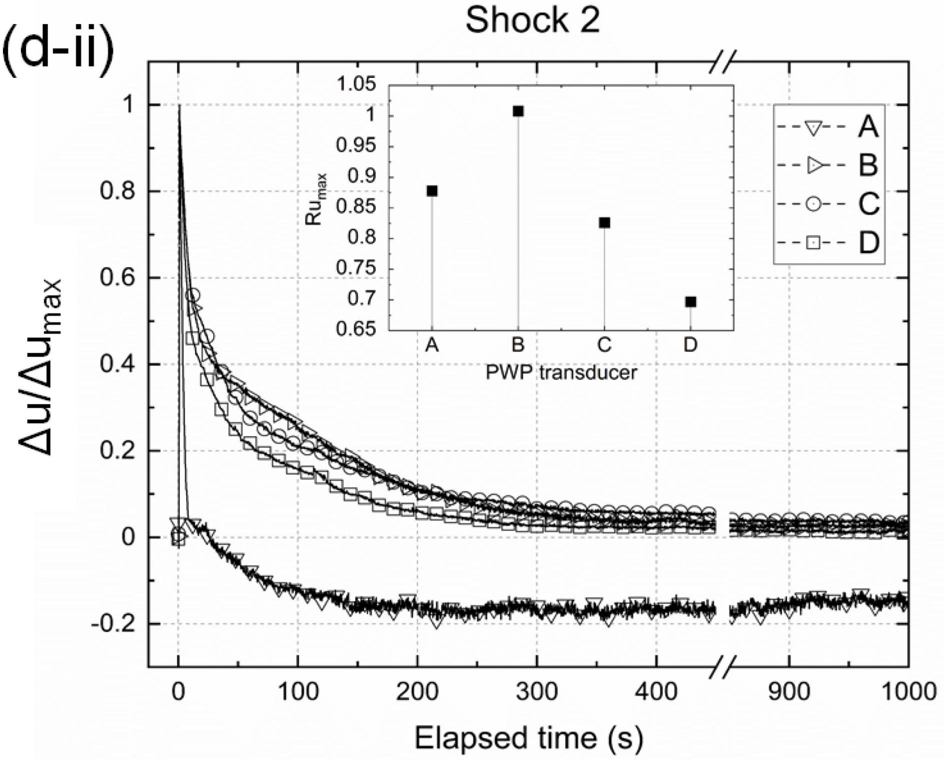

Figure 4.4 Dissipation of normalized change in excess pore water pressure with respect to elapsed time: (a-i,a-ii) Case I; (b-i,b-ii) Case II; (c-i,c-ii) Case III and (d-i,d-ii) Case IV.

4.3.2 Vertical dissipation profile of the pore water pressure

To evaluate the pore pressure variation simultaneously across the soil column height, the EPWP is plotted at different time intervals against the normalized height of the transducers (Figure 4.5a~d). Here the time t=0 means the time of peak EPWP in the soil column. The locations of the capping layers are depicted through dotted lines and the data points denote the locations of the PWP transducers. It should be noted that the clay layer is denoted as CL. Here in Figure 4.5a, the maximum EPWP is measured at the bottom of the soil column and the minimum near the surface. With the passage of time after the impact, a quick dissipation is observed. Also, it can be seen that the pressure distribution is not linear across the height, which can be attributed to a slight variation in relative density of the soil while model preparation. For Case II in Figure 4.5b, with the presence of single clay layer, a sharp increase in the EPWP below the clay layer is observed with a delayed dissipation below the layer. Furthermore, for Case III in Figure 4.5c, the trend of the EPWP is almost linear with the height initially, but as the dissipation occurs, the trend follows a curved pattern with the maximum value just below the second clay layer. A similar trend is observed for Case IV in Figure 4.5d. In both cases (III and IV), the top three PWP transducers measure linear increase in pore pressure which falls at the bottom. The peak below the second layer in Case III and IV can be attributed to the dual barrier encountered by the pore water to the reach the surface, as the pore water from the bottom layer tries to breach the bottom clay or silt seam, it also experiences additional resistance from the pore water present in the middle layer, which is trying to break or escape the top clay seam. As observed, the presence of a low permeable layer, not only decreases the rate of dissipation but also increases the peak magnitude of excess pore water pressure developed in the underlying layer. In addition to it, the soil does not reach to its initial vertical effective stress condition even after a delayed time interval.

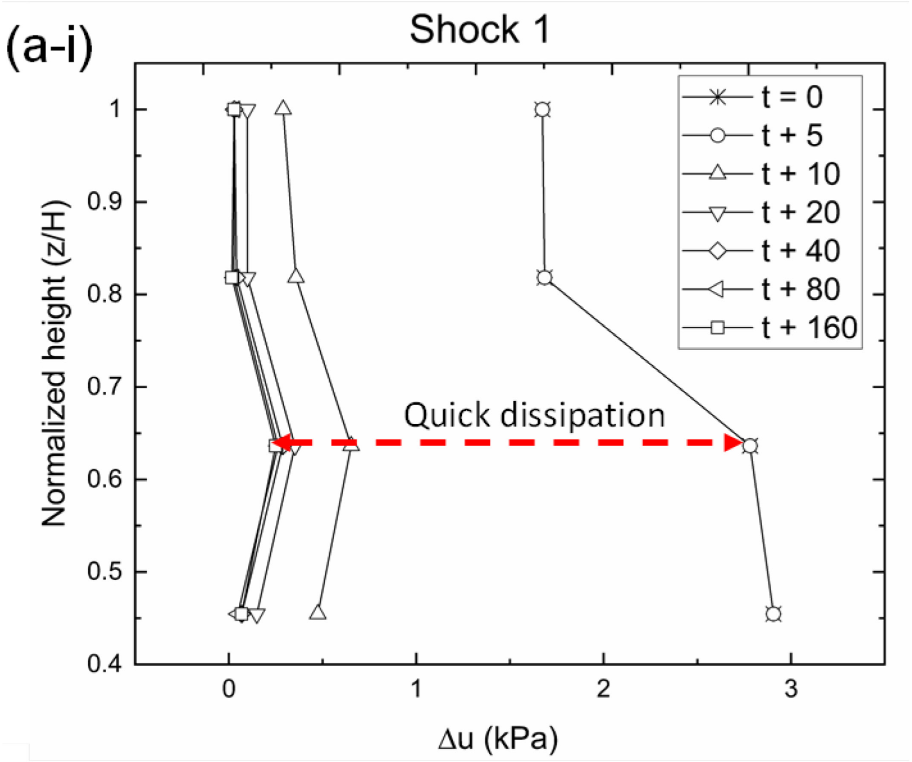

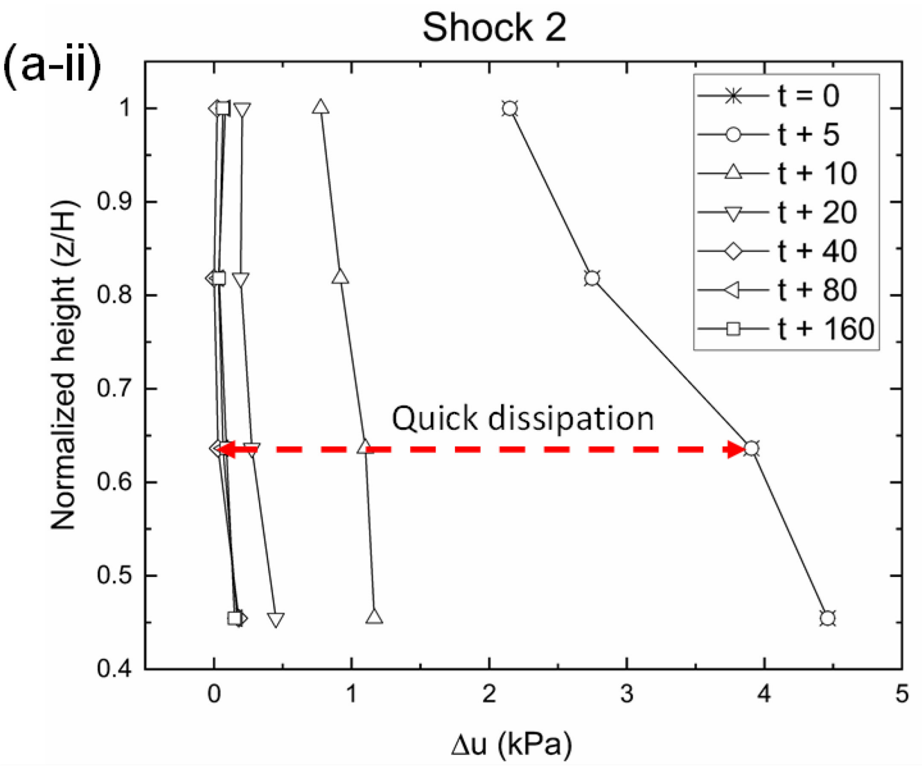

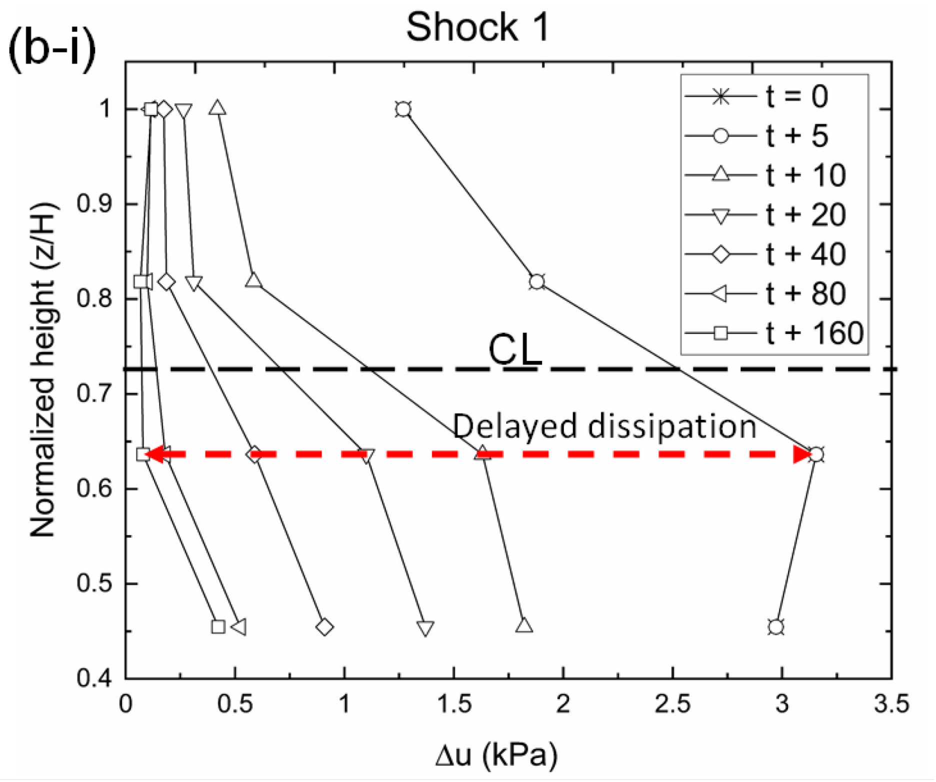
(b-i)
Shock 1
Normalized height (z/H)
Δu (kPa)
t = 0
t + 5
t + 10
t + 20
t + 40
t + 80
t + 160
CL
Delayed dissipation
0.4
0.5
0.6
0.7
0.8
0.9
1
0
0.5
1
1.5
2
2.5
3
3.5

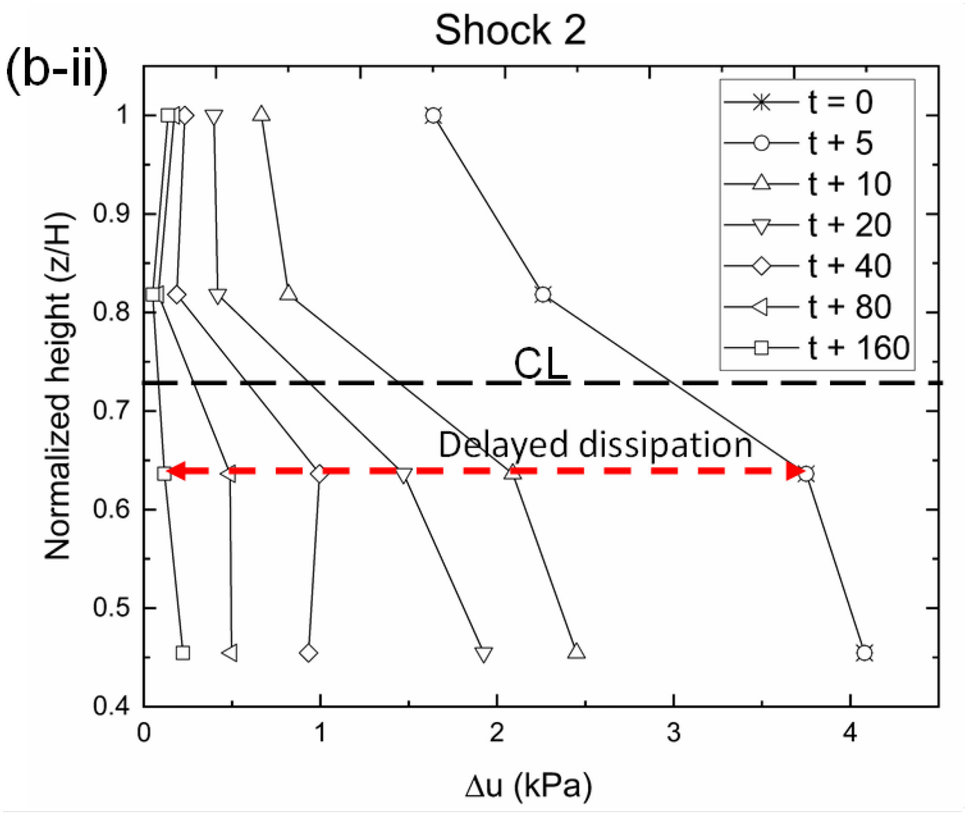
(b-ii)
Shock 2
Normalized height (z/H)
Δu (kPa)
t = 0
t + 5
t + 10
t + 20
t + 40
t + 80
t + 160
CL
Delayed dissipation
0.4
0.5
0.6
0.7
0.8
0.9
1
0
1
2
3
4

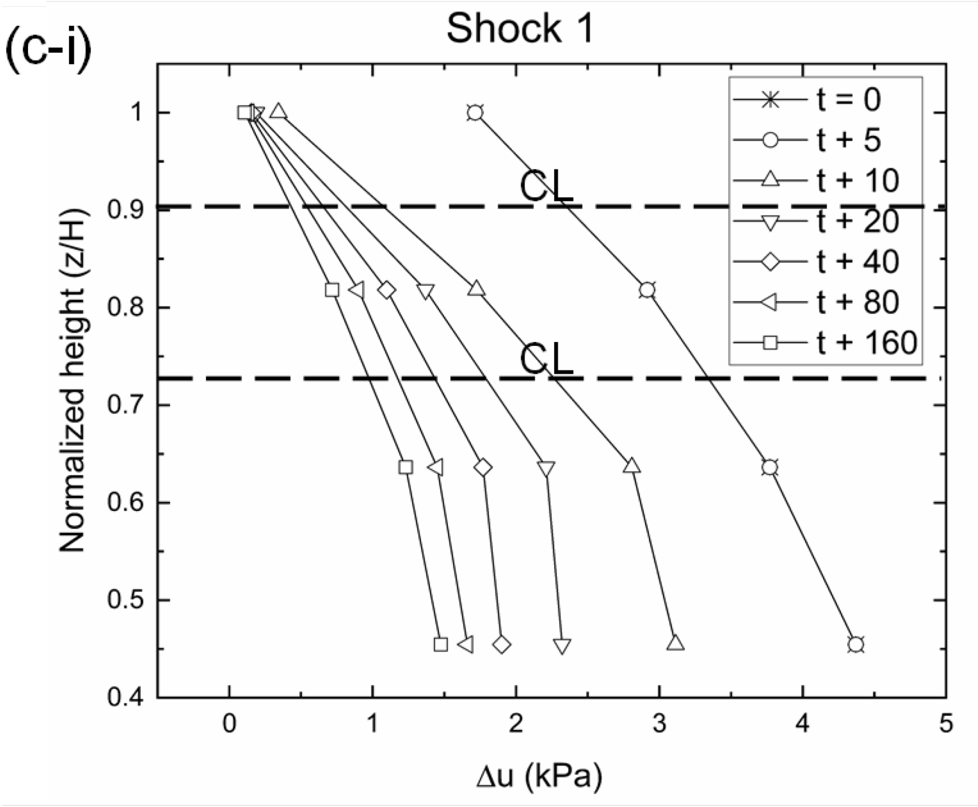
(c-i)
Shock 1
Normalized height (z/H)
Δu (kPa)
0.4
0.5
0.6
0.7
0.8
0.9
1
0
1
2
3
4
5
CL
CL
t = 0
t + 5
t + 10
t + 20
t + 40
t + 80
t + 160

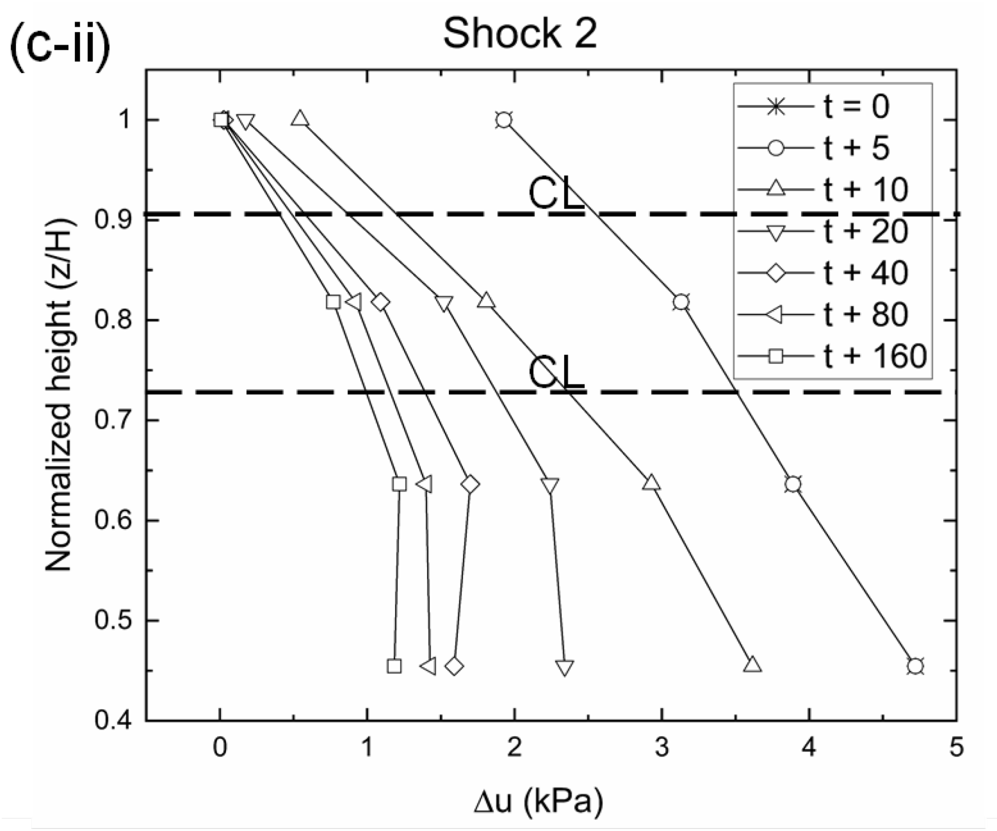
(c-ii)
Shock 2
Normalized height (z/H)
Δu (kPa)
0.4
0.5
0.6
0.7
0.8
0.9
1
0
1
2
3
4
5
CL
CL
t = 0
t + 5
t + 10
t + 20
t + 40
t + 80
t + 160

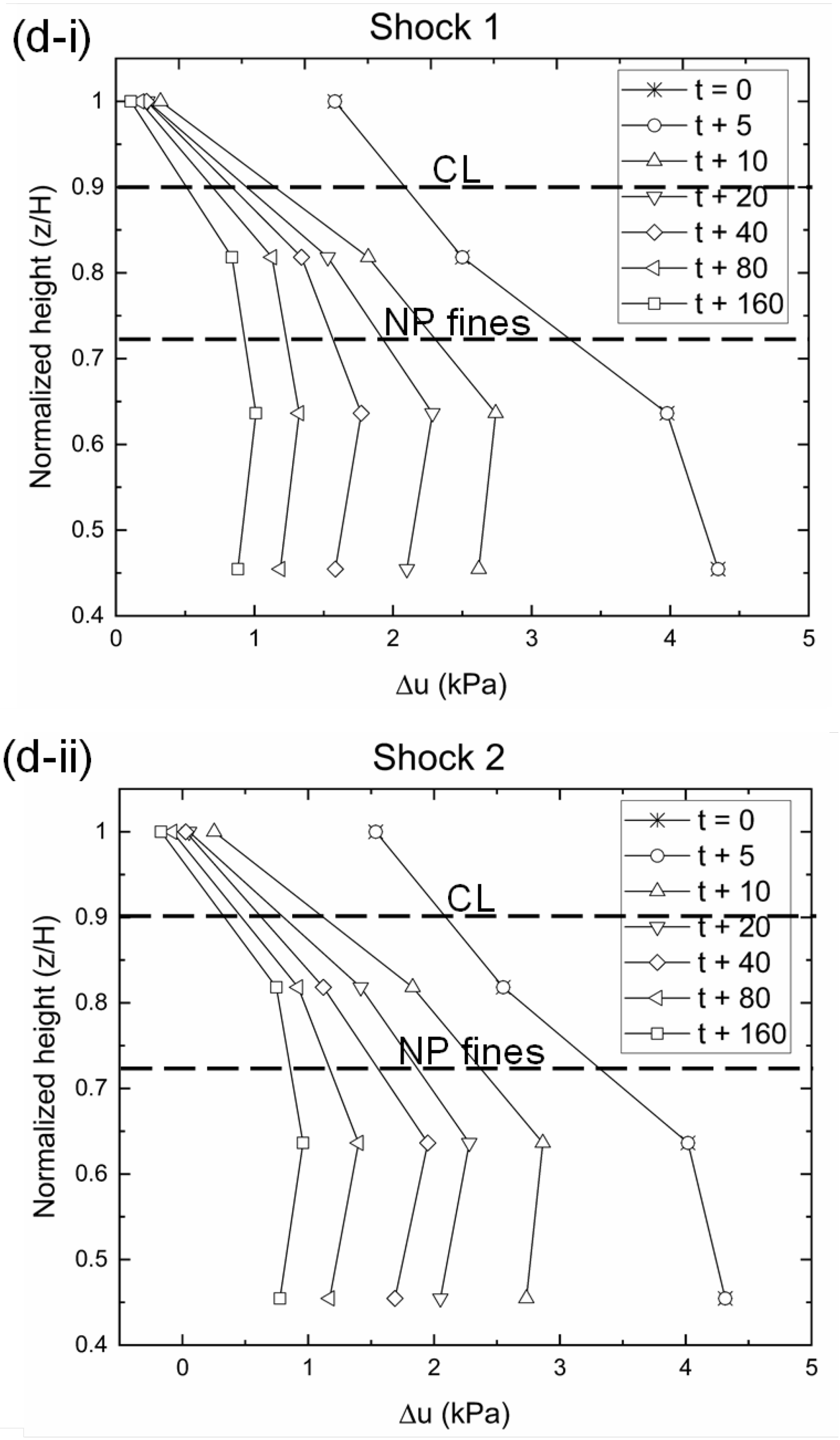
(d-i)
Shock 1
Normalized height (z/H)
Δu (kPa)
t = 0
t + 5
t + 10
t + 20
t + 40
t + 80
t + 160
CL
NP fines
0.4
0.5
0.6
0.7
0.8
0.9
1
0
1
2
3
4
5
(d-ii)
Shock 2
Normalized height (z/H)
Δu (kPa)
t = 0
t + 5
t + 10
t + 20
t + 40
t + 80
t + 160
CL
NP fines
0.4
0.5
0.6
0.7
0.8
0.9
1
0
1
2
3
4
5

Figure 4.5 Variation of change in excess pore pressure with respect to normalized height of sensors location: (a-i, a-ii) Case I; (b-i, b-ii) Case II; (c-i, c-ii) Case III and (d-i, d-ii) Case IV.

4.3.3 Soil settlement

Soil settlement at specific time interval was measured at three different locations, at the top surface for all the cases, at the bottom clay seam for case II, III and IV and at the top clay seam for case III and IV. The settlement measured is plotted against the elapsed time from the impact of the shock (Figure 4.6a~c). Figure 4.6a here, depicts the settlement of the surface soil layer for both the shocks in all the parametric cases. It can be seen for both the shocks; the maximum surface settlement is observed when two alternating clay layers are present (Case III). While the minimum settlement is observed in case of top clay layer and bottom layer of NP fines (Case IV). Also, the surface settlement in Case III during both the shocks is gradual as compared to other cases. In Figure 4.6b, the settlement for top seam (clay layer) is given for Case III and IV. Here during Shock 1, the top seam experiences higher settlement in Case IV, while the during the Shock 2, a higher settlement is observed in Case III. This may be due to the different degree of consolidation in the top layer during Shock 1 and 2, as well as delayed expulsion of pore water from the cracks formed in the upper clay layer at a later stage. The settlement for bottom seam is given in Figure 4.6c, here the lower soil layer experiences a delayed settlement in Case II and III. This is due to the water film formed below the lower seam which inhibits the pore water from lower depths to expulse to the top layers, thereby delaying the consolidation of the layer.

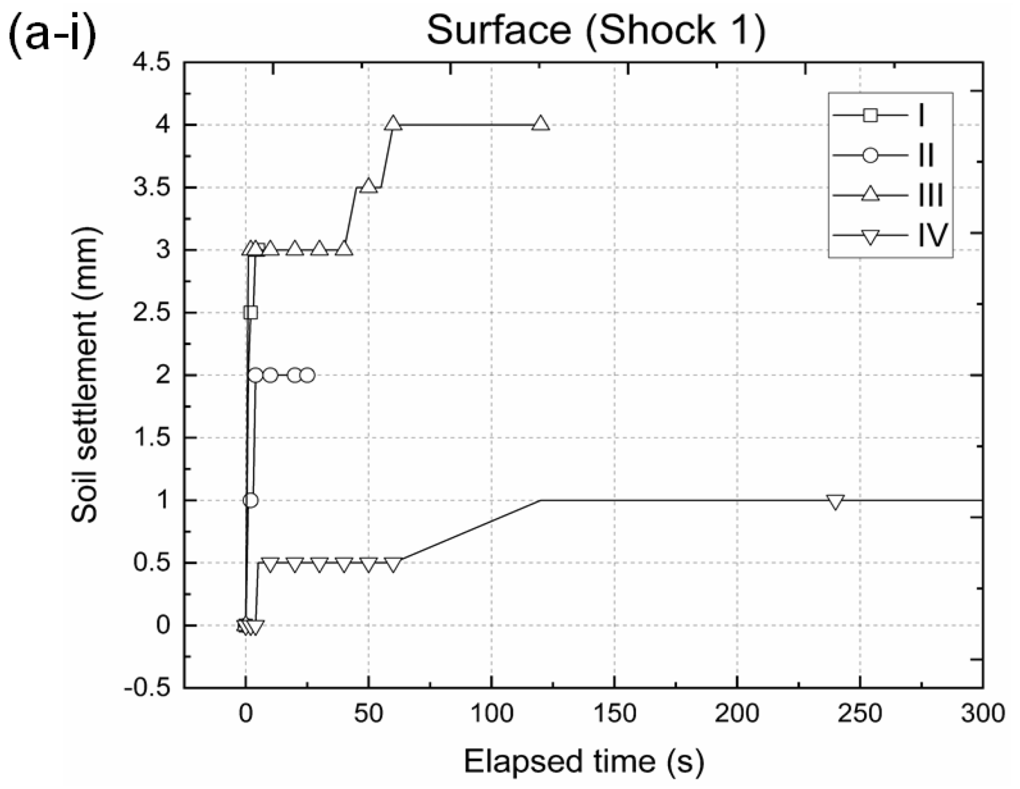
(a-i)
Surface (Shock 1)
Soil settlement (mm)
Elapsed time (s)
4.5
4
3.5
3
2.5
2
1.5
1
0.5
0
-0.5
0
50
100
150
200
250
300
I
II
III
IV

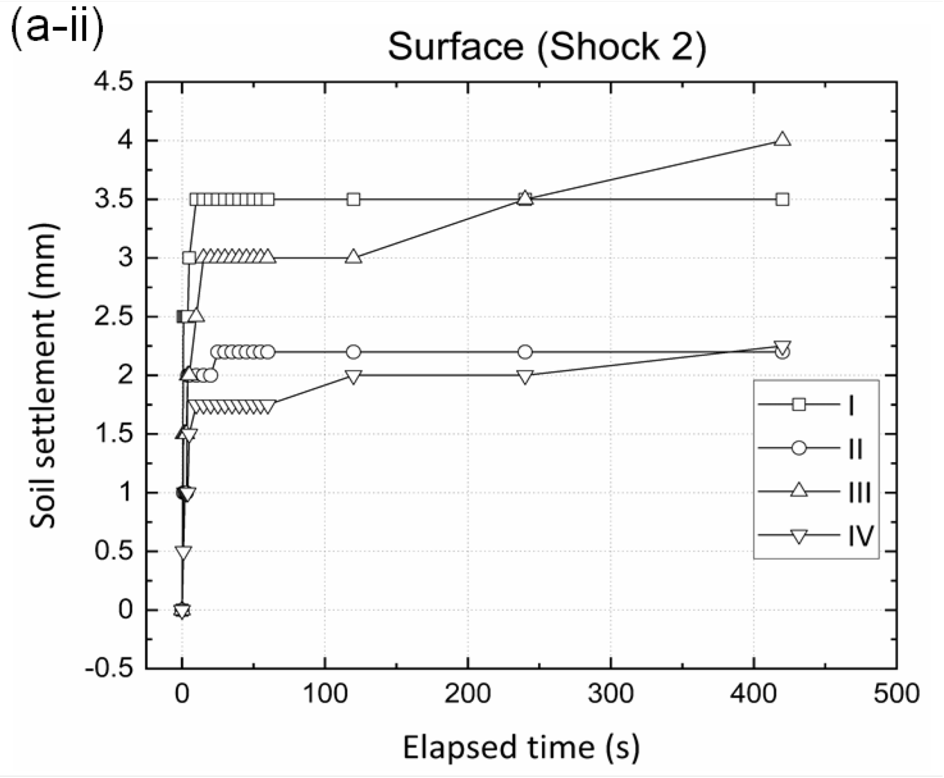
(a-ii)
Surface (Shock 2)
Soil settlement (mm)
Elapsed time (s)
4.5
4
3.5
3
2.5
2
1.5
1
0.5
0
-0.5
0
100
200
300
400
500
I
II
III
IV

(b-i) Top seam (Shock 1)

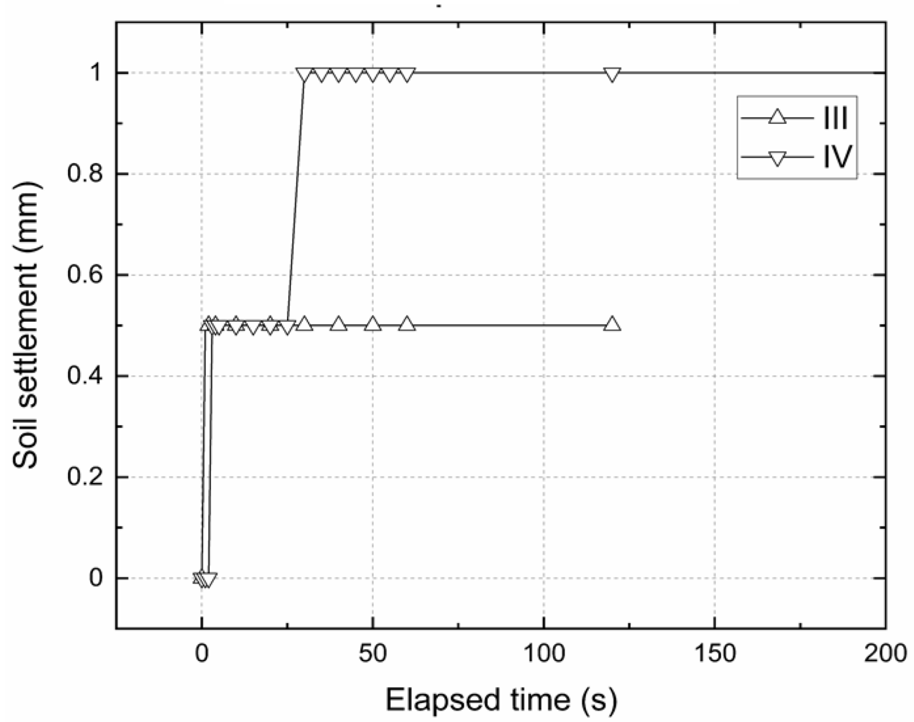

(b-ii) Top seam (Shock 2)

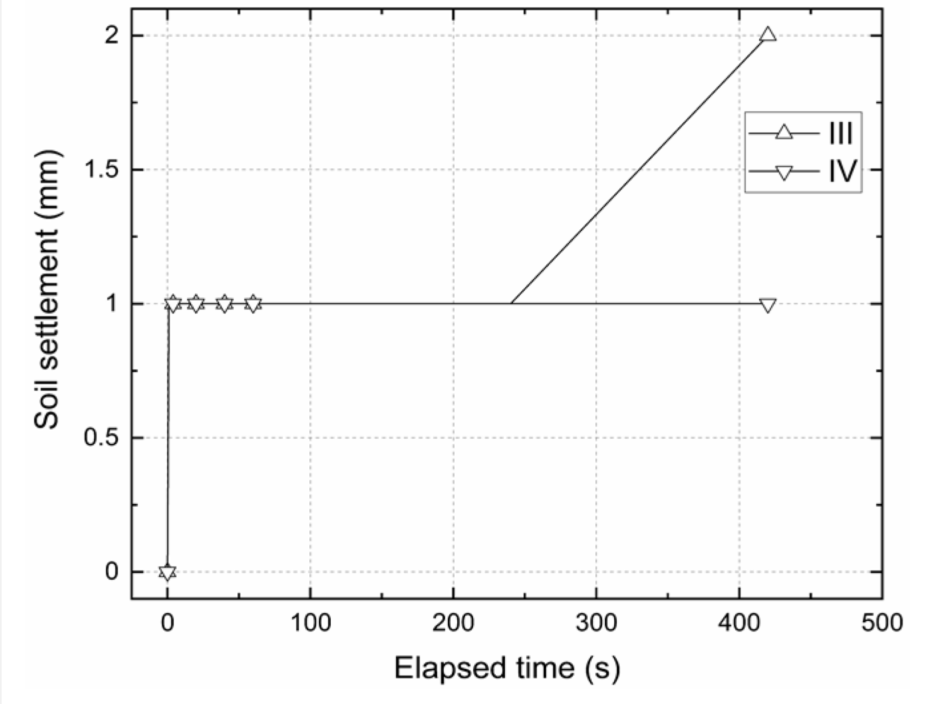

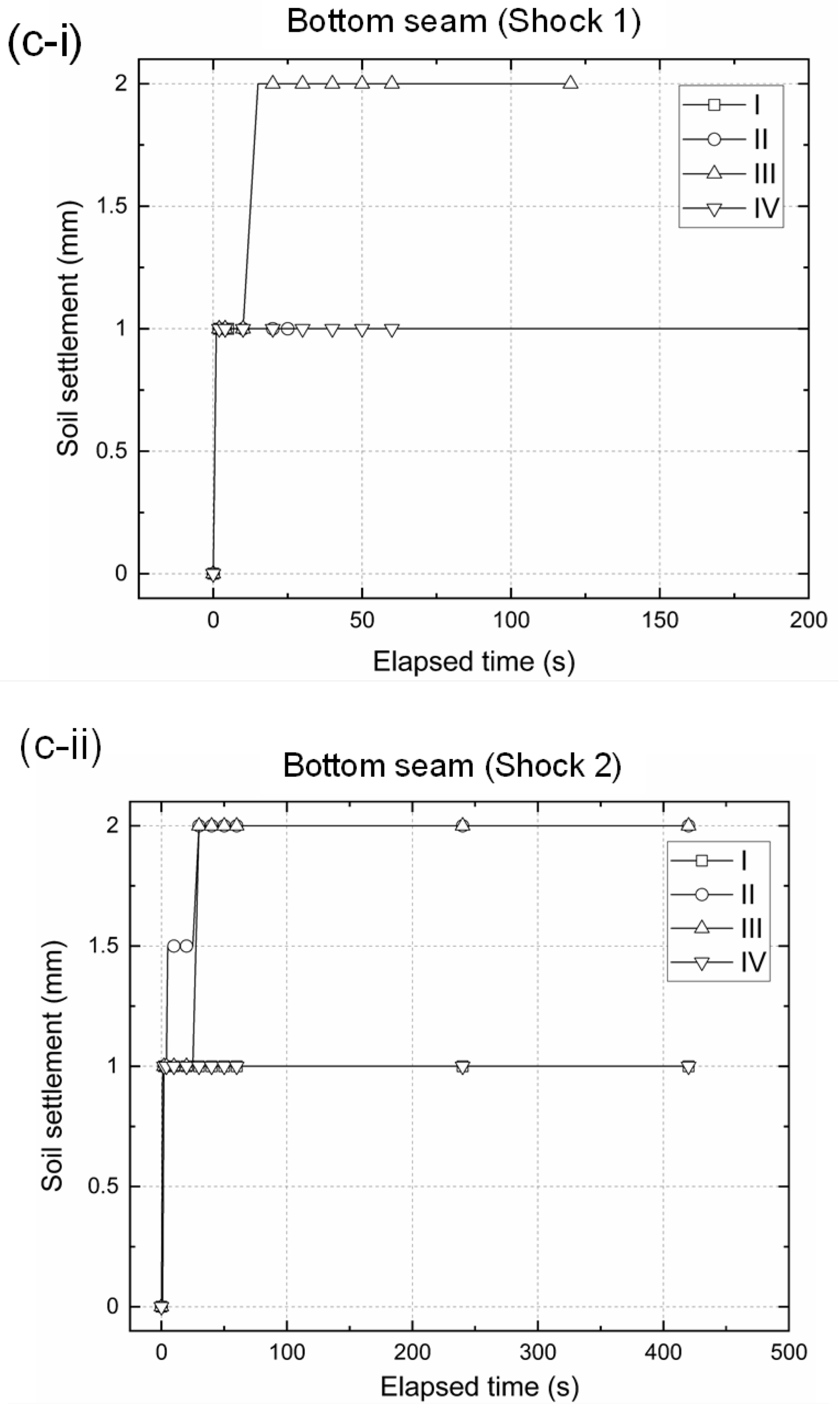

Figure 4.6 Soil settlement with elapsed time: (a-i, a-ii) surface layer; (b-i, b-ii) top seam and (c-i, c-ii) bottom seam.

4.3.4 Development and dissipation of water film

The water film thickness was measured during the formation and dissipation stage by collecting snapshots from the recorded video and measuring the thickness of the water film through an open source software (Neggers, 2020) to millimetre scale. The water film thickness is plotted against elapsed time in Figure 4.7a and b. In Figure 4.7a, the water-film thickness for the top seam is given for all Case III and IV during both the shocks. It can be observed from the figure that, during Shock 1, the water film thickness in Case III sees a gradual increase and then decrease, while in Case IV, there is a sudden decrease in thickness. Also, the maximum thickness of the water film is around 5% of the thickness of the capping layer. For Shock 2, the thickness gradually decreases for both Case III and IV. The variation of thickness for bottom seam is depicted in Figure 4.7b. Here, water film thickness is much lower when a single clay layer is present. In case of two clay layers, the water film thickness, dissipated gradually with time. While it is important to note that the water film formation in the lower layer in case of NP fines was not observed during Shock 1, while the water film quickly dissipated during Shock 2.

(a-i)

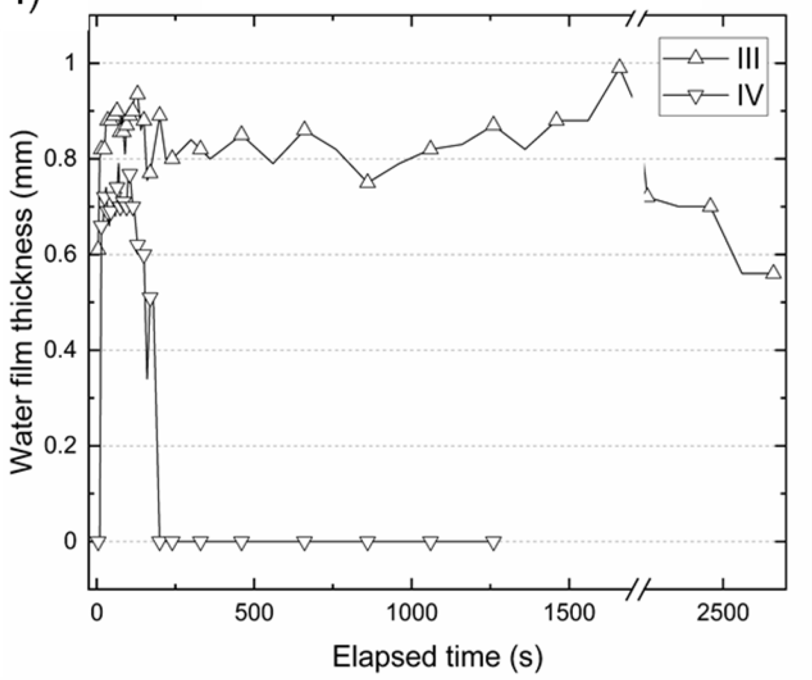
Top seam (Shock 1)

(a-ii)

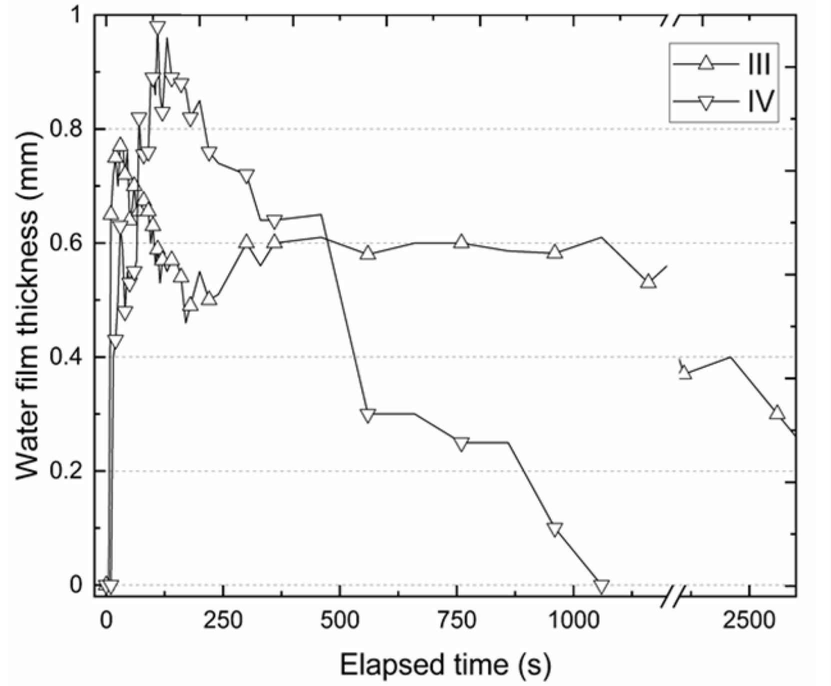
Top seam (Shock 2)

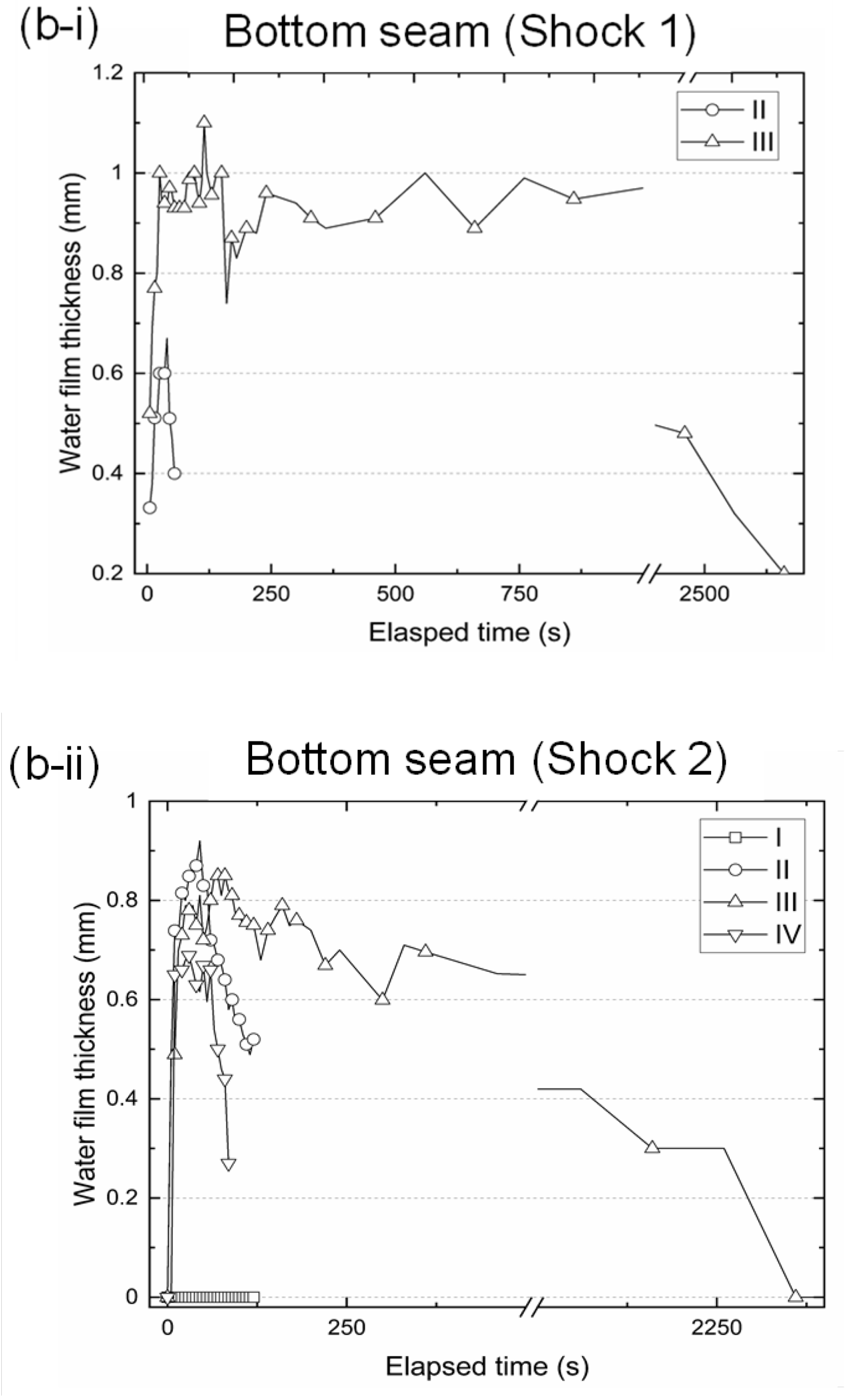

Figure 4.7 Variation in thickness of water film with elapsed time: (a-i, a-ii) top seam and (b-i, b-ii) bottom seam.

The formations of water film for the Cases II, III and IV are shown in Fig. 4.8. Gradient color mode is applied to the images to make the water film more distinctive. Here, for Case II, the development of WF is simple due to presence of single clay seam. For Case III, the water film first develops under lower clay seam with higher thickness as compared to the upper seam, later when the WF below lower seam starts decaying, the thickness of WF below the upper seam increases. Furthermore, in Case IV where the lower seam is of non-plastic fines, the WF film decays very quickly, dissipating the PWP in the lower sand layer and migrating the pore water to the middle sand layer. The migrated pore water results in increase in EPWP in middle layer and thereby increase in WF thickness below the upper clay seam. In brief, the formation of water film inhibits the passage of pore water from lower layers to upper layers and leads to a slow dissipation of PWP resulting in delayed settlement of the overall soil layer.

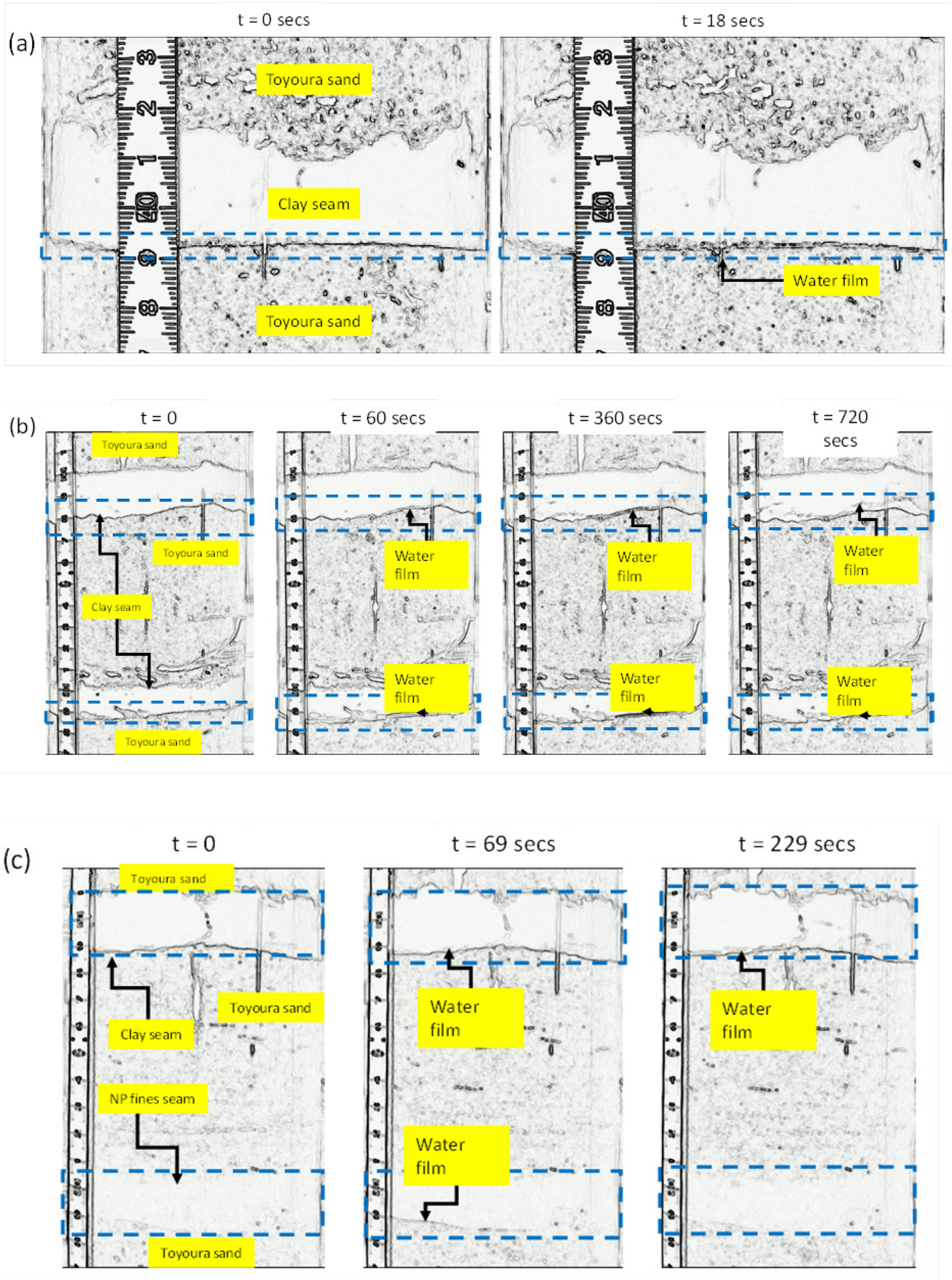

Figure 4.8 Water film development and dissipation under the clay and non-plastic fines seam at different time interval (t): (a) Case II; (b) Case III and (c) Case IV

4.4 CONCLUSIONS

1D soil model tests were conducted to simulate the formation of water film under cap layer which cause the delay in dissipation of pore water pressure, resulting in overall instability and delayed failure in soil layer. The soil model response was measured under single and double cap layer configurations along with cap layer of different plasticity characteristics. Following key inferences can be made from the test results:

- The overlying soil layer practically floats on the water film as the upward force generated by the pore water is able to overcome the overburden stress of the overlying layer. This creates a surface of very low friction between overlying cap layer and the underlying sand layer, this may lead to probable flow failure in field conditions.
- The plasticity of cap layer significantly influences the thickness and the dispersion time of water film. Plastic cap layer can sustain a water film of higher thickness for longer time. This also leads to further delay in dissipation of excess pore water pressure from underlying liquefied layers.
- Plastic cap layers tend to cause larger settlement in overall soil strata due to higher compressibility.
- A complete liquefaction of the soil strata for formation of water film is not necessary, water film may form even if the underlying soil layer reaches near liquefaction.
- With progressive consolidation of lower layers, the settlement of the overall soil strata occurs sequentially, this if considered in a field condition, may provide multiple sliding interfaces due to multiple cap layers.

The contents of this chapter have been published in or submitted for publication as the following:

Rohit, D., Hazarika, H., Qin, C. J., Maeda, T., Kokusho, T., & Yahiro, Y. (2021). One – dimensional soil column simulation on water film formation during earthquake. In Hazarika, H., Madabhushi, G.S.P., Yasuhara, K. and Bergado D. T. (Ed.), *Advances in Sustainable Construction and Resource Management*, Springer Nature Singapore, 693–703.

Rohit, D., Pasha, S. M. K., Hazarika, H., Kokusho, T., & Nurdin, S. (2021). Influence of Low Permeability Capping Layers on Liquefaction Induced Failure in Stratified Ground. In Patel, S., Solanki, C. H., Reddy, K. R. and Shukla, S. K. (Ed.), *Proceedings of the Indian Geotechnical Conference 2019*, Springer Singapore, 343–355.

Rohit, D., Hazarika, H., Qin, C., Maeda, T., Kokusho, T., Yahiro, Y. Experimental and Numerical Simulation on Water Film Formation During the Earthquake, *Journal of Forensic Engineering*, Proceedings of the Institution of Civil Engineers, UK (Submitted).

REFERENCES

Hazarika, H., Rohit, D., Pasha, S. M. K., Maeda, T., Masyhur, I., Arsyad, A., & Nurdin, S. (2021). Large distance flow-slide at Jono-Oge due to the 2018 Sulawesi Earthquake, Indonesia. *Soils and Foundations*, *61*(1), 239–255.

Kamai, R., Boulanger, R. W., Kano, S., Marinucci, A., Howell, R., Rathje, E., Conlee, C., & Gallagher, P. (2008). Effects of void redistribution on post-earthquake residual strengths for liquefiable soils. *Association of Dam Safety Officials - Dam Safety 2008*.

Kiyota, T., Furuichi, H., Hidayat, R. F., Tada, N., & Nawir, H. (2020). Overview of long-distance flow-slide caused by the 2018 Sulawesi earthquake, Indonesia. *Soils and Foundations*, *60*(3), 722–735.

Kokusho, T. (1999). Water film in liquefied sand and its effect on lateral spread. *Journal of Geotechnical and Geoenvironmental Engineering*, *125*(10), 817–826.

Kokusho, T. (2000). Mechanism for Water Film Generation and Lateral Flow in liquified Sand Layer. *Soils and Foundations*, *40*(5), 99–111.

Kokusho, T. (2003). Current state of research on flow failure considering void redistribution in liquefied deposits. *Soil Dynamics and Earthquake Engineering*, *23*(7), 585–603.

Kokusho, T., & Fujita, K. (2002). Site Investigations for Involvement of Water Films in Lateral Flow in Liquefied Ground. *Journal of Geotechnical and Geoenvironmental Engineering*, *128*(November), 917–925.

Kokusho, T., Hara, T., & Hiraoka, R. (2004). Undrained Shear Strength of Granular Soils with Different Particle Gradations. *Journal of Geotechnical and Geoenvironmental Engineering*, *130*(6), 621–629.

Malvick, E. J., Kutter, B. L., Boulanger, R. W., & Kulasingam, R. (2006). Shear Localization Due to Liquefaction-Induced Void Redistribution in a Layered Infinite Slope. *Journal of Geotechnical and Geoenvironmental Engineering*, *132*(10), 1293–1303.

Mason, H. B., Montgomery, J., Gallant, A. P., Hutabarat, D., Reed, A. N., Wartman, J., Irsyam, M., Simatupang, P. T., Alatas, I. M., Prakoso, W. A., Djarwadi, D., Hanifa, R., Rahardjo, P., Faizal, L., Harnanto, D. S., Kawanda, A., Himawan, A., & Yasin, W. (2021). East Palu Valley flowslides induced by the 2018 MW 7.5 Palu-

Donggala earthquake. *Geomorphology*, *373*. https://doi.org/10.1016/j.geomorph.2020.107482

Neggers, J. (2020). *Jann5s/measuringtool*. https://github.com/Jann5s/measuretool

Okamura, M., Ono, K., Arsyad, A., Minaka, U. S., & Nurdin, S. (2020). Large-scale flowslide in Sibalaya caused by the 2018 Sulawesi earthquake. *Soils and Foundations*, *60*(4), 1050–1063.

Rohit, D., Hazarika, H., Qin, C. J., Maeda, T., Kokusho, T., & Yahiro, Y. (2021). One – dimensional soil column simulation on water film formation during earthquake. In D. T. Hazarika, H., Madabhushi, G.S.P., Yasuhara, K. and Bergado (Ed.), *Advances in Sustainable Construction and Resource Management,* 693–703.

Rohit, D., Pasha, S. M. K., Hazarika, H., Kokusho, T., & Nurdin, S. (2021). *Influence of Low Permeability Capping Layers on Liquefaction Induced Failure in Stratified Ground BT - Proceedings of the Indian Geotechnical Conference 2019* (S. Patel, C. H. Solanki, K. R. Reddy, & S. K. Shukla (eds.)), 343–355. Springer Singapore.

Sun, D. A., Matsuoka, H., & Xu, Y. F. (2004). Collapse behavior of compacted clays in suction-controlled triaxial tests. *Geotechnical Testing Journal*, *27*(4), 362–370.

Yang, Z., & Elgamal, A. (2001). Sand Boils and Liquefaction--Induced Lateral Deformation. *15th International Conference on Soil Mechanics and Geotech. Engg.*, *1989*, 345–350.

CHAPTER 5

NUMERICAL SIMULATION OF SOIL STRATA

5.1 INTRODUCTION

Observations made from past earthquakes imply that lateral failures or spreads have occurred in liquified soils in coastal and river areas in regions like California (USA), Niigata (Japan), and Turkey. The ground displacement ranged up to few meters, that too surprisingly on gentle slopes of less than few degrees (Kokusho, 2003). Furthermore, these slides were observed to have occurred few moments after the ground motion ceased (Hamada, 1992; Kawakami & Asada, 1966). Numerical studies related to the formation of water film below a capped layer have been conducted in past with regards to liquefaction induced lateral spreading in gently sloped ground (El Shamy et al., 2010). It has also been studied that how the trapped pore water under hydraulic gradient tends to form seepage paths to the surface which then creates sand boils at the surface below the capping layer could later result in the formation of sand boils (Yang and Elgamal, 2001). Physical model tests conducted by Kulasingam et al., (2004) have highlighted that, slopes consisting clean sands with low relative densities, D_r, upto 20% may experience large displacements, although they have enough strength to prevent a flowslide. Numerical simulations performed by Yang and Elgamal (2002), on a soil column with three parametric cases. Here in Case 1, the soil column consisted of clean sand throughout; Case 2 had silt interlayer in between clean sand layer, while Case 3 had silt interlayer in between sandy gravel layer. It was observed that, for both the cases where the silt capping layer was present, the soil layers above the capping layer experienced much higher lateral shear strain with a localized shear failure. Also, the excess pore water pressure remained high for the layers below capping layer for a longer duration of time. Kokusho and Kojima(2002) performed sedimentation analysis for water film generation based on the 1D model tests performed by them. It was observed that, for a stable water film to be formed under the cap layer, an excessive hydraulic gradient need to be generated below the cap layer, so that it can push the cap layer up against the overlying coarser layer. It was also highlighted in the study that; water films tend to assist as sliding surfaces and therefore play a key role in seismically induced landslides and submarine slides in liquefied loose sand deposits.

Furthermore, it is important to note that in physical model tests, liquefiable soils are either considered as drained or undrained, although this may not be the case in field stratifications as during and after shaking pore water will permeate from the zones of high pore pressure to low pore pressure (Seid-Karbasi & Byrne, 2007). In this chapter, a dynamic solid-fluid coupled analysis technique is employed to study the forces generated at cap layer interface which lead to flow failures in ground with gentle gradient in liquefiable soil. Scaled soil models similar to the 1D laboratory tests are simulated under the influence of sinusoidal loading along with typical soil lithology from Trench 4.

5.2 CONSTITUVE SOIL MODEL

In order to study the dynamic response of layered soils with single and double capping layers of different permeabilities, a 1D non-linear site response analysis is performed on a soil column using CYCLIC 1D software (Elgamal et al., 2015). In this software the saturated soil system is modelled as a two-phase media based on the Biot's (1962) theory of porous media. A simplified solid-fluid (*u-p)* coupled formulation is adopted to define the finite elements, where the soil skeleton (*u*) and pore pressure (*p*) are primary unknowns (Zienkiewicz et al., 1990). For computation, the following assumptions are made (Chan, 1988):

- The model has small deformations and negligible rotations.
- Densities of the solid and fluid are constant in both time and space.
- Porosity is locally homogeneous and constant with time.
- Soil grains are incompressible.
- Equal accelerations are applied for both solid and fluid phases.

The *u-p* formulation as described by Chan (1988) is established by:

a) An equation of motion for the solid-fluid mixture

$$\nabla.(\boldsymbol{\sigma}' + p\boldsymbol{\delta}) - \rho(\ddot{\mathbf{u}} - g) = \mathbf{0} \ldots\ldots\ldots\ldots.(i)$$

b) An equation of mass conservation for the mixture, incorporating equation of motion for the fluid phase and Darcy's law.

$$\nabla.\dot{\boldsymbol{u}} + \frac{\dot{p}}{Q} + \nabla.\left[\frac{\boldsymbol{k}}{\rho_f g}(\nabla p - \rho_f \ddot{\boldsymbol{u}} + \rho_f \boldsymbol{g})\right] = 0 \ldots\ldots\ldots.(ii)$$

Where, $\boldsymbol{\sigma}'$ = effective stress tensor; p=pore water pressure; $\boldsymbol{\delta}$ = second order identity tensor; ρ= mass density of the mixture; **u=** displacement vector of the solid phase; **g=** gravity acceleration vector; Q= undrained bulk modulus of the mixture; **k**= Darcy's permeability coefficient tensor; ρ_f= fluid mass density; g= absolute value of gravity acceleration; ∇= gradient operator; ∇.= divergence operator and a superposed dot denotes the material time derivative.

On application of spatial discretization and Galerkin approximation equations (*i*) and (*ii*) transform to the following matrix form:

$$\boldsymbol{M\ddot{U}} + \int_{\Omega} \boldsymbol{B}^T \boldsymbol{\sigma' d\Omega} + \boldsymbol{Qp} - \boldsymbol{f}^s = \mathbf{0} \ldots\ldots\ldots..(iii)$$

$$\boldsymbol{Q^T\dot{U}} + \boldsymbol{S\dot{p}} + \boldsymbol{Hp} - \boldsymbol{f^p} = \mathbf{0} \ldots\ldots\ldots..(iv)$$

where, $\boldsymbol{M}$= mass matrix; $\boldsymbol{U}$= displacement vector; $\boldsymbol{B}$= strain-displacement matrix; $\boldsymbol{\sigma'}$= effective stress vector; **Q=** discrete gradient operator coupling the solid and fluid phases; **p**= pore pressure vector; **H**=permeability matrix and **S**= compressibility matrix; $\boldsymbol{f^s}$ and $\boldsymbol{f^p}$ are the vectors for the effects of body forces and the required boundary conditions for the solid and fluid phases respectively.

Furthermore, here $\boldsymbol{M\ddot{U}}$**=** inertia force of solid fluid mixture**;** $\boldsymbol{B^T\sigma' d\Omega}$**=** internal force due to soil skeleton deformation; $\boldsymbol{Qp}$= internal force induced by pore-fluid pressure; $\boldsymbol{Q^T\dot{U}} + \boldsymbol{S\dot{p}}$**=** rates of volume change with time for the soil skeleton and the fluid phase; $\boldsymbol{Hp}$**=** seepage rate of pore fluid.

Equations (*iii*) and (*iv*) are integrated using Newmark's time integration procedure with iterations obtained from modified Newton -Raphson approach (Yang and Elgamal, 2002).

The element used in the formulation is composed of 9 nodes for the solid phase and 4 nodes for the fluid phase, to simplify the calculation with almost incompressible fluid phase (Chan, 1988). The solid nodes have two-degrees of freedom (vertical and horizontal displacement) while the fluid node has single-degree of freedom for pore pressure change. A typical node used in the formulation is shown in Figure 5.1.

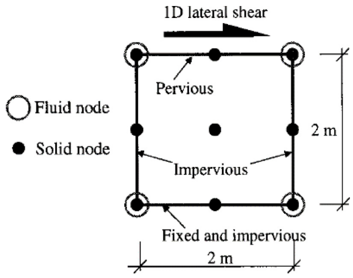

Figure 5.1 A characteristic 9-4 node element used in the *u-p* coupled formulation, with degrees of freedom and bottom and side impervious boundaries (Yang and Elgamal, 2002).

The significance of this constitutive model is that it controls magnitude of cycle-by-cycle permanent shear strain accumulation in clean medium-dense sands. In addition to it, the material elasticity is considered linear and isotropic while plasticity provides non-linearity and anisotropy according to the plasticity convention (Hill, 1950).

5.3 MODEL PARAMETERS FOR SINUSOIDAL LOADING

To perform the simulation in coherence with the experimental model a 1D non-linear site response analysis was performed using CYCLIC 1D software. Here, a uniform soil model of 8 metres in height was considered for the analysis with a rigid bedrock. The ration of numerical model height to the experimental model height was 10:1. Here a total number of 80 rectangular elements were considered with each element of 0.1 m thickness (Figure 5.2). The soil column was inclined at an angle of 2.86° considering a slope of 5% and the water table was assumed to be at ground level. The base input motion of acceleration 0.2g, frequency 3Hz and 15 cycles was provided (Figure 5.3) was used for simplification and a free vibration period of 50 s was considered to record the dissipation of excess pore water pressure. The damping ratio for the soil was assumed to be 5% while the 1st mode and 2nd mode frequencies of were calculated using the shear wave velocity of the soil.

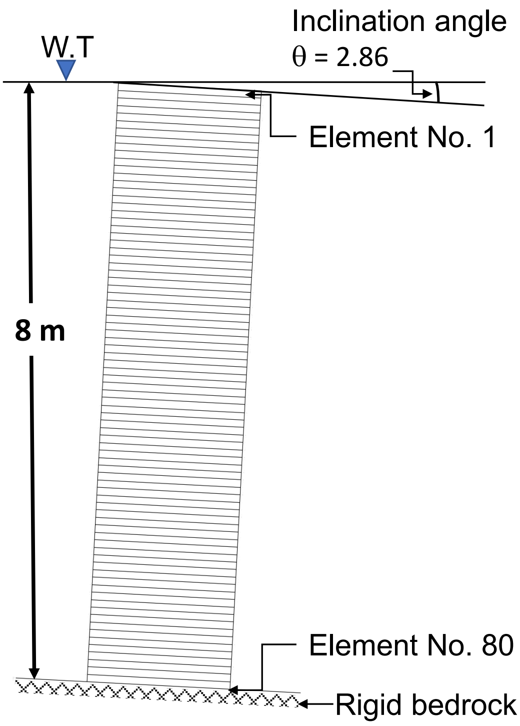

Figure 5.2 Soil column model for 1D site response analysis.

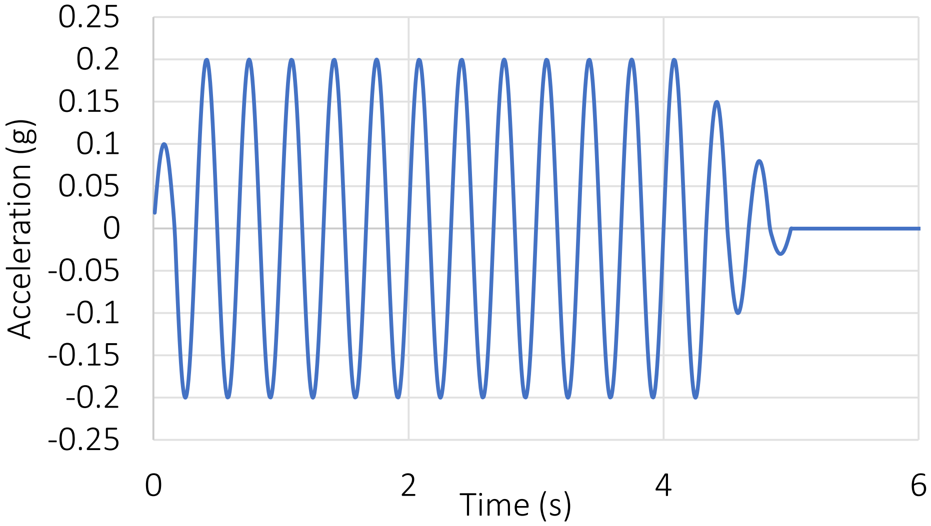

Figure 5.3 0.2g sinusoidal input motion for site response analysis.

5.3.1 Parametric Cases for sinusoidal loading

Here a total of six parametric cases (Case I ~ VI) were considered with varying cap layers configurations. The parametric cases are as follows: Case I: only sand; Case II: sand with clay cap layer; Case III: sand with silt cap layer; Case IV: sand with two clay cap layers; Case V: sand with top clay and bottom silt cap layers and Case VI: sand with top silt and bottom clay cap layers. The details of the parametric models are shown Figure 5.4. The locations of the loose sand, loose silt and soft clay layers are mentioned with the element numbers assigned to them. The properties of the overlying and underlying soil were kept uniform and user defined saturated granular strata with pore-pressure effects were used from the CYCLIC 1D manual for loose sand (Elgamal et al., 2015). The capping layers were assumed as loose silt and cohesive soft clay with permeability property available in the software database. The properties of the soil materials are as given in Table 5.1. The resulting soil response in terms of excess pore water pressure dissipation is recorded at locations A, B, C and D (Figure 5.5).

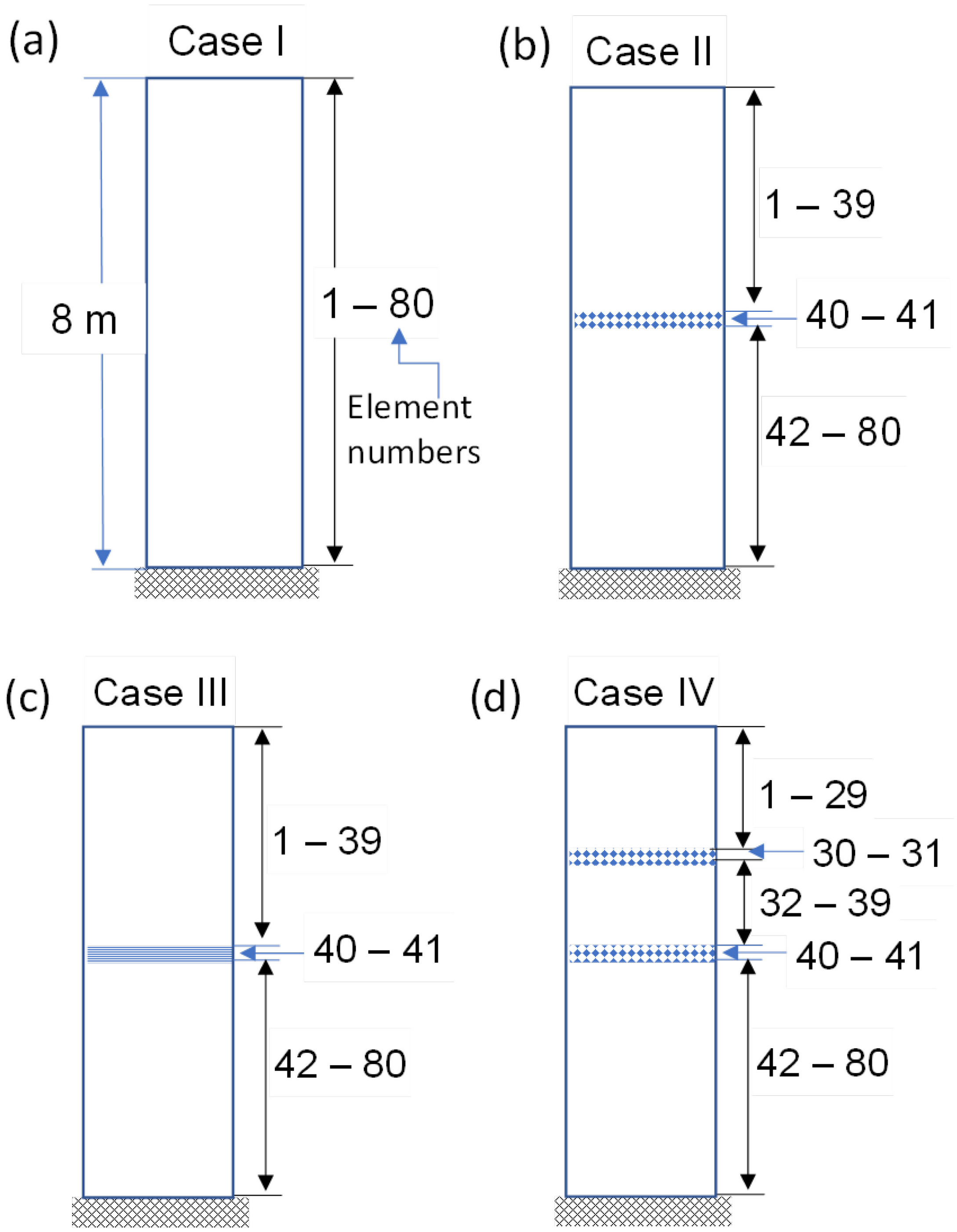
(a)
Case I
8 m
1 – 80
Element numbers
(b)
Case II
1 – 39
40 – 41
42 – 80
(c)
Case III
1 – 39
40 – 41
42 – 80
(d)
Case IV
1 – 29
30 – 31
32 – 39
40 – 41
42 – 80

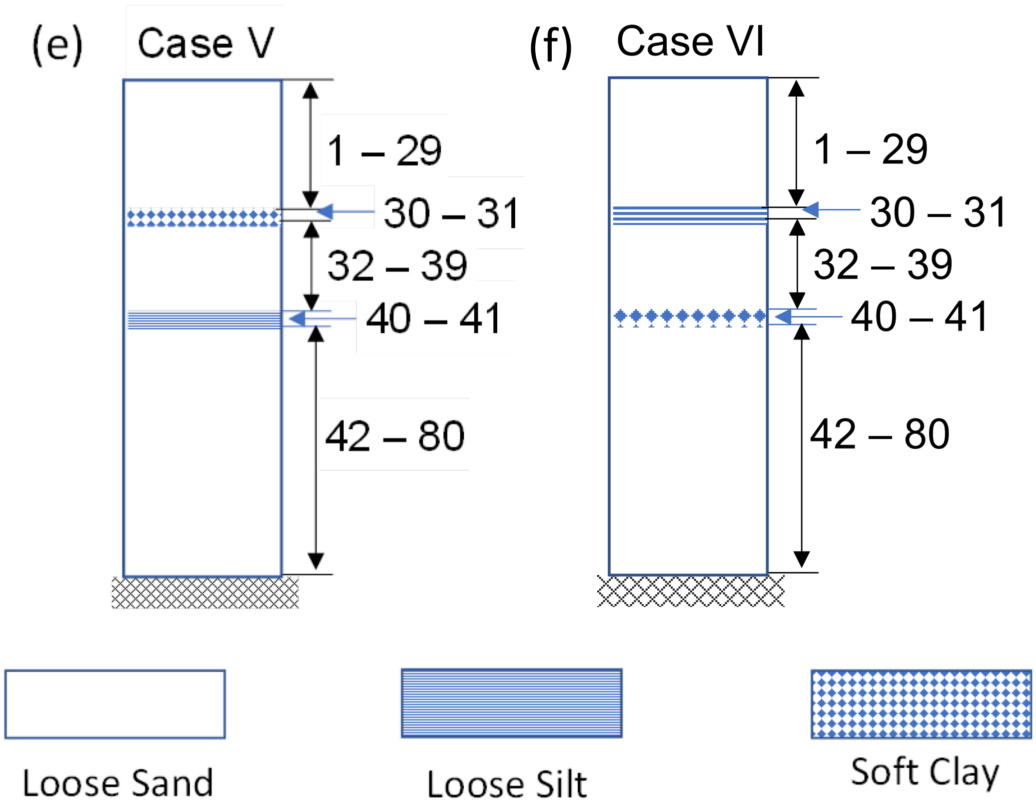

Figure 5.4 Parametric soil models used in site response analysis with assigned soil properties and element numbers: (a) Case I, (b) Case II, (c) Case III; (d) Case IV, (e) Case and (f) Case VI.

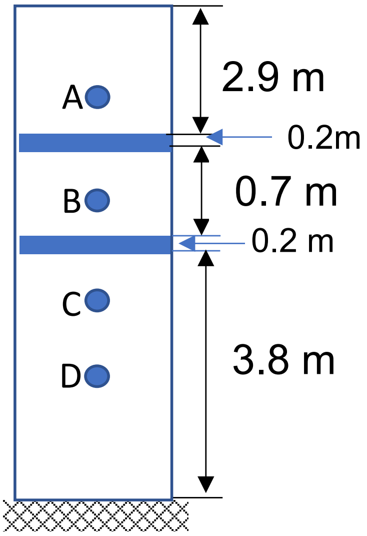

Figure 5.5 Locations for measuring excess pore water pressure development and dissipation.

Table 5.1 Input soil properties for parametric analysis

Soil type **Property**	**Loose sand**	**Loose silt**	**Soft clay**	**Loose gravel**	**Dense gravel**
Mass density, ρ (kg/m^3)	1700	1700	1300	1700	2100
$V_{s\ ref}$ (m/s)	185	185	100	185	255
p' ref (kPa)	80	80	50	80	80
coeff	0.5	0.5	0	0.5	0.5
Vertical confinement ratio, K_o	0.67	0.67	0.67	0.67	0.67
Cohesion, c (kPa)	0.3	0.3	18	0.3	0.3
Friction angle, φ (°)	29	29		29	40
Peak shear strain, γ_{max} (%)	5	5	5	5	5
Number of yield surfaces, NYS	20	20	20	20	20
Phase transformation angle (°)	30	30		30	22
Contraction parameter, c1	0.3	0.3		0.3	0.01
Contraction parameter, c2	0.2	0.2		0.2	0.6
Dilation parameter, d1	0	0		0	0.6
Dilation parameter, d2	10	10		10	10
Liquefaction parameter, l	0.025	0.025		0.025	0.003
Permeability coefficient, k (m/s)	6.6 x	1×10^{-7}	1×10^{-9}	1×10^{-2}	1×10^{-2}

5.3.2 Results and discussions

The excess pore water pressure (EPWP) development and dissipation at four key locations is compared for all the cases, in order to validate the soil numerical soil behaviour. Although, it is not possible to visually simulate the formation of water film, the effect of void redistribution is presented through the effective confinement stress and maximum shear stress across the soil profile.

Excess pore water pressure with respect to depth

The trend of EPWP development and dissipation is presented for all the parametric cases at locations A, B, C and D (Figure 5.6a~d). As observed from Figure 5.6a, the EPWP quickly dissipates for all the soil stratification conditions except for Case I as due to the absence of cap layers, all the pore water rushes towards the surface and causes an increased EPWP. It is to be noted that for Case VI, a significantly low magnitude of the EPWP is observed near the surface, which might be due to the complete failure and sliding of the lower layer. For point B (Figure 5.6b), the EPWP dissipates quickly for Case II and III as the cap layers are below this depth, while for Cases IV, V and Vi, it observes a delayed dissipation. Once again as the peak EPWP is significantly less for Case VI.

For location C (Figure 5.6c), which is below the cap layer in all the cases except Case I, the cap effect of the low permeable layer is clearly visible with significant influence on the delay in EPWP. Furthermore, as we go deeper to location D (Figure5.6d), the dissipation is quicker as compared to the location C, as most of the pore fluid gets accumulated underneath the cap layer. Here the maximum magnitude of EPWP for Case VI is comparable to other cases.

(a)

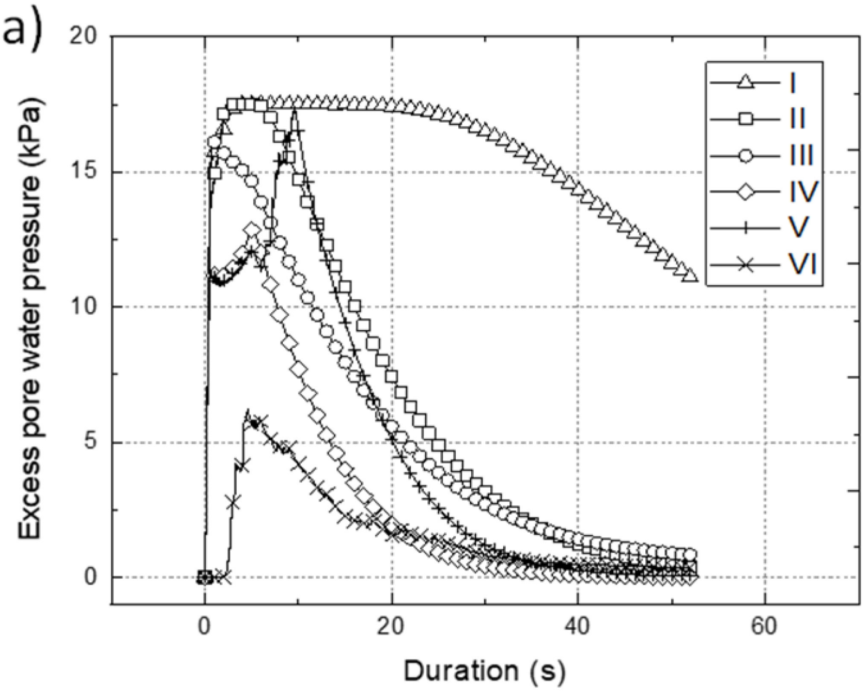
Excess pore water pressure (kPa)
Duration (s)
0
5
10
15
20
-0
20
40
60
I
II
III
IV
V
VI

(b)

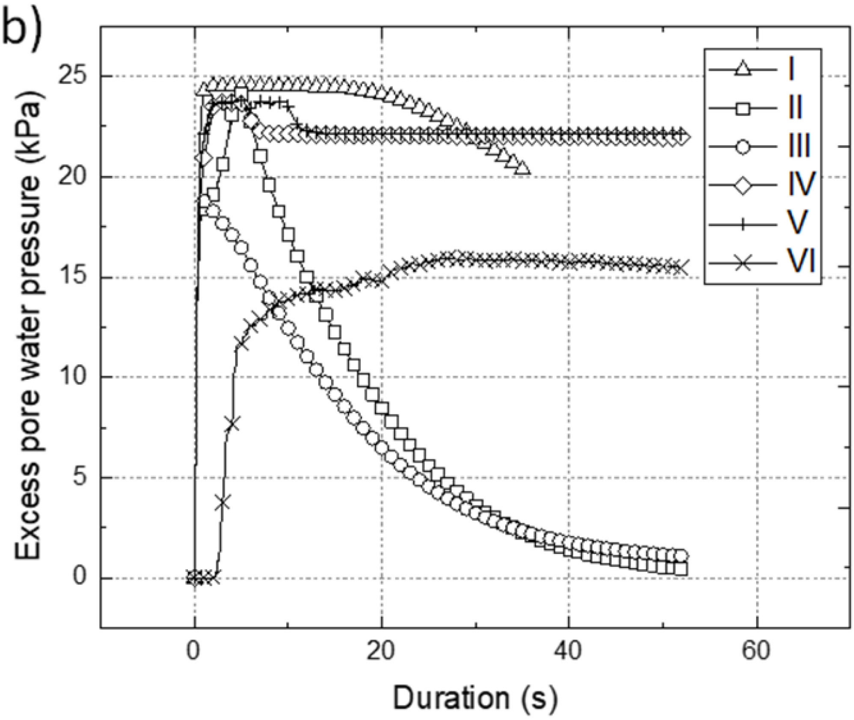
Excess pore water pressure (kPa)
Duration (s)
0
5
10
15
20
25
0
20
40
60
I
II
III
IV
V
VI

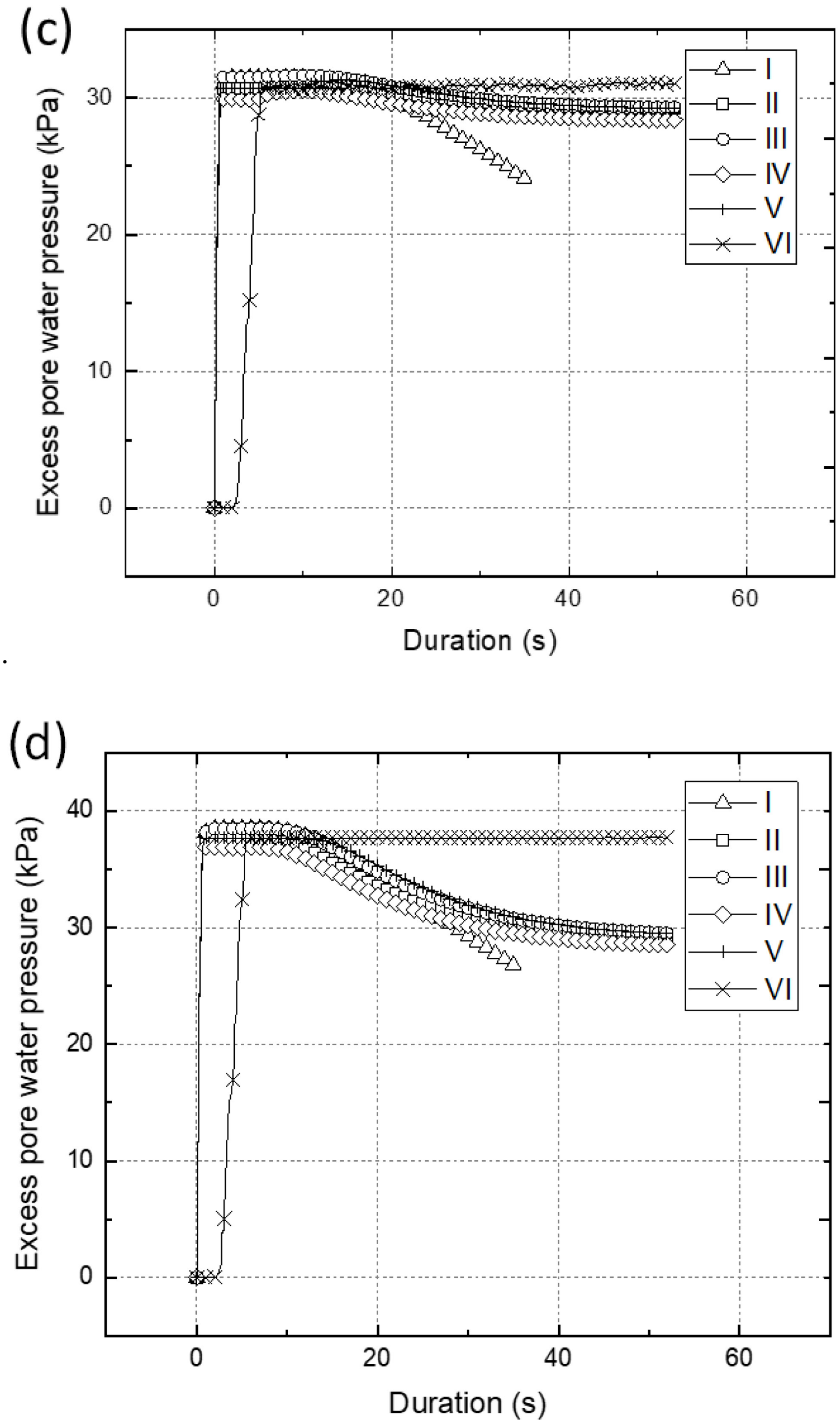

Figure 5.6 Trend of excess pore water pressure build-up and dissipation for all the parametric cases at depths from surface: (a) A (2.5m), (b) B (3.5m), (c) C (4.5m) and (d) D (5.5m).

Effective confinement stress and maximum shear strain

The presence of cap layers has a significant influence on the confining stress in soil along with the shear strain. At very low confining stresses the soil tends to fail under dilation with high shear strain. Figure 5.7a shows the maximum confining stress profile of the soil strata while Figure 5.7b shows the maximum shear strain profile. Here in the figures CL1 and CL2 denotes the location of cap layers in the soil strata. It can be observed that due to possible void redistribution and formation of water film at the cap layer interface, a zone of very low confining stress and high shear strain is developed due to presence of a non-contact surface. This zone may act as a probable sliding plane for the flowslide to occur. Furthermore, for Case VI, the confining stress does not increase even below the lower cap layer (CL2), which is due to the complete dilation of the underlying sand layer.

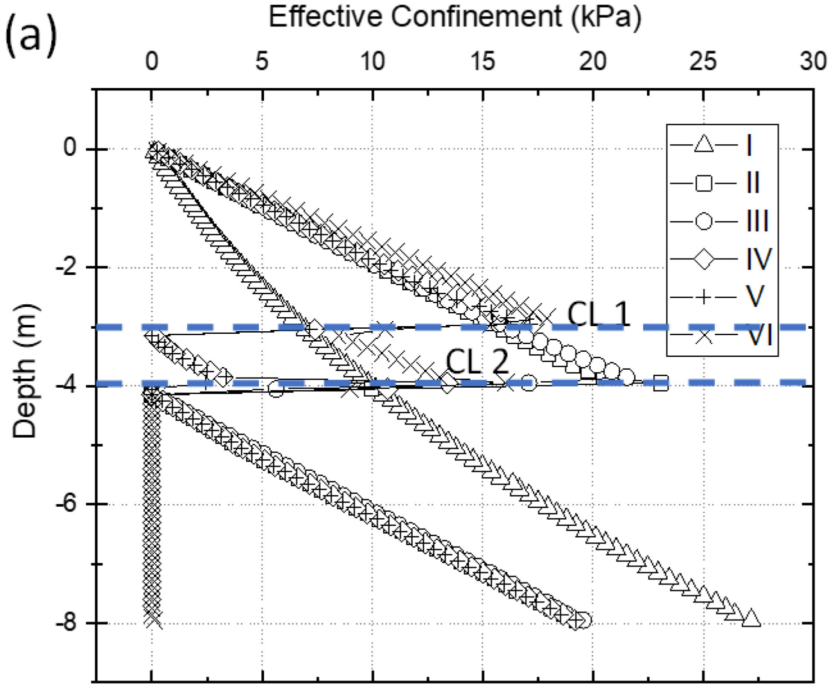

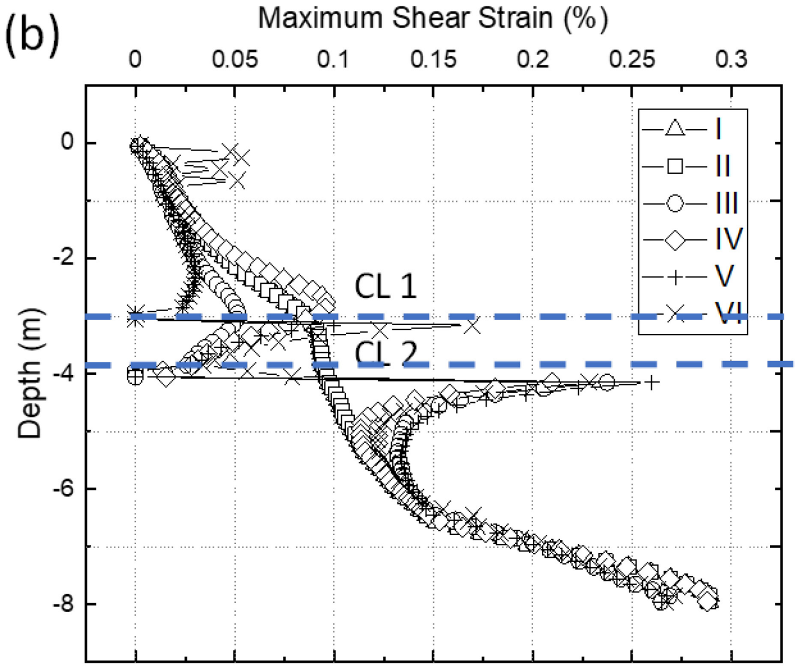

Figure 5.7 Dynamic response of soil profile under the influence of cap layer: (a) effective confinement stress vs depth and (b) maximum shear strain vs depth.

5.4 1D SITE RESPONSE OF ACTUAL SOIL PROFILE.

Considering the limitations of sinusoidal input motions and the complexities of actual site heterogeneities, a typical soil profile from Trench 4 in Sibalaya was considered and 1D site response analysis was performed under the influence of actual earthquake motion. The site response analysis was performed in OpenSeesPL, a graphical user interface (GUI) for three dimensional (3D) site response analysis (Lu et al., 2011). OpenSeesPL uses the same formulation as CYCLIC 1D but in a 3D environment and models the soil column as a shear beam. It also allows the user to provide input motion in all three directions as against one directional input motion in CYCLIC 1D.

The soil strata in this case is modelled as a multi-layered soil column and the classification is simplified as against the field classification or soil type since the laboratory properties of the in-situ material is not yet available to provide user defined material properties. The soil layer is classified according to the dominating soil type for simplification and dense gravel is provided at the base above the hard rock boundary material (Figure 5.8). The soil properties are selected from the in-house library of the software and are similar to the ones provided for CYCLIC 1D (see Table 5.1). Input motion of Palu NS (Figure 5.9) is provided with an amplitude scale factor of 0.5 considering the difference in depth of actual data recording and site amplification. The duration of motion is trimmed to remove the noise and shorten the simulation time. The ground surface in the soil model is inclined at an angle of 1.43° or 2.5% slope.

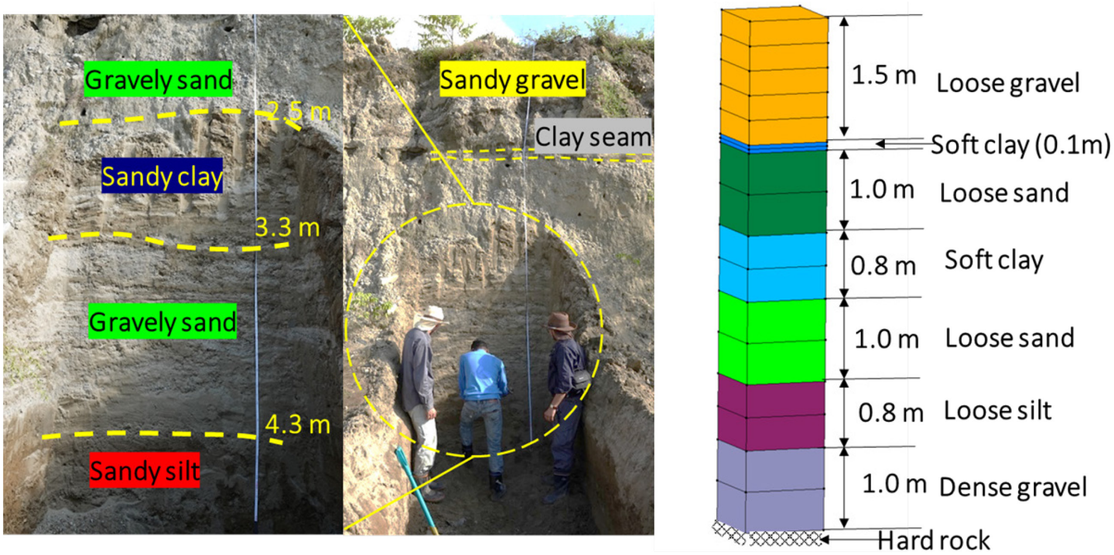

Figure 5.8 Simplified soil profile considered for the site response from Trench 4 in Sibalaya.

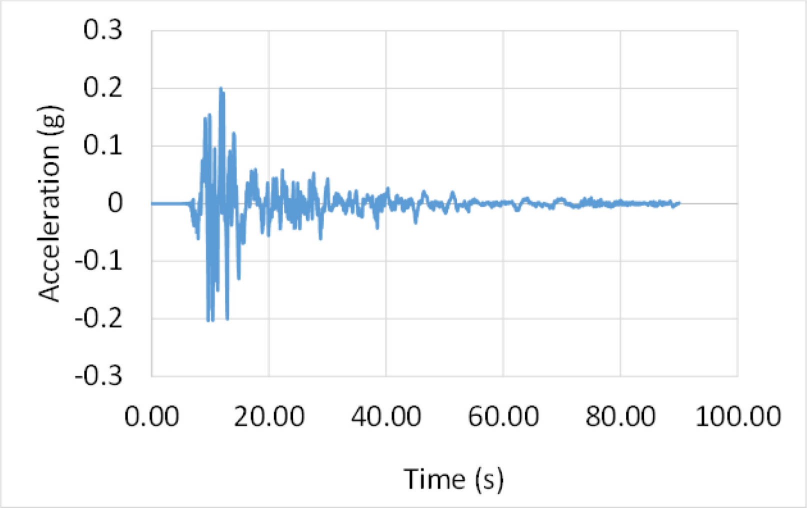

Figure 5.9 Palu NS input motion used for site response analysis of soil profile from Trench 4 in Sibalaya (data source JICA, 2018).

5.4.1 Results of site response for Trench 4 soil profile

The dynamic response of in-situ soil profile from Trench 4 is evaluated under the influence of Palu NS strong motion time history. The factors such as fluid pressure in the soil layers, soil displacement, and cyclic stress-strain behaviour in each layer were examined.

Maximum excess pore water pressure and excess pore water pressure ratio profile

The site heterogeneity tends of have a significant influence on the dynamic response of the soil profile and its stability. Here in Figure 5.10 a and b, the maximum EPWP (Δ u_{max}) and the excess pore pressure ratio (r_u) have been plotted against the elevation of soil strata respectively. Due to varying soil characteristics like, permeability and cohesion, both the profiles are non-linear, with a sharp peak observed in the Δ u_{max} at the silt layer (Figure 5.9a). While the r_u value implies that, the sand and silt layers were liquefied, although, no liquefaction is observed in the clay layer above the sand layer (Figure 5.9b).

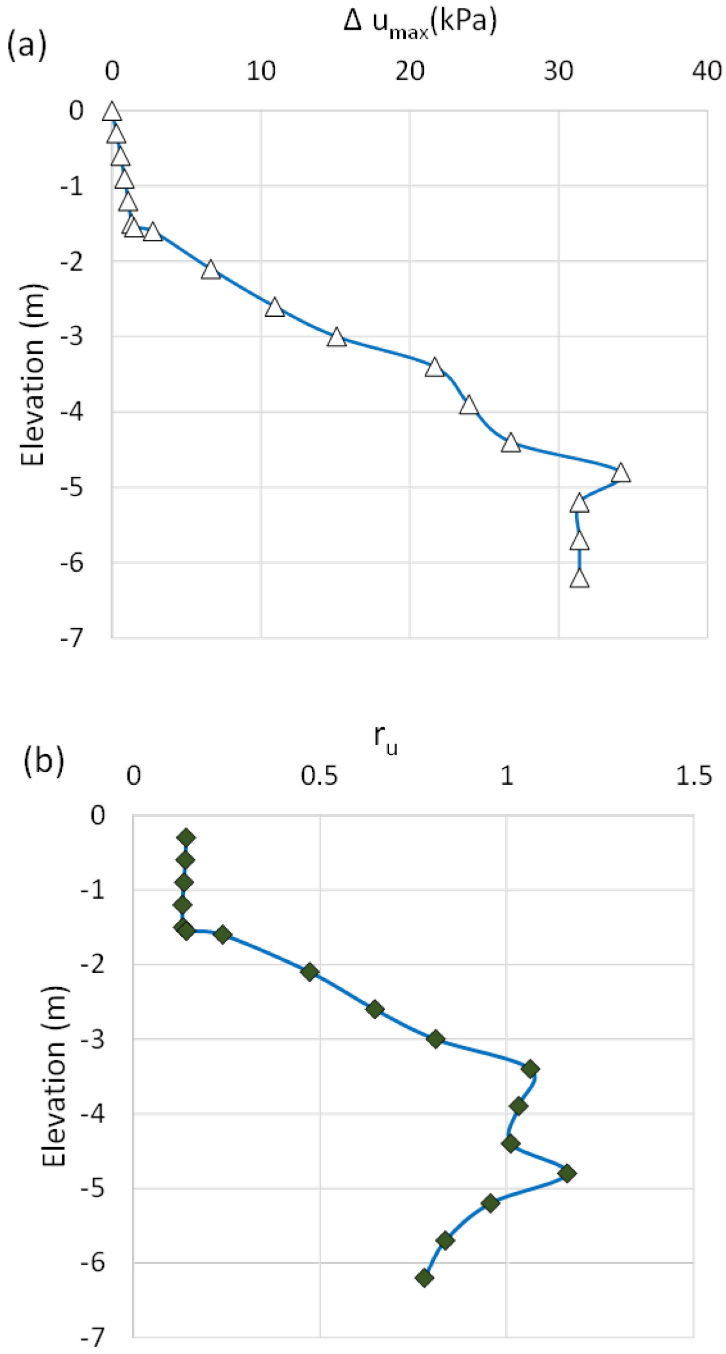

Figure 5.10: Effect of soil heterogeneity on pore water migration during seismic motion: (a) maximum excess pore water pressure and (b) excess pore water pressure ratio vs elevation.

Fluid pressure in each layer

Figure 5.11a~g here shows the EPWP and accelerations in each layer during the ground motion. The fluid pressure and acceleration time history for each layer is depicted as: (a) 1.35m (Gravel), (b) 1.525 m (Clay), (c) 2.35m (Sand), (d) 3.2m (Clay), (e) 4.15m (Sand) and (f) 5.00m (Silt). The EPWP are plotted with the acceleration time history recorded at those locations to study the relationship between excess pore water variation and the ground motion. It could be observed that, in all the layers, the peak acceleration is observed in the negative direction, moreover except for the surface gravel layer, all the underlying soil layers experience the peak EPWP post the peak acceleration.

Furthermore, the EPWP builds-up and dissipates with the ground motion in the top layer (Figure 5.11a), which is otherwise not observed in the layers below (Figure 5.11b~f). To be noted, with increasing depth, the magnitude and dissipation time for the EPWP also increases for lower layers. For the sand and silt layer below the clay layer at 3.4 m depth, the EPWP does not reach peak even after a major part of the strong ground motion has passed and keeps on developing for a longer duration. This is also due to the presence of a thicker clay layer above the sand and silt layers, which inhibits the quick dissipation of excess pore water pressure. The quicker dissipation in the upper clay layer at 1.6m depth is also due to the low thickness of the layer, which might have been not enough to stand the upward hydraulic gradient of the pore water. Furthermore, in all the layers, site amplification is observed, which is due to the presence of soft sandy strata.

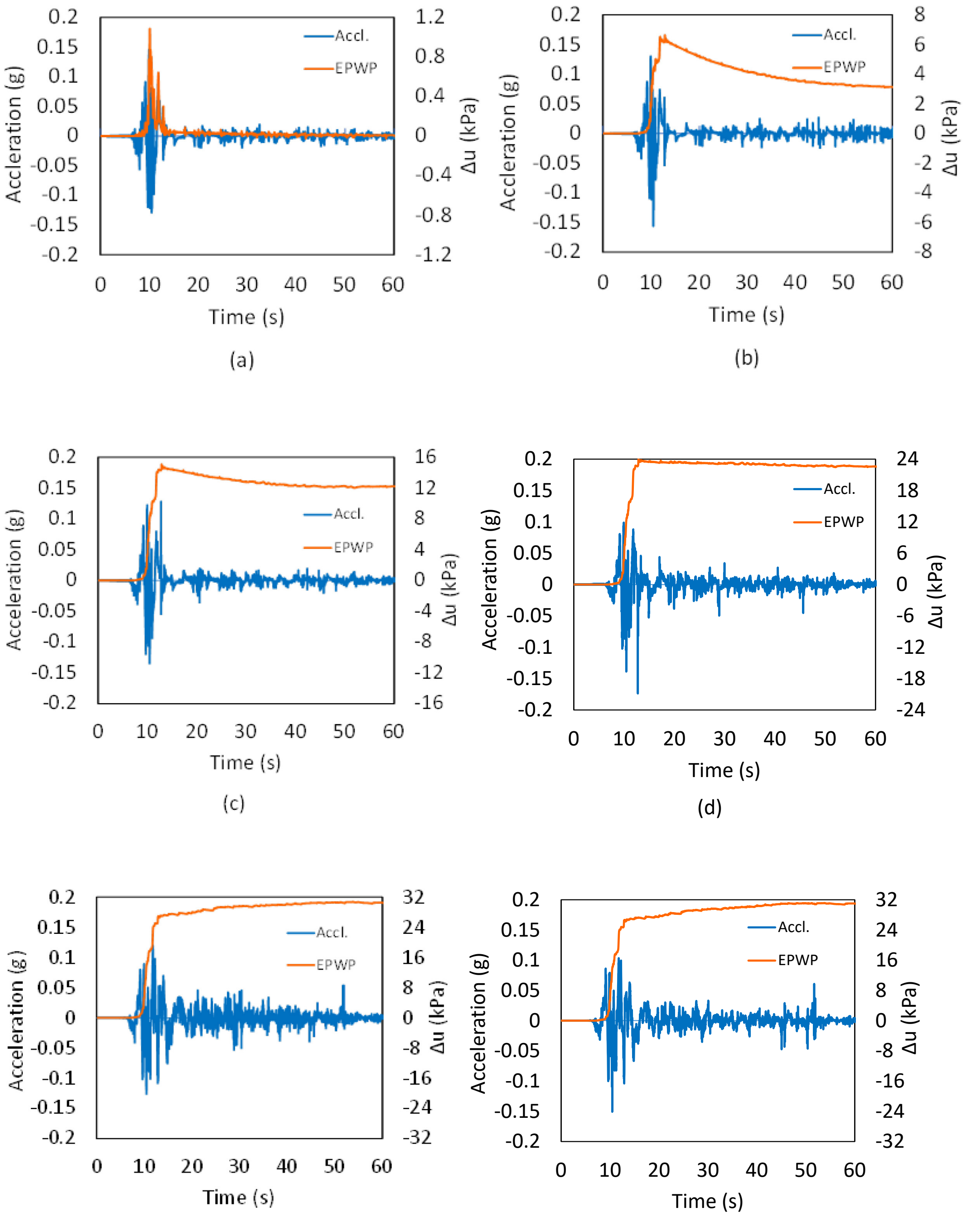

(a) (b) (c) (d) (e) (f)

Figure 5.11 Excess pore pressures/accelerations in each layer: (a) 1.35m, (b) 1.525m, (c) 2.35m, (d) 3.2m, (e) 4.15m and (f) 5.0m.

Effect of cap layers on stress-strain behaviour

In this section, the effect of soil heterogeneity on the stress-strain behaviour of soil profile is discussed with respect to the dynamic response of the soil layers at different depths. From the site response analysis, the stress (τ) vs shear strain (γ) hysteresis trend is obtained at different depths representing the soil profile at that depth. Figure 5.12a~g here depicts the shear stress-strain curve from (a) 1.35m (Gravel), (b) 1.525 m (Clay), (c) 2.35m (Sand), (d) 3.2m (Clay), (e) 4.15m (Sand), (f) 5.00m (Silt) and (g) 5.25m (Gravel). The top layers of loose gravel and sand show a slightly dilative behaviour with increasing number of cycles (Figure 5.12a and c), while the clay layers in Figure 5.12b and d do not show any dilation. The loose sand and the silt layers underneath the thick clay layer from 3.4m depth experience complete loose of strength and undergo liquefaction. Here the sand layer fails in dilation (Figure 5.12e) while the silt layer fails in compression (Figure 5.12f). Furthermore, the gravel layer also loses complete strength after initial cycles (Figure 5.12g).

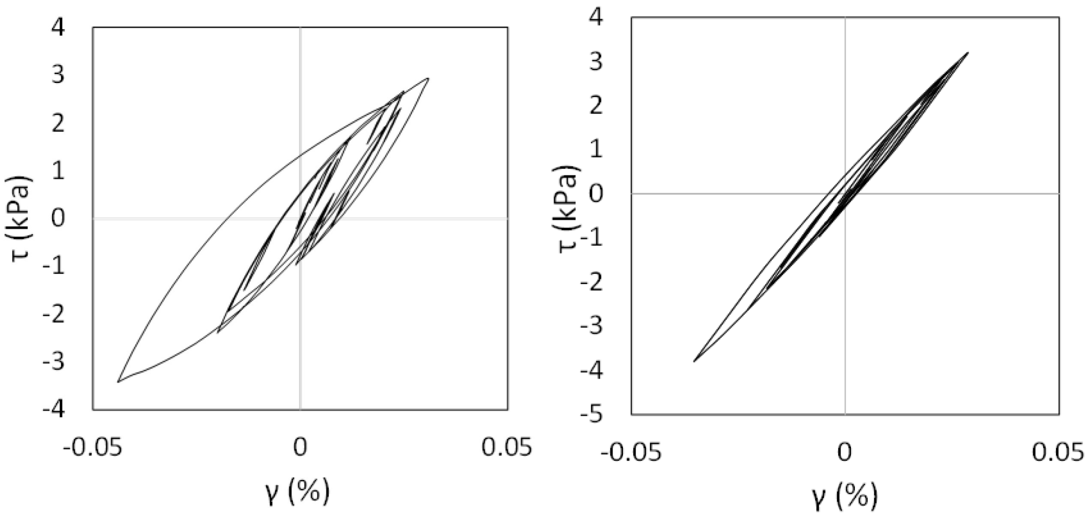

(a)

(b)

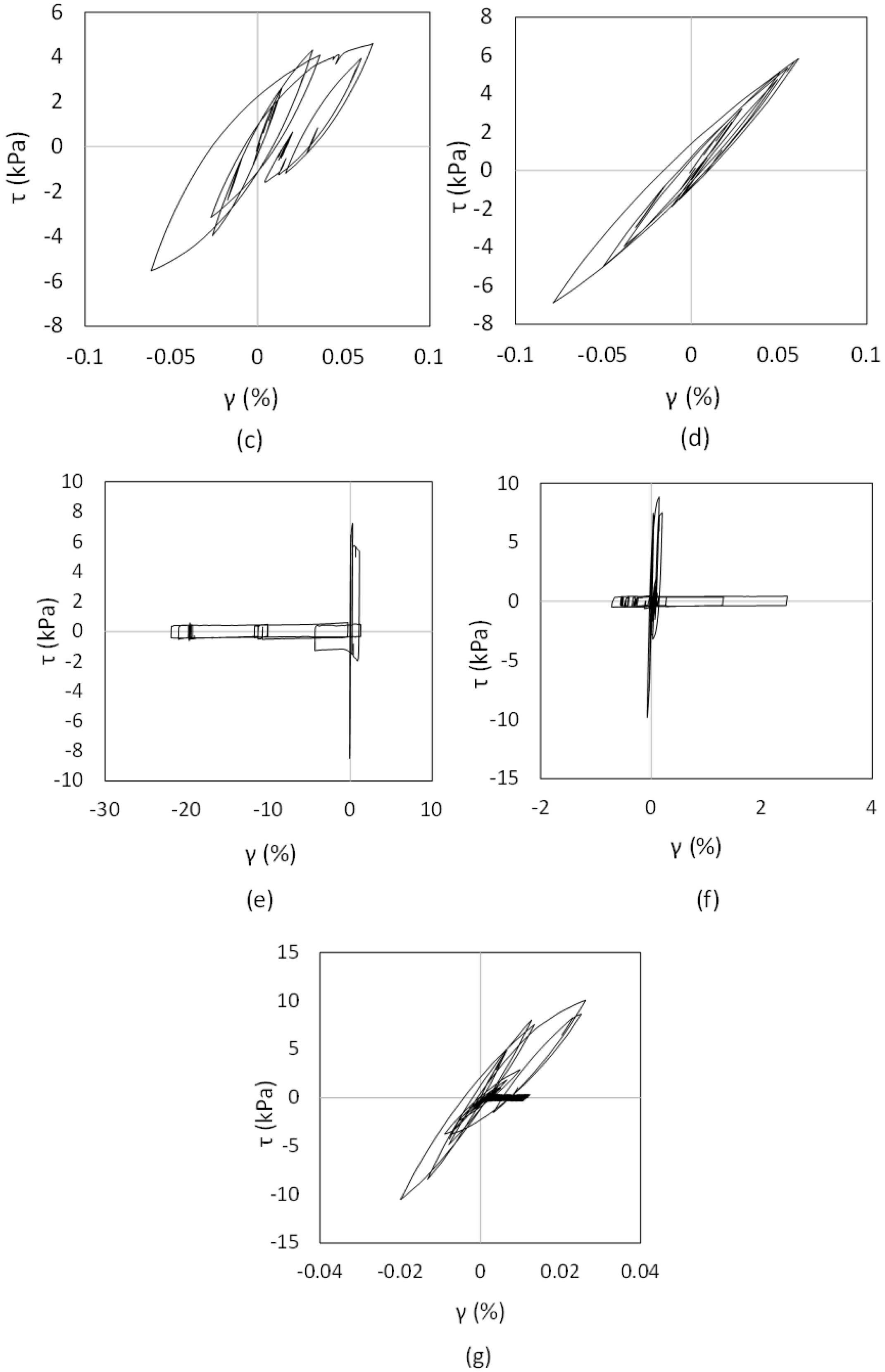

Figure 5.12 Effect of soil heterogeneity on stress-strain behaviour of the soil at different depths: (a) 1.35m, (b) 1.525m, (c) 2.35m, (d) 3.2m, (e) 4.15m, (f) 5.0m and (g) 5.45m.

Effect of cap layer on soil deformation behaviour

This section discusses the displacement in the soil profile under the influence of earthquake motion and presence of cap layers. The soil displacement and acceleration time histories for individual layers is given in Figures 5.13a~f. It can be observed from the figures that significant displacement in the soil layers initiates after the peak ground acceleration has passed, also the displacement continues after the strong ground motion has passed. The overall displacement of soil layers from the surface to 3.4 m or upto thick clay layer is uniform (Figure 5.13a~d), while the sand layer below 3.4 m depth shows significantly less displacement from the overlying layers (Figure 5.13e). Furthermore, the silt layer below the sand layer depicts a displacement in opposite direction although the magnitude is comparably very small (Figure 5.13f). The overall displacement profiles in longitudinal (x) and vertical (z) direction are shown in Figure 5.14a and b respectively. The difference in before and after profiles clearly depict the high longitudinal displacement at the sand layer (Figure 5.14a), which implies that sand layer acts as a sliding plane. Furthermore, for vertical displacement too the sand layer experiences higher displacement across the whole soil profile (Figure 5.14b)

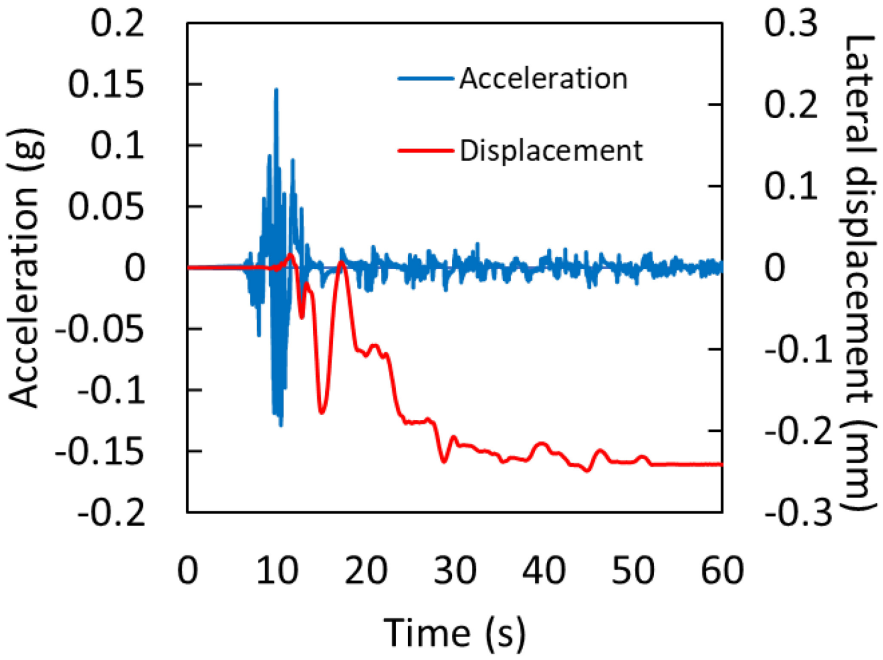
0.2
0.15
0.1
0.05
0
-0.05
-0.1
-0.15
-0.2
Acceleration (g)
0.3
0.2
0.1
0
-0.1
-0.2
-0.3
Lateral displacement (mm)
Acceleration
Displacement
0
10
20
30
40
50
60
Time (s)

(a)

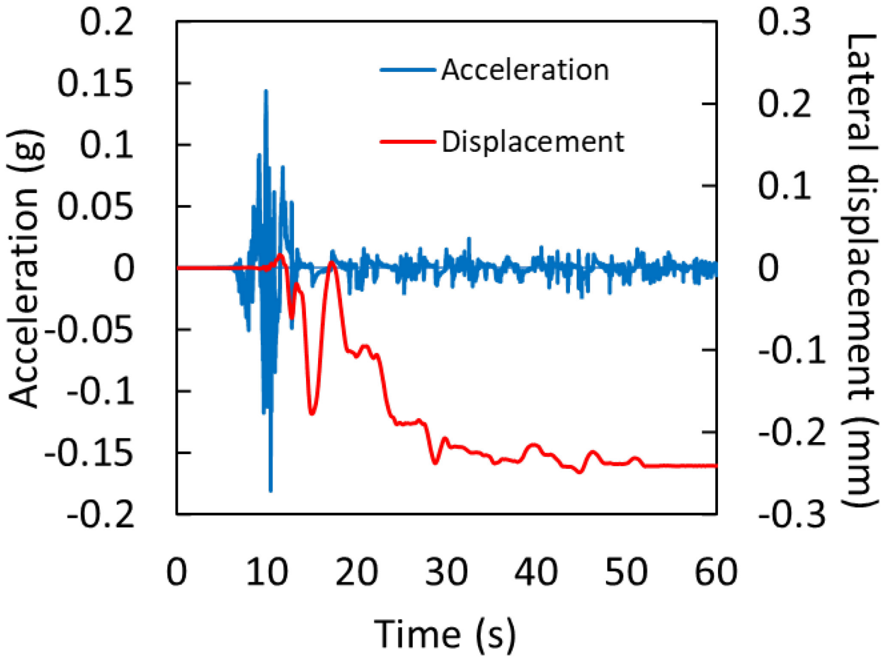
0.2
0.15
0.1
0.05
0
-0.05
-0.1
-0.15
-0.2
Acceleration (g)
0.3
0.2
0.1
0
-0.1
-0.2
-0.3
Lateral displacement (mm)
Acceleration
Displacement
0
10
20
30
40
50
60
Time (s)

(b)

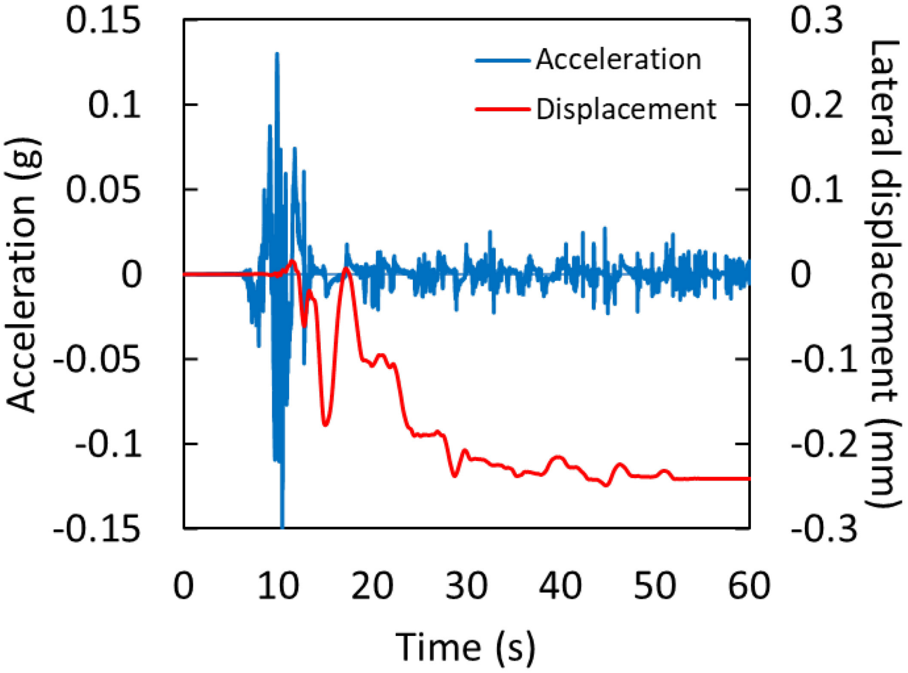

0.15
0.1
0.05
0
-0.05
-0.1
-0.15
Acceleration (g)
0.3
0.2
0.1
0
-0.1
-0.2
-0.3
Lateral displacement (mm)
Acceleration
Displacement
0
10
20
30
40
50
60
Time (s)

(c)

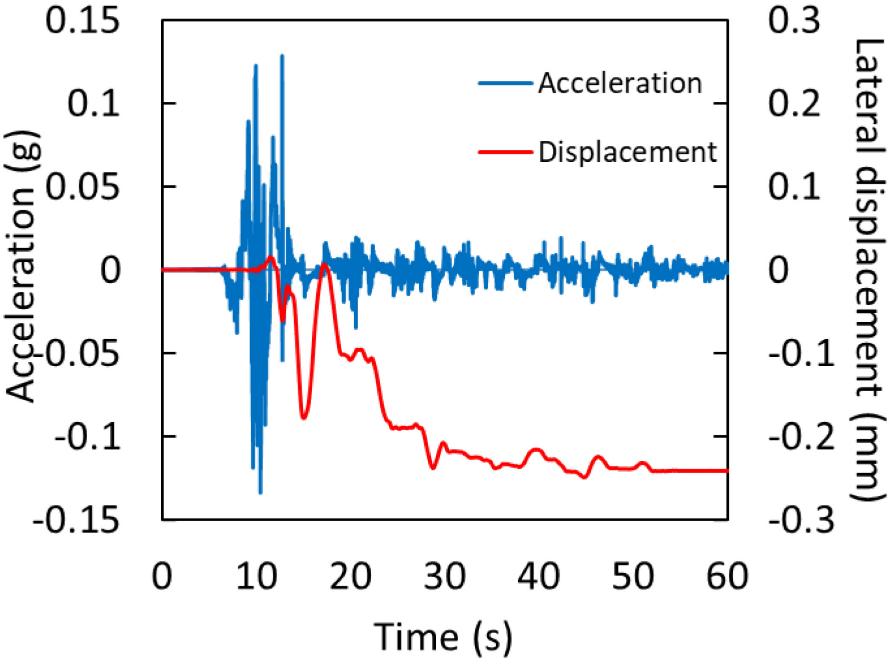

0.15
0.1
0.05
0
-0.05
-0.1
-0.15
Acceleration (g)
0.3
0.2
0.1
0
-0.1
-0.2
-0.3
Lateral displacement (mm)
Acceleration
Displacement
0
10
20
30
40
50
60
Time (s)

(d)

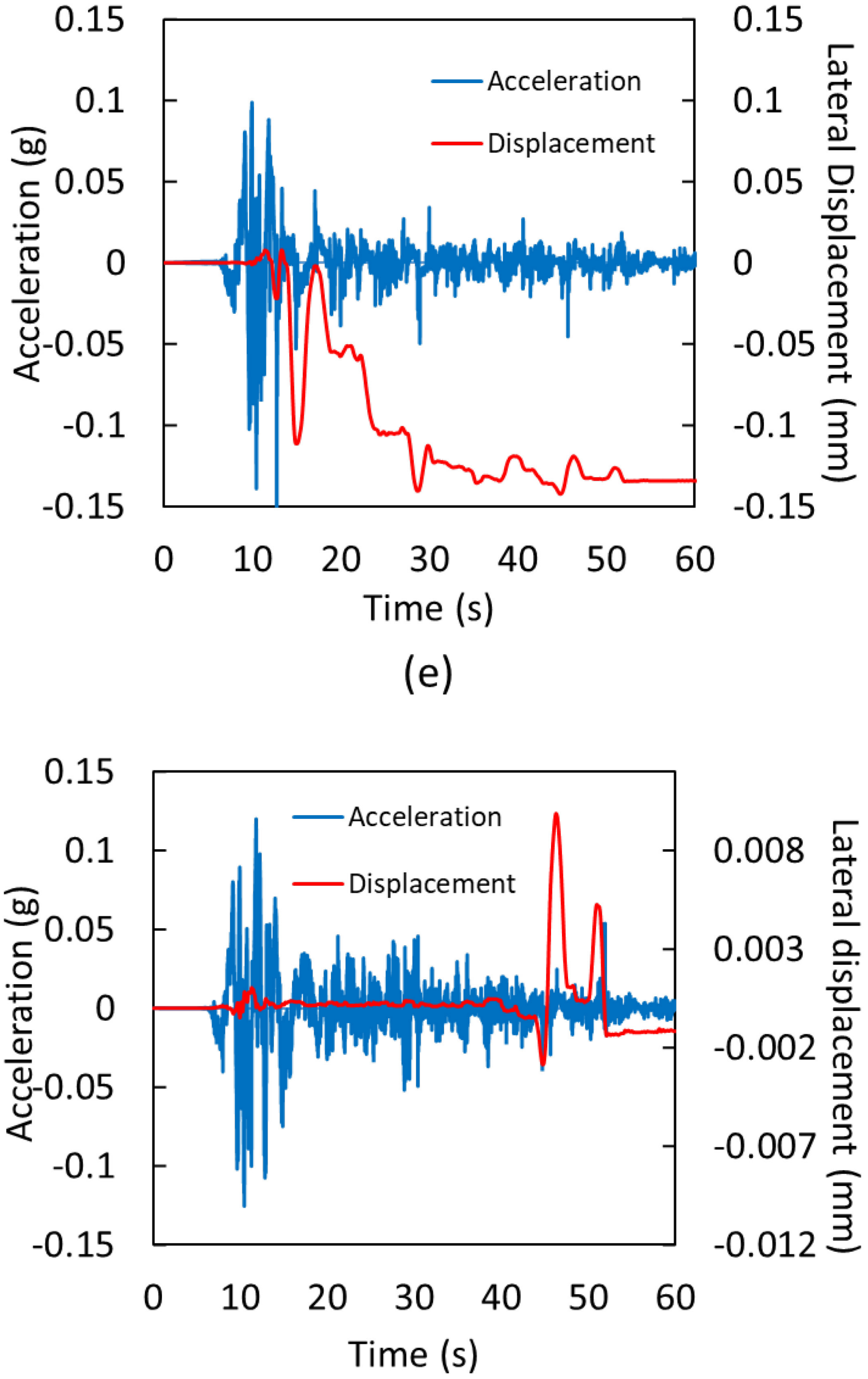

(e)

(f)

Figure 5.13 Soil displacement and acceleration time history: (a) 1.2 m (Gravel), (b) 1.55 m (Clay), (c) 2.1 m (Sand), (d) 3.0 m (Clay), (e) 3.9 m (Sand) and (f) 4.8 m (Silt).

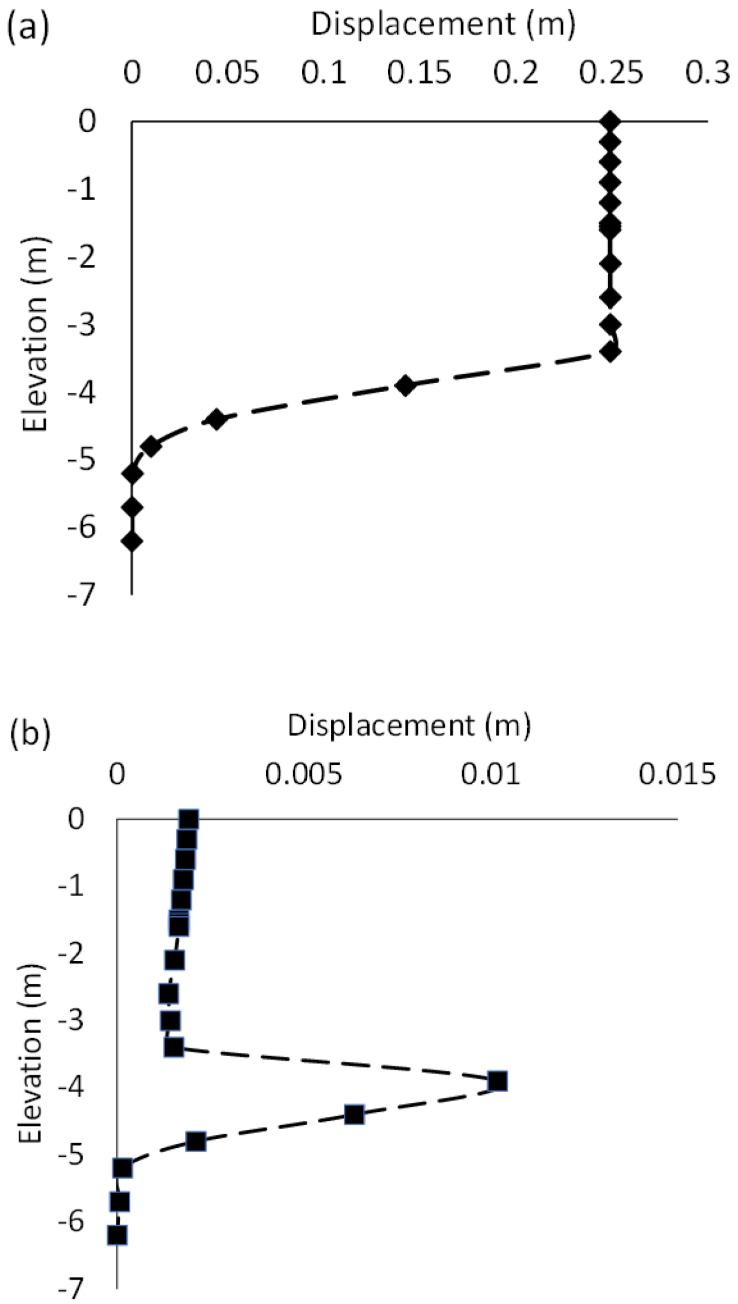

Figure 5.14 Effect of cap layers on soil deformation:(a) longitudinal displacement and (b) vertical displacement

5.5 CONCLUSIONS

1D response analysis was performed to reproduce the 1D experimental model test results, also ID site response analysis was performed for a typical soil profile from Sibalaya site. The influence of cap layers on dynamic soil response is clearly visible. Several contrasting as well as consistent outcomes were observed from both the exercises which are as mentioned below:

- The permeability of the capping layer affects the magnitude of build-up of EPWP and the duration of dissipation.
- Presence of capping layers can cause large, localized shear strain in the soil layers below the cap layer.
- The thickness of the cap layer also significantly affects the soil response as observed from the simulation of soil profile from Trench 4. The thin clay layer near the surface had no influence on cyclic shear stress-strain behaviour or the displacement profile. Furthermore, the sliding seems to have occurred at the silt layer as observed from the longitudinal and vertical displacement and the deformation occurs in dilation without any gain in shear strength which may cause long distance failure.
- The displacement in the soil layers initiates with a delay after the peak ground acceleration and it continues after the strong ground motion has passed.

REFERENCES

Biot, M. A. (1962). The mechanics of deformation and acoustic propagation in porous media. *Journal of Applied Physics*, *33*(4), 1482–1498.

Chan, H. A. C. (1988). *A unified finite element solution to static and dynamic problems in geomechanics*. University Colllege of Swansea, U.K.

El Shamy, U., Zeghal, M., Dobry, R., Thevanayagam, S., Elgamal, A., Abdoun, T., Medina, C., Bethapudi, R., & Bennett, V. (2010). Micromechanical aspects of liquefaction-induced lateral spreading. *International Journal of Geomechanics*, *10*(5), 190–201.

Elgamal, A., Yang, Z., & Lu, J. (2015). *Cyclic 1D Seismic Ground Response Version 1.4 User's Manual.*

Hamada, M. (1992). Large ground deformations and their effects on lifelines : 1964 Niigata earthquake, Case Studies of Liquefaction and Lifeline Performance during Past Earthquakes. *Japanese Case Studies*, *1*, 3.1-3.123. https://ci.nii.ac.jp/naid/10006542527/en/

Hill, R. (1950). *The mathematical theory of plasticity*. Oxford University Press.

Kawakami, F., & Asada, A. (1966). Damage to the ground and earth structures by the niigata earthquake of june 16, 1964. *Soils and Foundations*, *6*(1), 14–30.

Kokusho, T. (2003). Current state of research on flow failure considering void redistribution in liquefied deposits. *Soil Dynamics and Earthquake Engineering*, *23*(7), 585–603.

Kokusho, T., & Kojima, T. (2002). Mechanism for Postliquefaction Water Film Generation in Layered Sand. *Journal of Geotechnical and Geoenvironmental*

Engineering, *128*(2), 129–137.

Kulasingam, R., Malvick, E. J., Boulanger, R. W., & Kutter, B. L. (2004). Strength Loss and Localization at Silt Interlayers in Slopes of Liquefied Sand. *Journal of Geotechnical and Geoenvironmental Engineering*, *130*(11), 1192–1202.

Lu, J., Elgamal, A., Yang, Z., & Diego, S. (2011). *OpenSeesPL : 3D Lateral Pile-Ground Interaction* (Issue December).

Seid-Karbasi, M., & Byrne, P. M. (2007). Seismic liquefaction, lateral spreading, and flow slides: A numerical investigation into void redistribution. *Canadian Geotechnical Journal*, *44*(7), 873–890.

Yang, Z., & Elgamal, A. (2001). Sand Boils and Liquefaction--Induced Lateral Deformation. *15th International Conference on Soil Mechanics and Geotechnical Engineering*, *1989*, 345–350.

Yang, Z., & Elgamal, A. (2002). Influence of Permeability on Liquefaction-Induced Shear deformation. *Journal of Engineering Mechanics*, *128*(7), 720–729.

Zienkiewicz, O. C., Chan, C. H. A., Pastor, M., Paul, D. K., & Shiomi, T. (1990). Static and Dynamic Behaviour of Soils : A Rational Approach to Quantitative Solutions . I . Fully Saturated Problems. *Proceedings of the Royal Society of London. Series A, Mathematical and Physical Sciences*, *429*(1877), 285–309.

CHAPTER 6

CONCLUSIONS AND FUTURE SCOPE

6.1 CONCLUSIONS

The 2018 Sulawesi earthquake triggered extensive flowslides at Balaroa, Petobo, Jono Oge, and Sibalaya in the Palu Valley of Central Sulawesi, Indonesia. To the surprise of many people, the flowslides were triggered on a surface of a very gentle gradient and a few minutes after the cessation of ground motion. Also, due to the absence of any historical geotechnical data of the flowslide sites, it is extremely difficult to conclude the exact cause of flowslides. In the present study, an effort has been made to make clear the mechanism assuming that the flowslides were triggered due to the water film formation under a cap layer.

The primary objective of this research is to identify the key parameters and site conditions that could have led to the triggering of the flowslides. For this purpose, extensive field investigations are performed involving remote sensing with unmanned aerial vehicle (UAV), in-situ portable cone penetration testing (PDCPT), trenching, and collection of disturbed and undisturbed soil samples. The observations from the field are then implemented into 1g shaking table tests and 1D soil model tests, to simulate the site heterogeneities and evaluate the dynamic response of soil profile. The particle image velocimetry (PIV) technique is used to track the soil deformation during earthquake loading. The soil profiles from 1D model tests and trench are then simulated numerically for site response analysis with CYCLIC 1D software and OpenSeesPL software to elucidate the forces generated in the soil profile and the deformation behaviour. Based on the filed investigations, experimental model tests and numerical model studies, following specific conclusions could be derived:

1. The presence of vastly spread liquefiable deposits along with capping layers may significantly increase the potential of flowslide even in the gently sloped ground.
2. Firm bearing gravely sands with low fines content may not liquefy even with the presence of cap layers as observed from the intact cliff walls in Sibalaya.
3. The potential for liquefaction and flowslide is higher for strata with thicker cap layers as thin cap layers tend to break during the ground motion or get punctured by the excessive upward hydraulic pressure of pore water.
4. If the cap layer gets disturbed initially during the shaking, the water film formation may not be observed as seen during 1g shaking table tests. However, the presence of cap layer increases the depth of disturbance of underlying soil layers.
5. Water film formation may not be observed in soil with excessive sand boil formations during liquefaction, as most of the excess pore water pressure gets dissipated through the sand boils.
6. Permeability and plasticity of the cap layers significantly influences the magnitude and duration of dissipation of excess pore water pressure. Plastic cap layers generate a higher magnitude of excess pore water pressure in the underlying soil layers.

6.2 FUTURE SCOPE

This research provides an insight into the influence of multiple capping layers and their influence on excess pore water pressure dissipation. Due to the limitations in experimental and numerical approach the following recommendations are made for future studies:

1. The observations made in this research are based on the hypothesis that the flowslides occurred due to the water film formation, however, the alternate hypothesis of a breach in an underground aquifer triggering the flowslides cannot be neglected. Therefore, future research based on this hypothesis also needs to be performed to understand the mechanism with an alternate viewpoint.
2. The study tries to elaborate factors and parameters which might be behind the triggering of the flowslides, however what caused the flowslides to sustain for such a long distance and time is yet to be made clear. Therefore, in-depth studies elemental tests and numerical studies are required to be performed for detailed analysis of the overall failure scenario.
3. As the flowslides did not occur in the other locations in Palu with similar site conditions like paddy fields and unlined irrigation canal, therefore further investigation of the failed area and surround site is required.
4. For such a large scale flowslide to occur, it is necessary to have a continuity in the capping layers across the failed area. As point investigation methods like PDCPT and soil sampling cannot confirm the presence of such layers in limited time and resources, it is therefore recommended to perform an integrated geophysical and geotechnical survey to confirm the spatial distribution of such layers.

5. To avoid such catastrophic geotechnical failures and loss of lives in future, it is recommended to perform site specific hazard analysis for such areas and generate risk maps for potential hazards.